INFLUENCE OF MICROSTRUCTURE AND ORIENTATION RELATIONSHIPS ON THE MECHANISMS OF PLASTIC DEFORMATION OF A TWO-PHASE Ti - 47.5Al - 2.5Cr ALLOY

Thesis presented at the Institute of Structural Metallurgy
University of Neuchâtel

In fulfillment of the requirements for the degree of Docteur ès Sciences

by

Jeffrey W. Luster
Bachelor of Science, Carnegie Mellon University, USA
Master of Engineering, Catholic University of Leuven, Belgium

Director of Thesis : Professor M.A. Morris

Jury :
Prof. D.G. Morris
Prof. M. Loretto
Prof. J.L. Martin

November 1993

IMPRIMATUR POUR LA THÈSE

Influence of Microstructure and Orientation Relationships on the Mechanisms of Plastic Deformation of a two Phase Ti-47.5 Al - 2.5 Cr Alloy

de Monsieur Jeffrey Luster

UNIVERSITÉ DE NEUCHÂTEL

FACULTÉ DES SCIENCES

La Faculté des sciences de l'Université de Neuchâtel sur le rapport des membres du jury,

Mme et MM. M.A. Morris, J.-L. Martin (EPF-Lausanne), D.G. Morris et M. Loretto (Birmingham)

autorise l'impression de la présente thèse.

Neuchâtel, le 30 juin 1994

Le doyen:

H.-H. Nägeli

Abstract

Alloys based on the intermetallic phase TiAl are of interest due to their low density and attractive mechanical properties, however, industrial application is currently limited by the poor ambient temperature ductility of the alloys. The goal of this work is to clarify the influence of microstructure and orientation relationships on the mechanisms of room temperature deformation of two-phase TiAl / Ti_3Al alloys. Although the basic relationships between microstructure and mechanical properties are being established in these two-phase alloys, little is known about the underlying deformation mechanisms. Moreover, the influence of the orientation relationships which exist in these two-phase alloys on the deformation behavior also need to be defined.

Therefore, a cast **two-phase Ti-47.5Al-2.5Cr alloy** was heat treated to produce two microstructural conditions for detailed study of the deformation mechanisms using transmission electron microscopy (TEM). The two microstructures studied were a **transformed lamellar** structure with a bimodal lamellar distribution and an **equiaxed** microstructure which consisted of elongated Ti_3Al particles dispersed in a matrix of equiaxed TiAl grains. Samples of the heat-treated materials were then deformed 2% in compression at room temperature and the resulting deformation mechanisms were identified. Consistent indexing methods were established and used to determine the unique orientation relationships between grains which subsequently allowed for the spatially correct determination of the deformation mechanisms. In order to identify the influence of these orientation relationships on the deformation process, a **geometric compatibility factor** has been introduced which can be used to measure the relative alignment of the slip systems in adjacent grains. This relative alignment is significant since it is expected to control the transfer of deformation across the *grain or lamellar boundaries.*

Analysis of the deformation mechanisms and orientation relationships in many grains has been used to show that the active deformation mechanisms are determined by both the Schmid and geometric compatibility factors. It is also shown that deformation twinning of the type 1/6<112]{111} and glide of ordinary 1/2<110] dislocations on the close-packed {111} planes are the preferred deformation modes. <101] and 1/2<112] superdislocations are usually only present in grains where twinning and ordinary dislocations are not easily activated. This asymmetric deformation behavior is understood by consideration of the ordered $L1_0$ structure and the polarity of the twinning process. Furthermore, it has been shown both experimentally and theoretically that the 120° type orientation rotation provides the best geometric compatibility of slip systems in adjacent grains. The geometric compatibility factor has been shown to be useful in predicting the activation of slip systems in response to a stress concentration and activation of the required slip systems in the fine lamellar structures. Finally, the deformation behavior of the Ti_3Al phase is shown to have a notable impact on the deformation characteristics of the lamellar structure.

These findings indicate that the transmission of deformation across grains is, as expected, controlled by the orientation relationship between the grains. Since different relationships provide differing compatibilites od slip systems in the adjacent grains, it is expected that the ductility of two-phase alloys can be modified through careful control of the microstructure to obtain the maximum number of favorable 120° rotations. In this light, it is expected that the equiaxed microstructure possesses a superior ductility due to the relative ease of activation of deformation twinning, increased localized deformation and a favorable distribution of orientation relationships. In grains where the favorable ordinary dislocations and twinning are not easily activated, superdislocations are necessary. Understanding the behavior of these dislocations with the aim of increasing their mobility still remains an important route for improving the ductility of these TiAl alloys.

Table of Contents

1. Introduction and Literature Review

1.1. General Introduction

The useful potential of many current high temperature structural alloys has been, to a great extent, already exploited. This is especially true, for example, for nickel and titanium base alloys [1-4]. Therefore, alternative materials or materials systems are being sought for the next generation of aerospace vehicles and engines, to improve the efficiency of industrial equipment and to reduce the burden on the environment. One possibility for the attainment of materials which present a revolutionary improvement in properties is the family of materials designated *intermetallic phases*. In general terms, an intermetallic compound may be defined as a phase which crystallizes in a structure different from that of its components, where this structure is ordered such that the individual atomic species assume well defined positions within the crystal lattice and whose composition is usually near a simple stoichiometric ratio.

Although intermetallic phases were identified nearly 100 years ago [5], it has been only recently that attempts have been made to isolate them for use as monolithic materials [6]. Intermetallic alloys based on the aluminides are the most widely researched and developed materials. These materials are highly desirable due to their low density and inherent corrosion and oxidation resistance. While their development is largely driven by the aerospace industry [7-9], demand for improved materials for fossil fuel plants [10], industrial turbines [4] and automotive applications [11-13] also exists. The long range order present in intermetallic phases can have dramatic effects on the mechanical properties due to the combination of metallic and covalent types of bonding [5,14]. These effects generally include increased strength and temperature resistance which are, unfortunately, almost always accompanied by decreases in ductility. It is this brittle behavior of virtually all intermetallics that has, so far, limited their widespread application.

A comparison of the state-of-the-art in 1966 [6] with recent review articles [15,16] shows just how much progress has been made towards the development and understanding of intermetallics. One of the most frequently investigated alloy systems is the Ti-Al system where three intermetallic compounds can be identified. For titanium-rich compositions near the stoichiometric ratio 3:1 Ti/Al exists the compound Ti_3Al, one of the first compounds to be extensively developed and which is, to a large extent, responsible for the current interest in intermetallics [2]. At nearly equiatomic Ti-Al compositions exists the TiAl ordered phase. Alloys based upon this phase are currently the most active area of research in intermetallics [7,11] and will be the focus of this thesis. Finally, for aluminum-rich compositions, the stoichiometric line compound Al_3Ti can be identified.

1.2 The Intermetallic Phase TiAl

The intermetallic phase TiAl, commonly referred to as the gamma phase or γ-TiAl, forms for nearly equiatomic compositions of Ti and Al. A range of compositions from 48-55 atomic % aluminum are stable depending upon temperature and alloy purity. TiAl possesses the $L1_0$ ordered structure which is composed of alternate (002) layers of titanium and aluminum atoms [17]. Although the structure is, strictly speaking, face-centered tetragonal (fct), the low c/a axial ratio (≈1.02) indicates that the structure can be roughly treated as cubic for most purposes. The phase is fully ordered up to the melting temperature of approximately 1450°C and, combined with the low density (≈3.8 gcm^{-3}), give the alloy desirable specific and elevated temperature properties. However, the first survey of TiAl alloys in 1956 indicated that, although the alloy exhibited interesting strength, hardness and thermal stability, it was extremely brittle at room temperature [18]. Unfortunately, even after substantial research and development efforts, single-phase TiAl alloys remain very brittle and are no longer considered potentially useful materials. However, two-phase alloys based on TiAl and Ti_3Al do show good potential for industrial utilization and these will be discussed in detail in Section 1.4.

1.2.1 Crystallography

The $L1_0$ unit cell is shown in Figure 1.1. The alternate (002) planes of aluminum and titanium are readily seen in this diagram. Since the c/a ratio is almost unity, the unit cell can, for most purposes, be considered cubic. However, while the dimensions of the cell are nearly cubic, the $L1_0$ ordering indicates that not all directions within the same family are equivalent. For instance, [110] is not equivalent to [101] or [011], [100] is not equivalent to [001] or [010], and so on. *In order to simplify the designation of families of equivalent* directions, a mixed notation has been introduced [19] such that equivalent directions are represented by <hkl]. This notation indicates that the h and k indices may be permutated, while the l index remains fixed. Also indicated in Figure 1.1 are some of the important directions which could be possible perfect dislocation Burgers vectors. In increasing order of length, these lattice translation vectors are 1/2<110], <100>, 1/2<112] and <101].[1] It should be noted that a translation of 1/2<110] would shear the atoms to a chemically correct lattice position. This translation is the same as that of the normal dislocation in a fcc crystal and is, thus, referred to as an *ordinary dislocation*. In contrast, a translation of 1/2<101] would move the atoms to a chemically incorrect lattice site such that a perfect lattice translation requires a displacement twice this

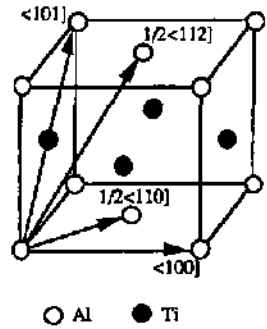

Figure 1.1 : The $L1_0$ unit cell.

[1] Throughout this text, the lattice parameter, a, will be left out of the notation of the Burgers vector. However, its presence is always implicit. Furthermore, to be strictly correct, a 1/2<112] dislocation would be properly indicated by use of both the a and c lattice parameters as 1/2<a, a, 2c].

length or <101]. This type of translation is commonly referred to as a *superdislocation* since it is composed of two individual 1/2<101] dislocations which glide in pairs separated by a region of incorrect atomic stacking called an *antiphase boundary*, APB. A second possible type of superdislocation is the 1/2<112] translation. Finally, a translation of <100> could also be a perfect dislocation. It should be noted that both the 1/2<110] ordinary dislocation and <101] superdislocation could be expected to be glissile in two close-packed {111] planes, while a 1/2<112] superdislocation would only be glissile in one.

Since the glide planes are of the {111} type, it is useful to look at the stacking arrangement of the (111) plane in order to gain more understanding of the possible dislocations and planar stacking faults in the $L1_0$ structure. A representation of three close-packed planes projected along the [111] direction is shown in Figure 1.2. With the aid of this diagram, it is useful to define the three types planar stacking faults which are possible in the $L1_0$ structure [20]:

1.) Superlattice Stacking Faults (SSF) - the atomic stacking sequence is modified. A translation of the type 1/6<112] creates this type of fault.

2.) Antiphase Boundaries (APB) - correct atomic stacking is maintained, but chemically incorrect first neighbor atoms are introduced. This is created by a translation of 1/2<101], for example.

3.) Complex Stacking Faults (CSF) - both the stacking sequence and chemistry of the neighbor atoms are modified (a combination of both a SSF and an APB). Translations of the type 1/6<211] will create this arrangement.

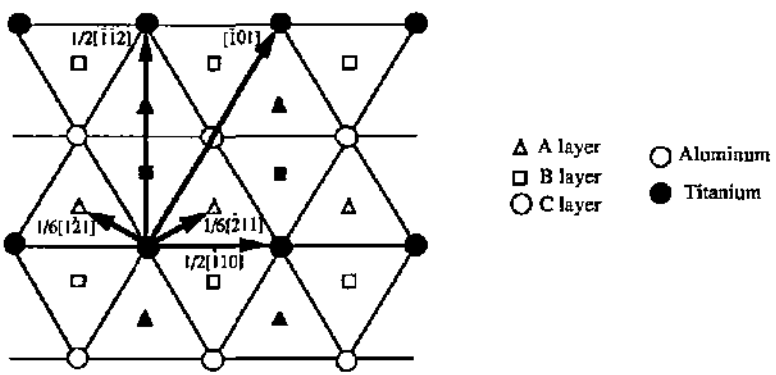

Figure 1.2 : Three layers of close-packed (111) planes projected along the [111] direction.

The diagram in Fig 1.2 clearly shows that a translation of 1/2<110] leaves the lattice undisturbed and is, therefore, a perfect dislocation. As stated above, glide of a 1/2<101] dislocation will create an APB and is, therefore, only a partial dislocation. In order to return the stacking sequence back to the undisturbed state, a second 1/2<101] partial dislocation must trail the first dislocation to correct the

stacking sequence and, thus, form a <101] superdislocation. It is also evident from this diagram that a translation of 1/2<112] will also be a perfect dislocation. This dislocation is also termed a superdislocation since, in theory, this dislocation may also dissociate into three parallel partial dislocations of 1/6<112]. These Shockley partial dislocations alter the stacking sequence, but not the type of nearest neighbor atom and are, hence, analogous to the Shockley partial dislocations in the fcc structure. In contrast, the 1/6<211] Shockley partials will change both the stacking and ordering and are, therefore, not analogous to the partials in the fcc crystal. Finally, it could be expected that twinning could occur in this alloy by passage of Shockley partial dislocations on successive {111} planes. However, it is very important to note that only 1/6<112] Shockley partials may be twinning partial dislocations since these do not modify the ordering sequence during the twinning operation [21]. In contrast, passage of 1/6<211] partial dislocations on successive {111} planes would result in the creation of a pseudo-twin arrangement - i.e. the lattice sites are sheared into the correct lattice orientation for a twin, but the lattice sites are occupied by the incorrect atomic species.

1.2.2 Room Temperature Deformation Mechanisms

Now that the crystallography of the $L1_0$ structure has been clearly defined, it is possible to discuss the dislocations which have been observed in TiAl alloys. The first detailed study of the deformation of TiAl identified 1/2<110] ordinary dislocations, <101] superdislocations and 1/6<112]{111} deformation twinning [22]. Elongated stacking faults on the {111} bound by 1/6<112] partial dislocations were also observed. In a subsequent deformation study, 1/2<112] superdislocations were also identified [20]. Finally, perfect dislocations of the Burgers vector <100> have also been observed, although only at very high temperatures [23,24]. The appearance of these dislocations at elevated temperatures is similar to the related fcc structure and these dislocations will not be considered further since they have not been identified at room temperature. To recapitulate, the following deformation structures have been identified in TiAl:

a.) 1/2<110] ordinary dislocations,
b.) <101] superdislocations,
c.) 1/2<112] superdislocations,
d.) deformation twinning, only of the 1/6<112]{111} type and,
e.) stacking faults on {111} planes which are bound by 1/6<112] partial dislocations.

A summary of the major deformation studies which have been undertaken on single-phase TiAl alloys is given in Table 1.1 in order to establish the relative importance of these different mechanisms. Firstly, it should be noted there is strong agreement between most studies that the dominant deformation mechanisms are 1/2<110] ordinary dislocations and <101] superdislocations with some deformation twinning. Stacking faults as described above are also usually identified. Furthermore, most of the studies indicate that the 1/2<112] dislocations are much less frequent and it is suggested that these dislocations are usually a reaction product [33,37]. Notwithstanding this general agreement

Investigator	Alloy	1/2<110] Ordinary	1/6<112] Twinning	<011] Superdisl.	1/2<112] Superdisl.	Stacking Faults
Shechtmann [23]	Ti-54Al	numerous	at small strains	large number	n.a.	numerous
Lipsitt [25]	Ti-54Al	major mode	observed	fewer	n.a.	observed
Kawabata [26]	Ti-54Al SC	observed	n.a.	observed	n.a.	n.a.
Hug [19,20]	Ti-54Al	observed	observed	observed	fewer	frequent
Hug [27]	Ti-54Al-Mn	dominate	observed	fewer	observed	few
Hall [28]	Ti-52Al	observed	many	observed	observed	observed
Court [29]	Ti-52Al	negligible	observed	observed	none	many
Vasudevan [30] *	Ti-50Al-0.4Er	dominant	observed	n.a.	n.a.	few
Whang [31]	Ti-54Al-2V	many	n.a.	many	rare	dominant
Huang [32]	Ti-52Al	observed	rare	observed	observed	abundant
Farenc [33]	Ti-54Al	observed	observed	observed	reaction only	n.a.
Sriram [34] *	Ti-52Al Ti-50Al	high density	observed	fewer	moderate	n.a.
Greenberg [35]	Ti-54Al	observed	n.a.	observed	fewer	observed
Chaudhuri [36]	Ti-52Al-3V	few	observed	dominant	none	many

Table 1.1 : Summary of the room temperature deformation mechanisms of single-phase TiAl alloys as reported by various investigators. n.a. indicates that this deformation mechanism was not analyzed or reported, * indicates studies on low oxygen materials and SC designates single crystal studies.

between the studies, discrepancies exist on the relative importance of the 1/2<110] and <101] dislocations. For instance, many authors [20,22,25,31] indicate that 1/2<110] dislocations are the dominant deformation mode in these alloys, while, in contrast, several others [29,32,36] have concluded that the <101] superdislocations are the dominant deformation mode. In this light, it is interesting to note that several studies have been performed on alloys with very low oxygen contents in order to determine the influence of this interstitial element on the deformation mechanisms [30,34]. In both of the studies, the 1/2<110] dislocations were reported to be much more important than the <101] superdislocations. Therefore, differences in the activity of 1/2<110] and <101] dislocations in the various studies could be due to varying oxygen contents in the different alloys. Statistical examinations of alloys with varying oxygen content are currently in progress [30].

As previously stated, stacking fault arrangements on the {111} planes and bound by 1/6<112] type Shockley partial dislocations are frequently observed in these alloys [22]. Subsequent work further defined the characteristics of these stacking faults as follows [20]:

1.) They are extrinsically faulted dipoles and the extrinsic nature indicates that they must be formed by the passage of two partial dislocations on successive {111} planes.

2.) They are always associated with 1/2<112] superdislocations which are discontinuously dissociated along their length.

3.) They are always elongated in a <101] direction.

Based on these observations, the following reaction was proposed to account for the formation of these *faulted dipoles* (as they will subsequently be referred to):

$$1/2\langle 112] \Rightarrow 1/6\langle 112] + \text{SESF} + 1/3\langle 112] \qquad 1.1)$$

where SESF represents an extrinsic stacking fault. A formation mechanism for these faults was proposed based upon the local pinning of a 1/2<112] dislocation into a dipole and the subsequent rearrangement of the core of this dislocation to the faulted arrangement [20]. Subsequent studies have called the finding of extrinsic faults into question and this sheds some doubt on the validity of the proposod formation mechanism [38]. Alternative formation mechanisms have recently been proposed [37]. Given the widespread observation of these faulted dipoles, it is curious that relatively little study has been devoted to these faults; however, these are the subject of ongoing research [39].

Many complex dissociations and core arrangements have been predicted for the $L1_0$ structure [40-42]. The distances between the dissociated partial dislocations have been calculated using elasticity theory [43] and the energies of various non-planar core configurations [42] have also been computed. While the importance of the detailed core structure on the mobility of dislocations is well established [44],

this is not the object of this work and, thus, will not be discussed here.[2] In general, the dislocations may split into, for example, superpartial or Shockley partial dislocations separated by any of the three types of stacking faults indicated previously. Furthermore, several decompositions (distinct from dissociations in that the resultant dislocations are perfect dislocations rather than partial dislocations) have been shown to be important in TiAl.

1.3 The Intermetallic Phase Ti_3Al

For compositions near Ti-25Al, the stoichiometric compound Ti_3Al forms with the DO_{19} ordered hexagonal phase. This phase, commonly designated α_2, is stable for compositions ranging from approximately 22 to 35% aluminum and undergoes an order-disorder transition at a maximum of 1200°C. The DO_{19} structure is shown below in Figure 1.3. As can be seen in the diagram, the a lattice parameter is twice that of the disordered hexagonal phase, α, while the c parameter remains the same. However, the standard hexagonal system is still used to designate the planes and directions in this ordered structure, for instance, the [0001] and $[2\bar{1}\bar{1}0]$ have been indicated in the diagram. It is necessary to recall that directions and planes will, in general, not be perpendicular in the hexagonal system. Three different types of dislocations can be observed in Ti_3Al alloys - namely, <a>, [c] and <a/2 + c> dislocations [45]. The $1/6\langle\bar{1}\bar{1}20\rangle$ dislocations, or dislocations <a> type usually travel in superdislocation pairs [46] and are the most commonly observed dislocations [47-49]. These dislocations are usually glissile on the $\{\bar{1}100\}$ prism planes, although they have also rarely been observed on the (0001) basal plane [50]. The <a/2 + c>, or $\langle 11\bar{2}6\rangle$, type dislocations which are glissile on the $\{11\bar{2}\bar{1}\}$ pyramidal planes are only rarely observed and exhibit a very high critical resolved shear stress [48,51]. It has been shown that alloying additions, for example, Nb, can render the activation of these pyramidal dislocations [47] more favorable. Pure [c] dislocations, or [0001], have also been observed [47,52], although only rarely and they are believed to be largely immobile. Finally, under the neces-

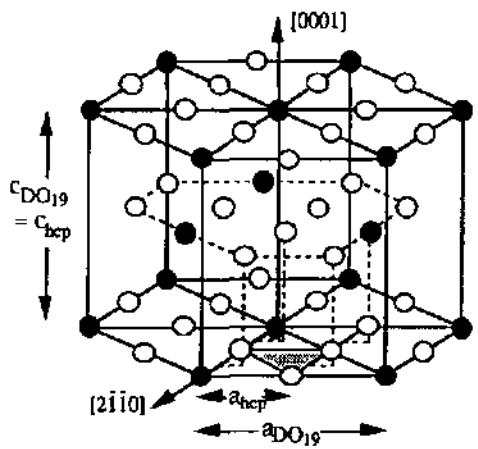

Figure 1.3 : DO_{19} structure of Ti_3Al.
● Al and ○ Ti atoms.

[2] For further details concerning the possible dislocation dissociations and decompositions, the reader is referred to, for example, [19, 41-43].

sary loading conditions, deformation twinning has also been observed [53]. As with conventional titanium alloys, interstitial elements such as oxygen are expected to have a large influence on the deformation mechanisms and ductility of Ti_3Al alloys.

1.4 Two-Phase TiAl / Ti_3Al Alloys

Although single-phase alloys show little technological promise due to their brittle behavior, two-phase alloys consisting of the TiAl and Ti_3Al phases are currently of great interest because of their improved ductility and interesting combinations of mechanical properties. For full details of two-phase alloys, the reader is referred to a number of excellent reviews [15,54]. For compositions between 35 to 50% aluminum, two-phase alloys are possible which consist of the two phases individually described above. Typically, alloys under development contain between 47 to 49 % aluminum with further alloying additions added to optimize the combination of mechanical properties. In order to understand the microstructural development of these alloys, an expanded view of the central portion of the Ti-Al phase diagram is shown in Figure 1.4. For these alloys, a single-phase disordered α phase region exists between 1350°C and 1450°C. Upon cooling from this phase region, the ordered γ phase will begin to precipitate from the disordered α phase. Depending upon the exact composition, two reactions are possible upon further cooling. For aluminum-rich compositions, at some temperature within the two phase $\gamma + \alpha$ phase region, the disordered α phase may undergo an ordering transformation to form the ordered α_2 phase [54]. For leaner compositions, any remaining α phase will decompose into the α_2 and γ phases at the eutectoid temperature of 1120°C.

1.4.1 Orientation Relationships

When the γ phase precipitates either from the disordered α phase or the ordered α_2 phase, the two phases will exhibit the following crystallographic orientation relationship [55]:

$$[\bar{2}110]_{\alpha_2} // \langle 011 \rangle_{\gamma} \text{ and } (0001)_{\alpha_2} // \{111\}_{\gamma} \qquad 1.2)$$

Yamaguchi has subsequently shown that this relationship is more properly written as [56]

$$\langle \bar{2}110 \rangle_{\alpha_2} // [110]_{\gamma} \text{ and } (0001)_{\alpha_2} // \{111\}_{\gamma} \qquad 1.3)$$

since only the <110] direction is exactly parallel to a $\langle \bar{2}110 \rangle$ direction in the α_2, while the <101] directions are usually 0.2-0.3° from being exactly parallel due to the tetragonality of the $L1_0$ structure. According to this orientation relationship, the basal plane of the α_2 and a {111} octahedral plane in the γ phase will be parallel and, therefore, define the interfacial boundary plane between the two phases. Due to this orientation relationship, the two-phase microstructure will tend to be composed of aligned lamellae of the two phases.

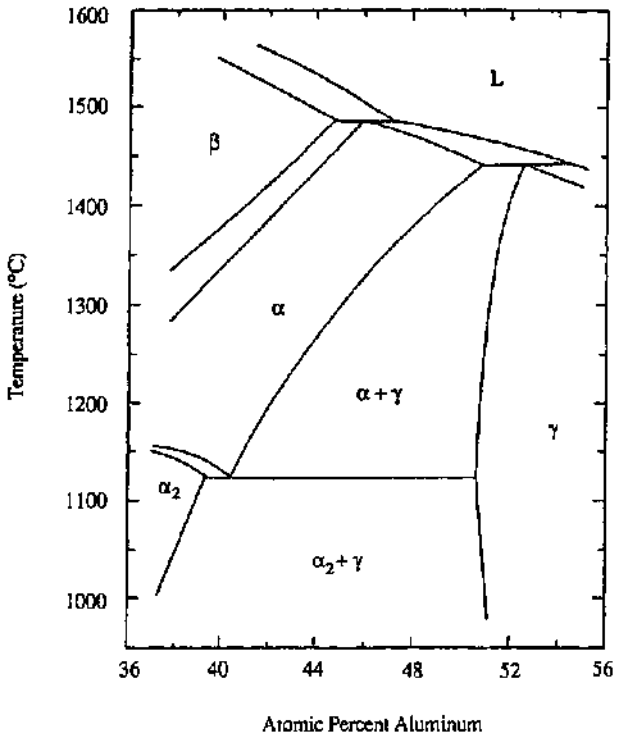

Figure 1.4 : The central portion of the binary aluminum - titanium phase diagram from [57].

In these lamellar structures, it is also possible for adjacent γ phase lamellae which may come into contact to exhibit defined orientation relationships. Feng et. al. [58] was the first to observe that adjacent lamellae could exhibit both a twin relationship, defined using the notation of a deformation twin as <11$\bar{2}$](111), and a pseudo-twin relationship defined by <121](111). The existence of these supposedly forbidden pseudo-twin adjacent lamellae was rationalized by the presence of a thin layer of Ti_3Al between the adjacent γ lamellae. It was later shown that there must not necessarily be a thin α_2 layer and that adjacent γ lamellae of all orientations may come into contact [59]. Subsequently, Schwartz and Sastry showed that, in addition to these twin and pseudo-twin relationships, a "stacking fault"-like relationship could also be observed in which all planes within the two lamellae are parallel [60]. It was later shown that this relationship could be described as a 90° rotation about a <010> cube axis [61]. Differently oriented regions within a single lamellae have also been observed [61,62] and these are always described by the 90° type rotation about a cube axis.

On the basis of these observations, several authors [62-64] proposed that a total of six orientational variants of the γ lamellae could be formed and that four of these could be individually distinguished. These relationships have most clearly been described by Yamaguchi [15,64-65] and his notation will be used throughout this text. Simply, the orientation relationship between the γ and α_2 shown in equation 1.10 is obeyed such that the $\langle 110 \rangle_\gamma$ may be parallel to any one of the three <1120> directions in the α_2. Referring to the schematic diagrams of the atomic stacking and important directions in both the $(0001)_{\alpha_2}$ and $(111)_\gamma$ shown in Figure 1.5, it is evident that the $[\bar{1}10]$ direction in γ (designated A) may be parallel to any of the three $\langle 11\bar{2}0 \rangle$ directions in α_2 (designated a, b and c). If the anti-parallel directions are included, the $[\bar{1}10]_\gamma$ may be aligned in a total of six different orientations with respect to the α_2.

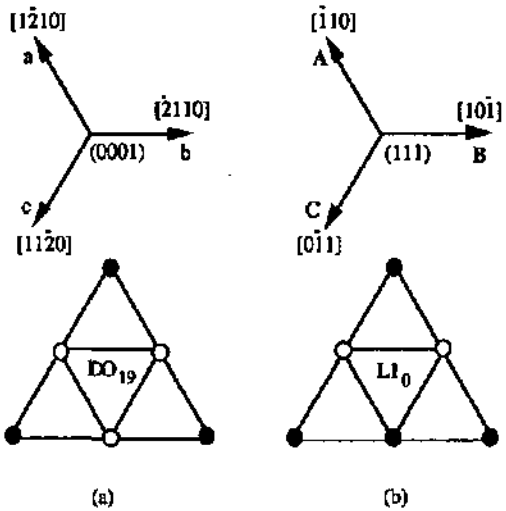

Figure 1.5 : Schematic diagram of the planar stacking and important directions a.) of the (0001) basal plane of Ti_3Al and b.) the (111) plane of TiAl. For the direction A parallel or anti-parallel to the directions a, b and c in Ti_3Al, the orientation relationship given in equation 1.10 is fulfilled. Atomic positions of these two planes match across the interphase interface with only a slight misfit, however an abrupt change in chemical composition exists.

Referring to Fig 1.5, these six orientational variants can be described as :

$$A \Uparrow a \qquad A \Uparrow b \qquad A \Uparrow c \qquad 1.4a)$$

$$A \Downarrow a \qquad A \Downarrow b \qquad A \Downarrow c \qquad 1.4b)$$

where ⇑ and ⇓ indicate parallel and anti-parallel operations, respectively. As a *consequence* of these orientational variants, adjacent TiAl lamellae will also exhibit a defined orientation relationship. These are most conveniently defined as a rotation of multiples of 60° about the normal to the (111) plane as follows:

$$180° \; A \Downarrow A \qquad 60° \; A \Uparrow B \qquad 300° \; A \Downarrow C \qquad 1.5a)$$

$$0° \; A \Uparrow A \qquad 240° \; A \Downarrow B \qquad 120° \; A \Uparrow C \qquad 1.5b)$$

These γ/γ orientation relationships can now be described as follows. For the rotations listed in equation 1.5a), the ABCABC stacking sequence changes to CBACBA in the adjacent grain. Therefore, the $A \Downarrow A$ 180° rotation describes a true twin relationship, while the 60° or 300° rotation describes a pseudo-twin relationship. In contrast, for the rotations given in equation 1.5b), the ABCABC stacking sequence is maintained in both grains. The 0° rotation results in translational order fault and has only recently been observed [66]. The 120° or 240° rotation is commonly observed and results in a 120° rotational fault with the c-axes orthogonal in the two grains. Therefore, these 120° type rotations are also equally described by a rotation of 90° about a <010> cube axis. On the basis of these works, it has been proposed that six orientation relationships exist between adjacent γ regions. However, only *four* of these have been experimentally verified. The observation of only four is due to the fact that the 60° and 300° or the 120° and 240° rotations are crystallographically equivalent operations. The four types of γ/γ orientation relationships which exist are :

I.) the true twin, 180° relationship
II.) the pseudo-twin relationship described by either a 60° or 300° rotation
III.) the rotational fault with orthogonal c-axes described by 120° or 240°
IV.) the translational order fault, 0°.

All of the above types of rotations have been observed for adjacent lamellae. However, several authors have noted that the 180° true twin relationship is the most common between adjacent γ lamellae and this is understood by energetic considerations of the possible boundary types [64]. For differently oriented regions within the same lamellae, only the 120° type rotation has been observed [61-62]. Finally, it should be mentioned that various types of dislocations have been observed in the various types of interfaces [67-75] and it has been suggested that alloying additions can be used to alter this interfacial structure in order to, ultimately, improve the ductility [76-77].

1.4.2 Microstructures

As mentioned above, the crystallographic relationship between the α_2 and γ phases indicates that a lamellar structure will commonly form for two-phase alloys. Cast alloys will generally consist of a lamellar microstructure. As expected, however, appropriate thermomechanical treatments can be used to modify this lamellar structure in order to create a variety of microstructural distributions. In part, these thermomechanical treatments can be compared to those of, for instance, steel such that the microstructure resulting from a specific treatment can be predicted. In contrast with steels, the eutectoid lamellar structure is not a classical eutectoid reaction - i.e. where the lamellar structure is formed through the cooperative growth of both phases. Rather, the lamellar structure is created by the precipitation and growth of individual γ phase plates from the α or α_2 phases [78]. Furthermore, it

should be noted that the phase transformations in these alloys are generally very sluggish [79-80] such that long-time aging treatments may be required to achieve the necessary structural modifications and, in some instances, the required changes may be induced only by sufficiently hot-working the cast structure.

An efficient and simple microstructural classification system has been devised by Kim [81-82]. Rigorous microstructural investigations were performed in order to define four types of common microstructures : near gamma, duplex, near lamellar and fully lamellar. Depending upon the alloy composition, aging treatments performed just above the eutectoid temperature (>1120°C) result in a microstructure which is composed largely of γ grains. Fine α_2 grains or discrete particles may be dispersed throughout this *near gamma* structure. For higher heat treatment temperatures in the $\alpha + \gamma$ phase field, a *duplex* microstructure consisting of γ and lamellar α_2 / γ grains. This structure is formed when the heat treatment temperature is chosen so that nearly equal portions of α and γ phases exist at elevated temperature. During cooling, the γ-phase grains are retained, while the α-phase grains decompose into the lamellar structure consisting of alternating plates of α_2 and γ. This structure is generally the finest with grain sizes ranging from 20-50 µm. Aging just below the alpha-transus temperature in the $\alpha + \gamma$ field, *near lamellar* microstructures will be formed which consist of large lamellar grains with few primary γ grains dispersed at the grain boundaries. Finally, for the highest heat treatment temperatures, i.e. - in the α phase region, *fully lamellar* structures similar to those of the as-cast structure will be formed. Grain growth is rapid in this phase field and fully lamellar structures are generally very coarse. An alternative to the duplex structure could also be envisioned with a dual phase structure consisting of equiaxed α_2 and γ grains [57]. These different types of microstructures are schematically represented in Figure 1.6. It should be noted that the formation of each of these structures will clearly depend on alloy composition. Moreover, the addition of third elements may alter these microstructures by changing the reaction kinetics [83-84].

Obviously, many microstructural parameters will be important in describing the final microstructures resulting for any given heat treatment [15] such as:

- the grain size,
- the fraction and distribution of the various types of grains,
- the chemical composition of the phases,
- thickness of the individual α_2 and γ lamellae,
- the volume fraction of α_2 lamellae,
- the size of the oriented domains within the γ lamellae,
- the distribution of orientation relationships between adjacent γ lamellae.

It has been shown that the lamellar thickness can be varied through appropriate control of the cooling rates [85-86] while, in addition to well defined lamellar structures, quenching treatments have been used to produce Widmanstatten and acicular, massively transformed α_2 / γ structures [78,87-89].

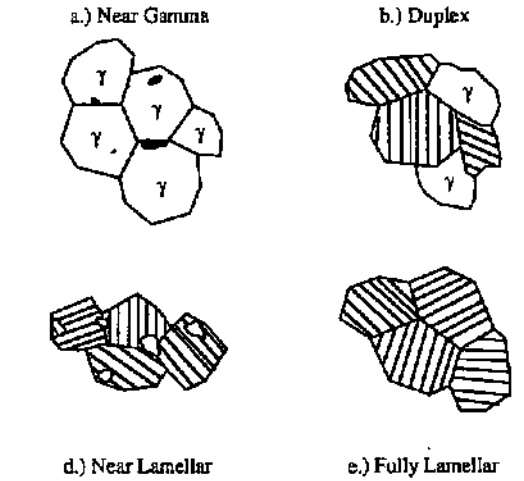

Figure 1.6 : Various microstructures of two-phase alloys that can be created through appropriate thermomechanical treatment as described in the text.

1.4.3 Mechanical Properties

The most remarkable difference between the mechanical properties of two-phase alloys versus single-phase alloys is the dramatic increase in tensile ductility [1,28,90-92]. While single-phase alloys generally fracture prior to appreciable plastic deformation, two-phase alloys have been developed which exhibit up to 3.5% tensile elongation prior to failure [1]. The maximum tensile ductility is generally achieved for compositions with 47-48 % aluminum [90-91]. Further alloying additions of 2-3% Cr [57,93-94], V [95] and Mn [96] have also been shown to improve the ductility of two-phase alloys. However, these alloying additions have not been shown to improve the ductility of the single-phase alloys. Several explanations have been proposed to account for the mechanism of the improved ductility of the two-phase alloys including reduced tetragonality of the lattice, altered atomic bonding characteristics, gettering of interstitial elements by the α_2 phase, reduced grain sizes and increased dislocation sources [32].

Furthermore, the specific microstructural distribution will greatly influence the mechanical properties of the alloys and defining these structure / property relationships has been the focus of a number of studies [57,79,81,97-99]. Shown in Figure 1.7 is a schematic description of the general influence of microstructure on the mechanical properties of binary alloys. In general, duplex alloys exhibit the best ductility, but rather poor strength [57,82]. In contrast, lamellar alloys exhibit greater strength but with a corresponding decrease in ductility. The lamellar alloys also exhibit rather high values of fracture toughness (up to 35 MPa$\sqrt{m}$ [100]) in comparison to the duplex structures (approximately 10-12 MPa$\sqrt{m}$). Therefore, there exists a definite tradeoff in the ductility versus fracture toughness in TiAl alloys [54,81,98-99] which runs contrary to the common expectations for metallic materials.

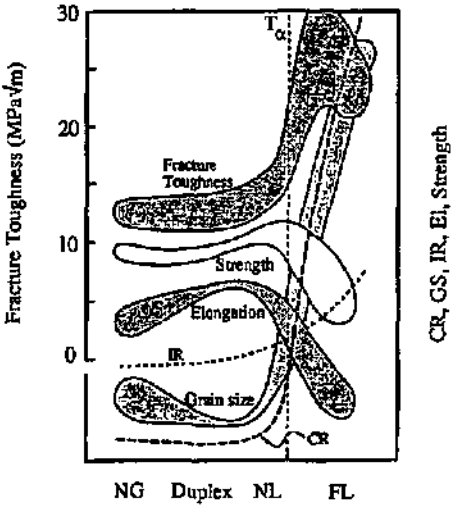

Figure 1.7 : Schematic relationships between the microstructure and mechanical properties. (NG) is near gamma, (NL) near lamellar and (FL) fully lamellar and (GS) is the grain size. Mechanical properties include fracture toughness, tensile strength and elongation (EL), impact resistance (IR) and creep resistance (CR). After [54].

The large variety of heat treatment schemes which results in a seemingly endless variety of microstructures gives a correspondingly wide range of mechanical properties. For example, a Ti-48Al alloy can be heat-treated to yield strengths ranging from 260 MPa to 400 MPa, while the tensile ductility ranges from 0.4 to 2.0 % [99]. The ductility did not always vary inversely with the yield strength, which indicates that both ductility and strength depend upon the multitude of microstructural parameters in a complex manner. Similarly wide variations in mechanical properties for the same alloy have been observed by other investigators [81,93].

It has been shown that microhardness, strength and ductility may be correlated with the fraction of primary or morphologically large γ regions [79] and these results are reproduced in Figure 1.8. These data clearly show that hardness and yield strength decrease with increasing proportions of primary gamma. The opposite is observed for the ductility - i.e. the tensile elongation prior to failure increases with increasing amounts of primary γ. Other studies have shown that the yield strength rapidly augments with increasing α_2 content [101], increasing from 400MPa for 0% up to 700MPa for 15%, *though details of the microstructural distribution were not given.* The yield strength has been shown to increase with decreasing grain sizes according to a Hall-Petch relationship [95,101]. Finally, the ductility has also been shown to dramatically increase with smaller grain sizes for both duplex [95,102] and lamellar structures [54,81,103].

Studies on lamellar colonies with a well-defined orientation have shown that the mechanical properties of the lamellar structure are sensitive to the orientation of the lamellae with respect to the loading direction [65,104-105]. Namely, *the yield strength is found to be very large for loading orientations*

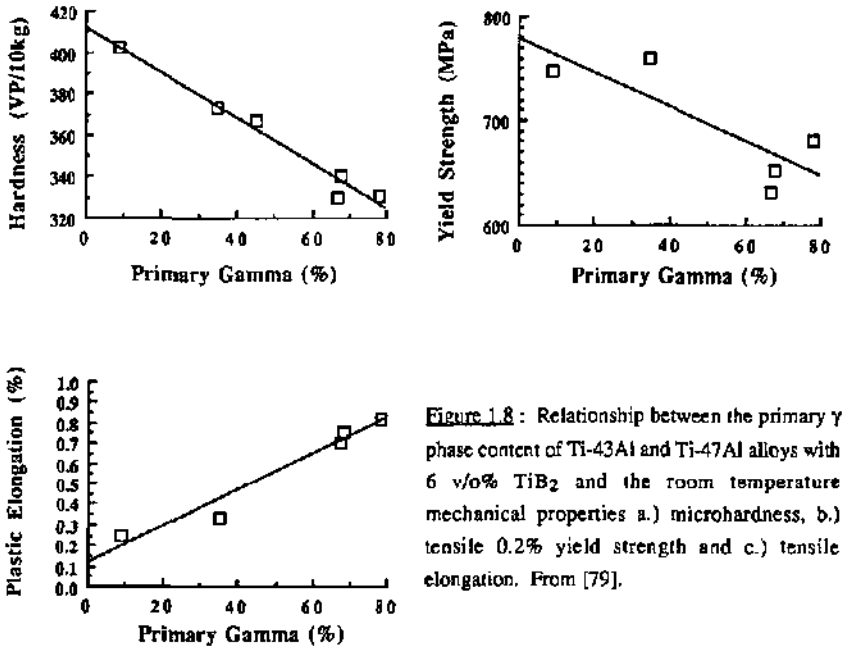

Figure 1.8 : Relationship between the primary γ phase content of Ti-43Al and Ti-47Al alloys with 6 v/o% TiB_2 and the room temperature mechanical properties a.) microhardness, b.) tensile 0.2% yield strength and c.) tensile elongation. From [79].

at angles of 0° and 90° from the normal to the lamellar plane, while the strength is a minimum at 45° [65]. The variation of yield strength is not symmetric around 45° such that the orientations of 90° are relatively stronger than the 0° orientations. This effect is even more pronounced in [105] which indicates that the effect could be related to lamellar thickness or alloy composition. These effects are summarized in Figure 1.9. Furthermore, the ductility varies inversely with the yield strength and plastic elongations up to 20% have been observed near the 45° orientation [65]. This clearly indicates that the γ phase in these lamellar structures is itself *ductile* and that the brittle behavior of lamellar structures must be related to interfacial effects, grain boundary effects or the deformation behavior of the α_2 phase. This dramatic difference in behavior with loading orientation has lead to the definition of two deformation modes [65]. The hard mode indicates that deformation proceeds on slip planes inclined to the lamellar plane and is predicted to be active for loading orientations near 0° and 90°. The high strength is then due to the large resistance of the lamellar boundaries to the propagation of shear. In contrast, the easy mode indicates that slip proceeds primarily on the {111} slip planes parallel to the lamellar interface and is dominant for loading orientations near 45°. This effect is, however, unable to explain the asymmetric behavior of the orientation - strength curve shown in Figure 1.9. It is important to note that deformation in the lamellar structure occurs predominantly in the γ phase as discussed in the following section.

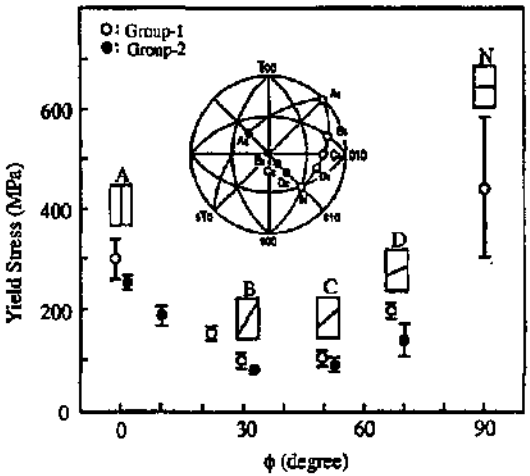

Figure 1.9 : Room temperature yield strength of PST (polysynthetically twinned) crystals as a function of the angle ϕ. ϕ is defined as the angle between the loading direction and the normal to the lamellar plane as schematically shown in the diagram. Taken from [65].

Finally, the yield strength of oriented lamellar crystals has also been shown to be strongly dependent upon the average lamellar spacing as shown in Figure 1.10. Although these data were measured on different binary alloys such that the volume fraction of α_2 phase was not controlled, they demonstrate, nevertheless, that the lamellar spacing will play an important role in the strength of lamellar structures.

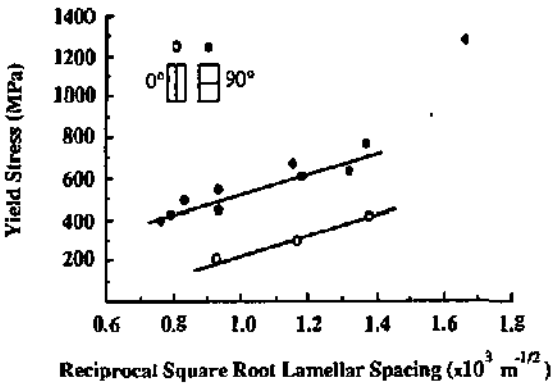

Figure 1.10 : Room temperature yield stress as a function of the reciprocal square root of the average lamellar spacing for binary alloys ranging from 48.1 to 51.6% aluminum. Note that the influence of the loading direction is again observed. Taken from [105].

In conclusion, it has been shown that the basic microstructure - property relationships in two-phase alloys are currently being developed. Based on the observations that

1.) the two-phase microstructures can be modified to achieve optimal combinations of mechanical properties and

2.) two-phase alloys exhibit much greater ductility than their single-phase counterparts,

it is clear that only the two-phase alloys possess the potential for successful commercial exploitation. However, more work is necessary in order to further understand the mechanisms underlying these structure - property relationships, especially from the standpoint of the mechanisms of plastic deformation.

1.4.4 Mechanisms of Plastic Deformation

The earliest documented deformation study of a two-phase material indicated that the deformation structure was dominated by 1/2<110] ordinary dislocations, while the <101] superdislocations were rare in comparison to single-phase materials [106]. Subsequently, many studies have attempted to link the enhanced ductility of the two-phase alloys to the corresponding deformation mechanisms. Table 1.2 provides a summary of the studies which have reported detailed deformation mechanisms for two-phase materials. All studies indicate that 1/2<110] ordinary dislocations and deformation twinning are the primary deformation modes. In contrast, the <101] superdislocations and faulted dipoles are generally not observed and the 1/2<112] dislocations are only infrequently encountered. Therefore, several important differences are observed between the deformation mechanisms for single-phase materials as summarized in Table 1.1 and the two-phase alloys in Table 1.2. It has, therefore, been proposed that the increased activity of twinning and the greater mobility of the ordinary dislocations is responsible for the improved ductility of the two-phase alloys [93,107]. This, in turn, has been correlated with decreased tetragonality of the unit cell with decreasing aluminum contents, reduced stacking fault energy with higher Ti/Al ratios [32] and the gettering of interstitial oxygen by the α_2 phase which alters the directional bonding of the γ phase [29,108]. Alloying with third elements may also result in improved ductility, however, it is unclear if these improvements are associated with further changes in the modes of deformation or if they are due to structural changes that may occur such as grain refinement or modification of the volume fraction of phases present [95].

While these general deformation mechanisms have been determined and appear valid for both equiaxed γ grains and the γ lamellae in equilibrium with the α_2 phase, the peculiarities of the deformation mechanisms in the lamellar structures have only recently been addressed. In these structures, synergistic effects between the two phases and may influence the deformation mechanisms. The mechanical properties of the lamellar structures outlined in the previous section indicate that the deformation behavior is complex. In addition to deformation in the γ phase, the deformation of the α_2 phase may also become important while the properties of the interfacial boundaries will be critical. The role of the interfaces has been shown to be both as potential sources for dislocation nucleation [70,73,99] and as obstacles for the propagation of slip between adjacent lamellae [64,73,81,95,99,105,109]. Indeed, it is believed that the transfer of slip across adjacent lamellae is the most important factor regarding the strength and ductility of the lamellar structures [64,99].

Investigator	Alloy	1/2<110] Ordinary	1/6<112] Twinning	<011] Superdisl.	1/2<112] Superdisl.	Stacking Faults
Huang [109]	Ti-48Al	many	many	n.a.	n.a.	n.a.
Vasudevan [110]	Ti-46Al	dominate	n.a.	n.a.	n.a.	n.a.
Vasudevan [30] *	Ti-50Al-0.4Er	dominate	observed	n.a.	n.a.	few
Hall [28]	Ti-48Al	majority	high density	n.a.	n.a.	n.a.
Huang [32]	Ti-46Al	few	observed	n.a.	n.a.	few
	Ti-48Al	dominate	numerous	n.a.	n.a.	numerous
	Ti-51Al	dominate	numerous	n.a.	n.a.	none
Sriram [34] *	Ti-48Al	high density	many	few	n.a.	n.a.
	Ti-50Al	high density	many	few	moderate	n.a.
Huang [95]	Ti-48Al-3V	many	many	n.a.	n.a.	none
	Ti-52Al-3V	many	many	n.a.	n.a.	few
Yamaguchi [64]	Ti-49.3Al	complementary mode	dominant mode	none	few	n.a.

Table 1.2 : Summary of the room temperature deformation mechanisms of two-phase TiAl alloys as reported by various investigators. n.a. indicates that this deformation mechanism was not analyzed or reported and * indicates studies on low oxygen materials.

Initially, it was believed that the α_2 phase deformed only slightly [69,108] or not at all [28,64,70] during deformation of the lamellar structures since it is the stronger of the two constituents. Therefore, little importance was attached to understanding the deformation characteristics of this phase. While it is generally accepted that the α_2 phase does deform less than the γ phase, it has recently been shown that the deformability of the α_2 phase may indeed be the factor which controls the strength of the lamellar structures [105]. It has also been suggested that the crystallographic relationship between deformation modes in both phases plays a decisive role in the ability of slip to transfer through the α_2 phase [105,110]. These crystallographic relationships could explain why some investigations have observed shearing [77,105] of the α_2 lamellae by deformation in the surrounding γ when others have not observed this [64,77,81,95,111]. Also, the thickness of the α_2 lamellae may be important in limiting the propagation of deformation across the lamellar colonies [70,101,110].

It has been shown that γ/γ interfaces present less resistance to the propagation of deformation [64,95,109]. The transfer of slip between differently ordered regions in the same lamellae has been shown to be rather easy [48,64] and Inui et. al. have reported that this transfer is facilitated by the possibility of slip continuity on the same plane with only a change in the direction of slip across the boundary. Several other works have shown that the impingement of a deformation twin at the interface may lead to the emission of dislocations in the adjacent grain [64,70,73,99]. However, no systematic study has been performed in order to look at the resistance of the various possible boundaries in a systematic way. Given the importance of the transfer of slip across the different types of boundaries, it is clear that this is an area that is relatively unexplored and certainly requires further study in order to advance the understanding of the deformation behavior of lamellar structures.

1.5 Deformation Models

1.5.1 Resolved Shear Stress for Single Crystals

One way to predict the active slip systems in a single crystal sample is through the application of the *Schmid law* which states that slip will begin for a given system when the shear stress on the slip plane and in the direction of slip exceeds a critical value. This critical value is known as the critical resolved shear stress, CRSS. In order to mathematically determine the shear stresses from an applied normal load, the angle between the direction of the axial loading and the slip direction, λ, plus the angle between the loading axis and the normal to the slip plane, φ must be calculated. These angles are shown in Figure 1.11 and equation 1.6 is then applied to calculate the resolved shear stress :

$$\tau = \sigma \cdot \cos\lambda \cdot \cos\varphi \qquad 1.6)$$

The term $\cos\lambda \cdot \cos\varphi$ is commonly referred to as the **Schmid factor, m.**

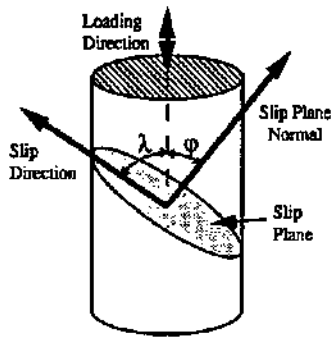

Figure 1.11 : Schematic diagram of the geometrical construction for the calculation of the Schmid factor, m. Once the angles φ and λ have been determined, the resolved shear stress for any slip system is easily calculated with the knowledge of the applied axial stress.

1.5.2 Geometric Compatibility for Polycrystalline Deformation

For deformation of polycrystalline materials, continuity must be maintained at the grain boundaries. This concept has gained widespread acceptance since it was first used by, von Mises [112], Taylor [113] and Bishop and Hill [114] to understand polycrystalline deformation behavior. The concept of continuity at the grain boundaries was first applied in order to predict the transfer of slip in adjacent grains by Livingston and Chalmers [115]. Starting with a set of continuity equations at the grain boundary, they sought to predict slip activation at a pile-up by considering slip as a homogeneous shear process. By considering slip in one grain as a homogeneous shear, it is possible to resolve this shear stress onto the slip systems in the adjacent grain according to the following resolution factor :

$$N = (e_l \cdot e_i)(g_l \cdot g_i) + (e_l \cdot g_i)(e_i \cdot g_l) \qquad 1.7)$$

where e is the normal to the slip plane, g is the slip direction, l represents the directions in the initial grain and the factor N is used to resolve the shear stress on the i slip system in the adjacent grain. This equation is derived directly from the rotation of the stress tensor onto the set of axes aligned with the slip system i. Using slip line trace analysis, it was shown that this calculation could be used to predict the additional slip systems in the boundary regions of bicrystals. The applicability of this concept has been further confirmed in the analysis of various bicrystals [116-117]. The parameter was also successfully used in two-phase brass bicrystals [118]. In each of these works, slip line trace analysis was applied and, thus, only indirect confirmation was obtained.

Only recently has this resolution parameter been applied in polycrystalline materials [119]. In this study, TEM examination was made in order to directly observe the active slip systems. During in-situ

observations, it was generally found that this parameter was *not* able to adequately predict transfer of slip across grain boundaries. In contrast, these authors found that the slip plane in the adjacent grain was predicted by the trace of slip plane on the grain boundary, while the slip direction was predicted by the full calculation of the anisotropic stress field associated with the pile-up. It was not made clear why the resolution parameter was successfully applied for the bicrystal slip transfer but did not seem to adequately apply in the polycrystal case. However, the authors did note that the types of grain boundaries present will play an important role. They were also able to show that the stress required for slip to transmit across the boundary varies greatly between different types of boundaries. For a geometric situation where the slip directions were collinear in the two grains, this stress was found to be a low value.

Both of the above approaches have emphasized the influence of the stress fields on the activation of slip systems in the adjacent grain. Contrarily, it is possible to predict the activation of slip systems on the basis that similar shape changes must occur in adjacent grains. Continuity at the grain boundary requires that :

$$\varepsilon_{xx}^{I} = \varepsilon_{xx}^{II} \qquad \varepsilon_{zz}^{I} = \varepsilon_{zz}^{II} \qquad \varepsilon_{xz}^{I} = \varepsilon_{xz}^{II} \tag{1.8}$$

where ε is the strain component indicated and I and II indicate the two grains separated by the boundary plane defined in the X-Z plane. Slip systems in the adjacent grains will most nearly fulfill these boundary continuity conditions only if the slip systems are geometrically compatible within each grain. When the slip systems are not compatible, additional strains will occur at the boundary which will result in large stress concentrations which must either be relieved by additional plastic flow or failure will ensue. Therefore, it is interesting to be able to determine the compatibility of deformation systems in adjacent grains. This compatibility can be defined by the introduction of a geometric compatibility factor which indicates the alignment or similarity of the slip systems. This geometric compatibility factor, designated as m', can be calculated from the knowledge of two angles : 1.) the angle between the slip directions in grains I and II, κ, and 2.) the angle between the normal to the slip planes, ϕ. A schematic representation of slip systems in adjacent grains is given in Figure 1.12 which clearly shows these two angles. The geometric compatibility factor is, thus, calculated as:

$$m' = \cos\phi \cdot \cos\kappa \tag{1.9}$$

Using this definition, the geometric compatibility of slip systems in adjacent grains may vary between 0 and 1. For m' = 1, complete compatibility exists between the slip systems in the adjacent grains and, in this case, both the slip directions and the slip planes in each grain will be parallel. Such deformation would be expected to be easily transmitted across the grain boundary. In contrast, m' = 0 indicates that the slip systems are completely incompatible such that either the slip directions or slip

planes are orthogonal. Such systems would be expected to result in unfavorable conditions at the grain boundaries. In general, m' will assume intermediate values between 0 and 1.

In order to calculate this geometric parameter, it is necessary to be able to express the appropriate directions in grain I in the grain II coordinate system. This can be done easily if the orientation relationship between the two grains can be defined by an appropriate rotational matrix, $\overline{R}$. Finally, the choice of the symbol m' in this text is used to emphasize the similarity of this factor with the *common Schmid factor, m. The Schmid factor represents the ratio of the resolved shear stress to the* axial stress. In a similar way, the compatibility factor, m', resolves the strain due to slip in grain I onto the slip systems in the adjacent grain II.

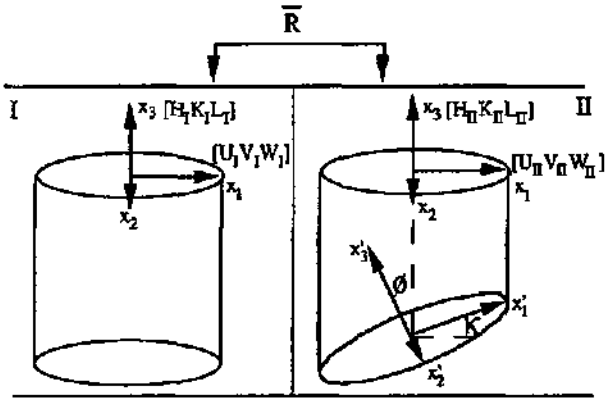

Figure 1.12 : Slip systems in adjacent grains showing the construction used for determining the angles used in the calculation of the geometric compatibility factor, m'.

2. Experimental Procedure

This section will provide the experimental details concerning the materials and methods of analysis used in this work. Of special importance are the procedures used in the transmission electron microscopy including the methods used for the determination of orientation relationships which permits the spatially consistent identification of deformation modes in adjacent grains.

2.1 Materials and Heat Treatments

The starting material for this study was graciously supplied by Alusuisse-Lonza (Neuhausen, Switzerland) in the as-cast form with a nominal composition Ti - 47.5 Al - 2.5 Cr (atomic percent). A disc 1cm thick and 10cm in diameter was removed from the bottom section of a larger cast billet and used for detailed study. Heat treatments were performed on slices 3.2 - 4.0 mm thick and 3-4 cm in length which were cut from the original casting. In order to minimize contamination during the elevated temperature heat treatment, the slices were encapsulated in quartz tubes which were evacuated and back-filled with argon several times prior to being sealed under argon at ≈2/3 atmospheric pressure.

Preliminary heat treatments were done in order to understand the development of microstructure. Subsequently, two heat treatments were selected for in-depth study :

I.) 1270°C for 64 hours.

II.) 1000°C for 168 hours.

Both alloys were cooled to room temperature in the furnace which resulted in a cooling rate of approximately 5°C/min. From the phase diagram shown in Figure 1.4, it can be seen that the first heat treatment was performed above the eutectoid temperature in the two-phase $\alpha + \gamma$ field, while the second was performed below the eutectoid temperature in the $\alpha_2 + \gamma$ field. After the heat treatment, the materials were removed from the encapsulation and the surface layers were mechanically polished to remove the slight oxidation layer that was created during the heat treatment. These slices were then subsequently machined into the appropriate dimensions for further study. Compression samples were made either by electrodischarge machining or mechanical grinding, while the other samples were sectioned with the diamond wheel.

2.2 Methods of Analysis

2.2.1 Optical Microscopy and Microhardness

Samples were mounted by conventional metallographic techniques and mechanically polished using a final polishing step with a 200Å alumina slurry. Chemical etching was done with a solution of 10 parts H_2O, 5 parts HNO_3 and 1 part HF (immersion for ~5s). For the microhardness messurement, mechanical polishing was performed as above. The Vickers hardness was then determined on unetched samples by applying a 200g load for 30s (loading and hold time).

2.2.2 Compression Testing

Compression testing was performed on cylindrical samples with a nominal diameter of 3mm and 6mm in length. The surface of the cylinder was used in the as-machined condition, while the end surfaces were mechanically ground until parallel. Compression tests were performed on a Schenck RSA universal testing machine in laboratory air at room temperature. The nominal crosshead speed was 0.1mm/min which corresponds to an initial strain rate of approximately $3x10^{-4}$ s^{-1}. Changes in sample length were measured with a gauge attached immediately adjacent to the sample on the compression ram and stationary block. Finally, all tests were interrupted at 1.5 to 2.0% plastic strain in order to observe the dislocation structures by transmission electron microscopy.

2.2.3 Bend Testing

3-point bending tests were performed to failure on samples which were nominally 3.0mm thick (parallel to the direction of the applied load), 3.5mm wide and 20mm long. A span length of 16mm was used. The sample surface was prepared by conventional mechanical polishing with the final polish of 200Å alumina slurry. The sample surface was optically examined prior to testing to ensure that all surface scratches were eliminated. The testing was performed under laboratory air at room temperature and with a constant crosshead displacement of 0.1mm/min. The stress and strain corresponding to the tensile side of the sample were calculated using standard equations.

2.2.4 X-Ray Diffraction

X-ray diffraction was used to confirm the phases present in the materials and to determine the lattice parameters. A Philips PW 1880 Diffractometer system operating at 40kV and 30mA with monochromatized $CuK\alpha$ radiation was used for this analysis. Step scans of 2θ from 20-100° were made with a step size of 0.005° and a count time of 10s at each step. Lattice parameters were calculated using the least-squares fitting method.

2.2.5 Electron Microscopy

For observation of the microstructure using scanning electron microscopy (SEM), samples were prepared as for optical microscopy. In addition, the final polishing step was done in an automatic container under gentle agitation with a 200Å alumina slurry. Observations were carried out on a Cambridge Stereoscan 360 using 15kV and a working distance from 14-16mm. Quantitative analyses using scanning electron micrographs were carried out with the aid of a Cambridge Quantimet 920 image analyzer.

For observations using transmission electron microscopy (TEM), discs 275µm thick were removed from the compression samples (ø3mm), perpendicular to the compression axis, using a diamond cut off wheel. After preparing uniform surface conditions using 1000 and 500 grit abrasive paper, the discs were electrolytically thinned into thin foils using a Tenupole twin jet polishing system. Two sets of conditions were found to give adequate results. An electrolyte of 8% perchloric acid (concentration 70%) in 92% methanol at -40°C with an applied tension of 13-15V was successfully used. Alternately, a 12 % perchloric acid (70%) and 35 % butoxyethanol in 53 % methanol electrolyte was used at -10°C and tension decreasing from 25 to 8 V during the thinning also yielded appropriate thin foils. Subsequent examination of the thin foils was carried out on a Philips CM12 electron microscope operating at 120kV. A double tilt stage (±40°, ±30°) was used for controlled tilting experiments.

2.3 Consistent Indexing Methods for TEM

A major emphasis in this work is the detailed determination of the orientation relationships between adjacent grains which subsequently allows a spatially consistent determination of deformation systems. Therefore, this section is devoted to describing the methods of specimen tilting, determination of the orientation relationships and matrix transformation operations used to relate the deformation systems in adjacent grains.

2.3.1 Controlled Tilting

Due to the lower symmetry of the $L1_0$ structure in comparison to the related fcc unit cell, the choices for indexing a zone axis corresponding to an observed diffraction pattern are correspondingly reduced. As discussed in Section 1.2.1 [110] ≠ [101] or [011], etc., thus, the diffraction patterns corresponding to these zone axes may also be distinguished. Using this information, in conjunction with an appropriate Kikuchi map, controlled tilting experiments may be performed within a single grain. Once an initial zone axis has been indexed, the specific indices of subsequent zone axes are defined by comparing the motion of the Kikuchi lines during tilting with the constructed Kikuchi map. Tilting between these zones is then accomplished by rotating along the necessary Kikuchi road - i.e. by keeping the electron beam parallel to the plane common to both zones during the entire rotation

operation. The Kikuchi map for the $L1_0$ structure along with the diffraction patterns for the important zone axes are given in Appendix 9.1. These tilting methods are identical to those described in standard texts - for example, see [120].

2.3.2 Definition of Orientation Relationships and Consistent Indexing of Adjacent Grains

In the manner described above, the orientation of any individual grain may be defined. However, for grains which are related by a specific orientation relationship, it is desirable to index the zones in a manner which is spatially consistent with the orientation relationship rather than treating each grain as an independent entity. In order to perform this indexing procedure, it is necessary to orient the thin foil so that the electron beam is simultaneously parallel to a zone axis within each grain. This is generally possible when the zones in the adjacent grains are contained within the plane of the rotation. For instance, with grains which are related by a rotation (a multiple of 60°) about $[\bar{1}\bar{1}1]$, if the electron beam is parallel to [101] in one grain, it will also be parallel to a <110> direction in the adjacent grain. [112] would also be parallel to a <211> in the adjacent grain, etc.

Now, in order to determine the unique orientation relationship between the grains and, at the same time, to index the zone axes in a consistent manner, it is necessary to identify at least two zones (preferably three) which are common in each grain and that lie within the plane of rotation. These diffraction patterns contain a common <111> reflection and this reflection is then subsequently used to define the pole of rotation. It is also desirable to locate another zone which is not contained within this plane to confirm the final analysis. The orientation of these zone axes and the position of any superlattice reflections which are present will then be used to determine the exact orientation relationships. This is most easily accomplished with the aid of a <111> standard projection such as that shown in Appendix 9.1 (Fig 9.2a). This projection is constructed such that the {111} plane of rotation (i.e. the common <111> reflection) is taken as the pole of the projection. In this manner, the zones which contain this plane are all located along the circumference of the projection. Rotation of a second projection by multiples of 60° relative to the stationary projection will then define the directions which are parallel in both grains. As an example, assume that the adjacent grain is rotated 60° about $[\bar{1}\bar{1}1]$ relative to the grain described by the stationary projection. This situation is shown in Fig 9.2b and it is readily seen that [101] in the initial grain is parallel to [011] in the adjacent grain, while [112] in the initial is parallel to $[\bar{1}21]$ adjacent. If the electron beam is oriented parallel to [101] or [112] in the original grain, the zones in the adjacent grain must then be [011] or $[\bar{1}21]$, respectively. In this manner, the presence of superlattice spots and the orientation of the zone defines the orientation relationship relative to the reference grain which has already been indexed using the standard techniques. Details about this method and further diagrams are given in Appendix 9.1.

Consequently, it is possible to construct a table which gives the predicted zone axes and their orientation as a function of rotation about, for example, the $[\bar{1}\bar{1}1]$. Three zones in the $(\bar{1}\bar{1}1)$ plane are

assumed to have been identified for the reference grain as $(2\bar{1}1)$, [101] and [112], respectively. Table 2.1 gives the zones which should be parallel to these zone axes in an adjacent grain. A fourth zone, for example of the <100> type, should also be located in each grain to confirm the analysis.

It can be seen that for the <112> type zones, only the presence of superlattice spots will give information about the rotation. In contrast, the <110> zones give information not only concerning the nature of the zone (i.e. <110] versus <101]), but the orientation of the zone will provide further information. For the 120° and 240° rotations, the orientation of zone B is the same in both grains since the ABCABC stacking sequence of the {111} planes is the same in both grains. In contrast, the orientation of zone B is rotated for the 60, 180 and 300° rotations since the ABCABC stacking sequence is changed to ACBACB in the adjacent grain. As a consequence, zone D (which is not contained in the plane of rotation) is not parallel for all rotations. This zone will be parallel only in grains rotated by 0, 120 and 240° or 60, 180 and 300°. Nevertheless, it is useful to examine a zone which is not contained in the $(\bar{1}\bar{1}1)$ plane since the position of the superlattice spots can be used to confirm that the correct indexing has been done. Hence, both the orientation relationship and the consistent indexing of the zone axes can done at the same time.

	0°	60°	120°	180°	240°	300°
A	$[2\bar{1}1]$	$[11\bar{2}]$	$[\bar{1}21]$	$[\bar{2}1\bar{1}]$	$[\bar{1}\bar{1}2]$	$[1\bar{2}\bar{1}]$
B	[101]	$[01\bar{1}]$	$[\bar{1}10]$	$[\bar{1}0\bar{1}]$	$[0\bar{1}1]$	$[1\bar{1}0]$
Orientation B.		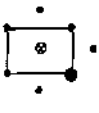				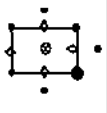
C	[112]	$[\bar{1}21]$	$[\bar{2}1\bar{1}]$	$[\bar{1}\bar{1}2]$	$[1\bar{2}\bar{1}]$	$[2\bar{1}1]$
D	[001]	[001]	$[\bar{1}00]$	$[\bar{1}00]$	$[0\bar{1}0]$	$[0\bar{1}0]$
variant	I - reference	II	III	IV	V	VI

Table 2.1 : Schematic diagrams of simultaneous zone axes in a $(\bar{1}\bar{1}1)$ plane of rotation in adjacent grains for various orientations. • represents fundamental reflections, ◊ superlattice reflections and ● the common $[\bar{1}\bar{1}1]$ reflection. Note that zones A, B and C are in the plane of rotation such that $A \wedge B = 30°$ and $B \wedge C = 30°$ about the $[\bar{1}\bar{1}1]$. However, zone D is located away from this plane and, consequently, does not contain the $[\bar{1}\bar{1}1]$ reflection.

It should also be noted that both the 60° and 300° or the 120° and 240° rotations are crystallographically equivalent rotations. For any two adjacent grains, the relationship could be equally described by 60° or 300° (or 60° clockwise rotation and 60° anti-clockwise). However, if a collection of more than two grains is examined, then there will be a difference between adjacent grains rotated by 60° or 300° and it is necessary to appreciate this difference in order to correctly determine the unique orientation relationships and relative deformation mechanisms in each grain.

2.3.3 Matrix Transformations

It should be noted that the convention used throughout this work is that the orientation relationship can be described as a rotation about the <111> direction which is perpendicular to the {111} plane of rotation (which has generally been taken as $[\bar{1}\bar{1}1]$). Using this convention, it can be seen that for a 180° rotation the [101] in the reference grain is parallel to $[\bar{1}0\bar{1}]$ in the adjacent, rotated grain, etc.[1]

Once the orientation relationship between two adjacent grains has been defined by the appropriate <111> pole and the rotation as a multiple of 60°, a transformation matrix may be easily calculated that allows all directions (and planes) in the reference grain to be converted to the coordinate system of the the adjacent grain. This rotational transformation matrix, $\overline{R}$, is given by [122] :

$$\overline{R} = \cos\theta \begin{bmatrix} 1 & 0 & 0 \\ 0 & 1 & 0 \\ 0 & 0 & 1 \end{bmatrix} + (1 - \cos\theta) \begin{bmatrix} c^1c^1 & c^1c^2 & c^1c^3 \\ c^2c^1 & c^2c^2 & c^2c^3 \\ c^3c^1 & c^3c^2 & c^3c^3 \end{bmatrix} + \sin\theta \begin{bmatrix} 0 & -c^3 & c^2 \\ c^3 & 0 & -c^1 \\ -c^2 & c^1 & 0 \end{bmatrix} \qquad 2.1)$$

where c^1, c^2, c^3 are the normalized indices defining the pole of rotation such that $(c^1)^2 + (c^2)^2 + (c^3)^2 = 1$ and θ is the angle of rotation. With this rotational matrix calculated, any direction in the reference grain, I, is transformed to the adjacent grain coordinates, II, by simple matrix multiplication. Since the <x,y,z> direction is orthogonal to the {u,v,w} plane in the cubic system, this matrix transformation applies equally well to the conversion of planes to another coordinate system.

These results may also be confirmed graphically using the projections given in Appendix 9.1. Using this transformation, it is easily seen that the same results will not be obtained for a 60° and 300° rotation in spite of the fact that these are crystallographically equivalent. Similarly, if a grain II is rotated 60° relative to a grain I, then grain I is *not* rotated 60° relative to grain II. This indicates that the sense of rotation between adjacent grains needs to be carefully preserved when specific determinations are to be made.

---

[1] This convention is not the same as that commonly encountered in standard textbooks - for example see [121]. These authors generally define the twin relationship such that $[101]_{matrix}$ is parallel to $[10\bar{1}]_{twin}$. However, this definition is not consistent with the fact that the twinned grain has been rotated about a fixed axis.

2.3.4 Foil Normal Determination

In order to determine the foil normal, a minimum of three zone axes were identified in the grain. The coordinate positions of the tilt stage could then be used to determine the angular tilt of each zone axis from the foil normal. With three directions and the angle of each direction from the foil normal, the foil normal can be readily determined using graphical or mathematical procedures. For instance, the foil normal may be determined graphically on the stereographic projection as the intersection of the three small circles drawn about the zone axes at the appropriate angles. It is estimated that the error in determining the angle from the zone axis is $\pm 3°$ such that the foil normal should be determined to within approximately $\pm 5°$. Since the thin foil discs were sectioned perpendicular to the compression axis, it is assumed that the foil normal will then roughly correspond with the compression axis.

3. Results : Materials Characterization

3.1 Microstructure

3.1.1 As-Cast Material

Figure 3.1(a) shows that the microstructure of the as-cast alloy at the bottom of the casting consists of a fine, equiaxed grain structure typical for the quench zone of a casting. Away from this quench surface which extends approximately 1mm thick into the casting, the microstructure consists of coarse, elongated grains typical of a dendritic structure as shown in Fig 3.1(b). These elongated grains are generally 100-500 μm wide and up to 2mm long. In both of these regions, the grains are composed of alternating lamellae of the γ and α_2 phases and are, thus, referred to as fully lamellar grains. The nature of this fully lamellar structure is more clearly visible in the scanning electron (SEM) micrograph shown in Fig 3.1(c). Finally, it should be noted that a small volume fraction of round particles (imaged black in Fig 3.1(c)) were distributed inhomogeneously throughout the as-cast material. EDS microanalysis showed that these particle consist mainly of aluminum and oxygen and are, thus, assumed to be aluminum oxide particles. These would only be expected when the γ and α_2 phases are fully saturated in oxygen. Their role during plastic deformation has not been investigated.

3.1.2 Heat-treated Alloys

The general microstructural features of the materials heat-treated at 1000°C for 168h are shown in the SEM micrograph of Figure 3.2(a). As will become visible later in the TEM micrographs, this microstructure consists mainly of equiaxed γ grains which are 5-30μm in size and, hence, will subsequently be referred to as the equiaxed microstructure. Distributed inhomogeneously throughout this matrix of γ grains (in correspondence with the original dendritic distribution) are many elongated α_2 particles. These particles are 1-2μm in width and up to 40μm long. Also seen are five coarse aluminum oxide particles which are 5-15μm in diameter and are usually spherical or blocky in shape. The size, shape and volume fraction of these particles is the same as in the as-cast material.

As-heat treated samples were also observed in the transmission electron microscope to identify any deformation structures due to thermal stresses created during the heat treatment process. A representative micrograph of the structures which have been observed in the equiaxed microstructure is given in Fig 3.2(b). In this micrograph, a deformation twin, a pile-up of ordinary dislocations, several superdislocations and a faulted dipole are all shown. While these defects will all be discussed in more detail in Section 4, it is important to note at this point that all of the possible deformation modes have been identified in the as-heat treated material. Although, the density of defects is usually rather low, a significant fraction of the as-heat treated grains contains deformation twins.

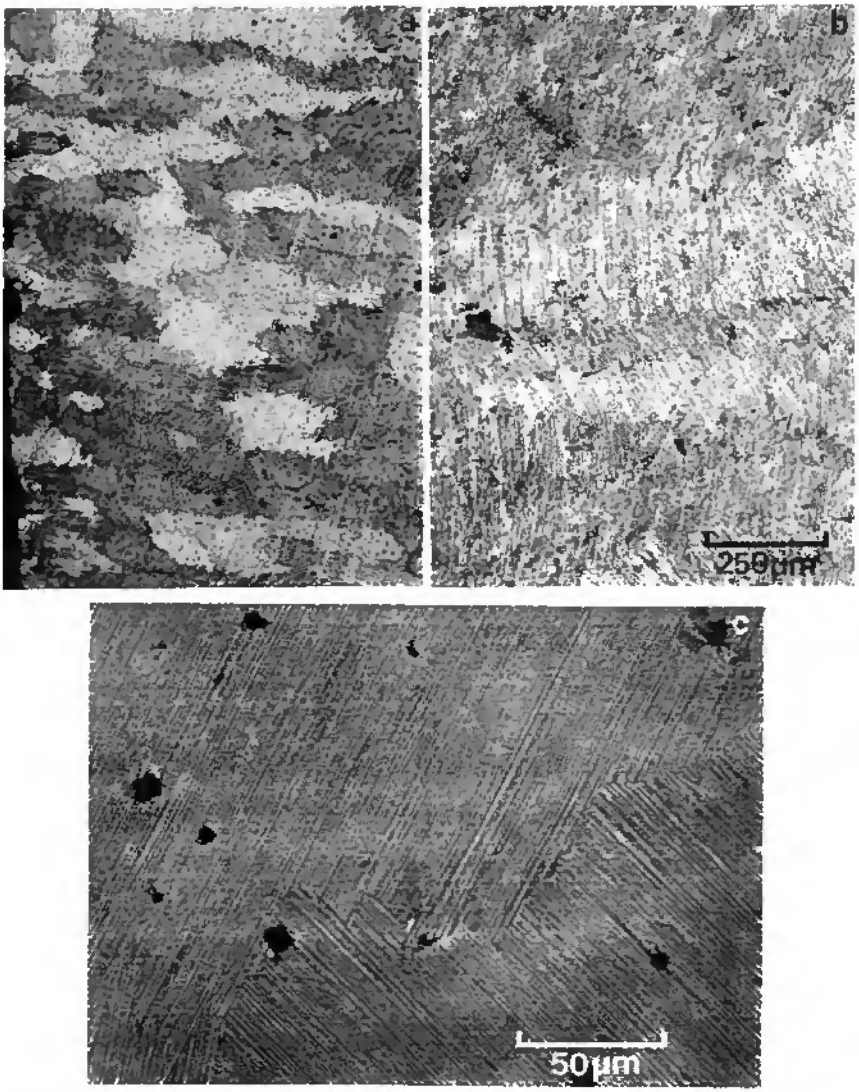

Figure 3.1 : Optical micrographs of the (a) quench side and (b) the interior of the casting. Details of the nature of the lamellar structure are evident in the SEM micrograph (backscattered mode) in (c).

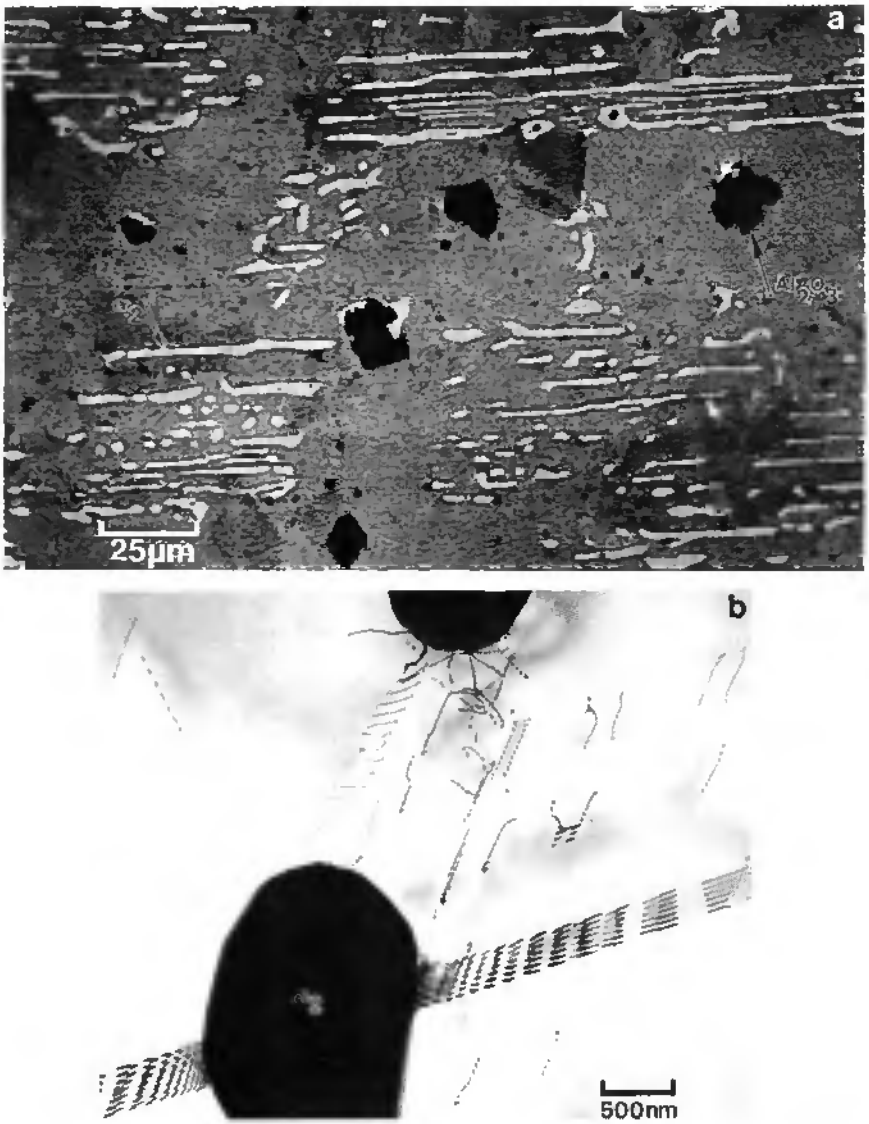

Figure 3.2 : *The equiaxed microstructure (1000°C, 168h) : (a) a SEM micrograph showing the* general features of the structure and (b) a TEM micrograph revealing the defect structures in the as-heat treated material.

The material heat treated at 1270°C for 64h has also been examined and a representative SEM micrograph is shown in Figure 3.3(a). The grain size and shape in this material is unchanged from the original as-cast state. This microstructure is seen to consist of a bimodal distribution of lamellae. The coarse lamellae which are imaged dark are γ lamellae and these coarse γ regions may consist of one or several individual γ lamellae and vary in width from 3-17 μm. The lighter gray regions are composed of fine lamellae of alternating α_2 and γ phases which are similar to the as-cast fully lamellar structure. Since this lamellar structure is made up of regions of fine lamellae plus the coarse γ lamellae, it is referred to as the **transformed lamellar** structure. It should also be noted that regions of discontinuous coarsening [123] can also be seen at the grain boundary. Finally, several aluminum oxide particles are again observed in the micrograph.

The microstructural features of this transformed lamellar microstructure are emphasized by the TEM micrographs shown in Figs. 3.3(b)&(c). In Fig. 3.3(b), a coarse γ lamella is shown which is approximately 7 μm thick. It can be seen that this region corresponds to a single, thick lamella, whereas it is more commonly observed that the coarse γ region consists of several individual lamellae. It should also be noted that the boundaries of these regions can be either flat, as demonstrated by the boundary to the left of the lamella, or rather irregular with fine lamellae ending at the coarse γ as seen at the boundary to the right. On both sides of this coarse lamella, fine lamellar regions consisting of alternating γ and α_2 lamella can be observed and which are shown more clearly in a higher magnification TEM micrograph, Fig 3.3(c). Viewed with the electron beam parallel to the interfacial plane, the alternating nature of the two phases is clearly seen. Due to absorption and diffraction effects, the γ phase is imaged lighter while the α_2 phase is darker and this identification was confirmed by diffraction analysis. As indicated by the arrow, adjacent γ lamellae may also be present with the fine lamellar structure; however, this is a rather uncommon feature. It can also be seen that the γ lamellae are generally thicker than the α_2 lamellae. The general nature of the deformation structures observed in the as-heat treated material is also clear in this figure. In the coarse γ lamellae, sporadically distributed individual dislocations and well defined dislocation networks can be observed, though the density of dislocations is generally low. Within the fine lamellar structure, many dislocations are observed at the lamellar interface as can be seen by the strong contrast behavior observed at the interface. In contrast, only few isolated dislocations can be observed within the γ lamellae, while no deformation structures were observed within the α_2 phase. It should be noted that, in contrast with the equiaxed structure, deformation twins were *not observed* in this heat-treated condition - neither in the coarse γ lamellae nor in the fine lamellar regions.

In order to quantify the distribution of phases in the heat-treated materials, quantitative microstructural analysis has been performed using scanning electron micrographs at a magnification of 500 times (observed area roughly 30mm^2). TEM micrographs were taken as necessary in order to determine the lamellar thickness and phase volume fractions in the fine lamellar structures. The transformed lamellar structure was found to consist of 48 vol% coarse lamellar regions (ave. thickness 7.7μm), 51% fine

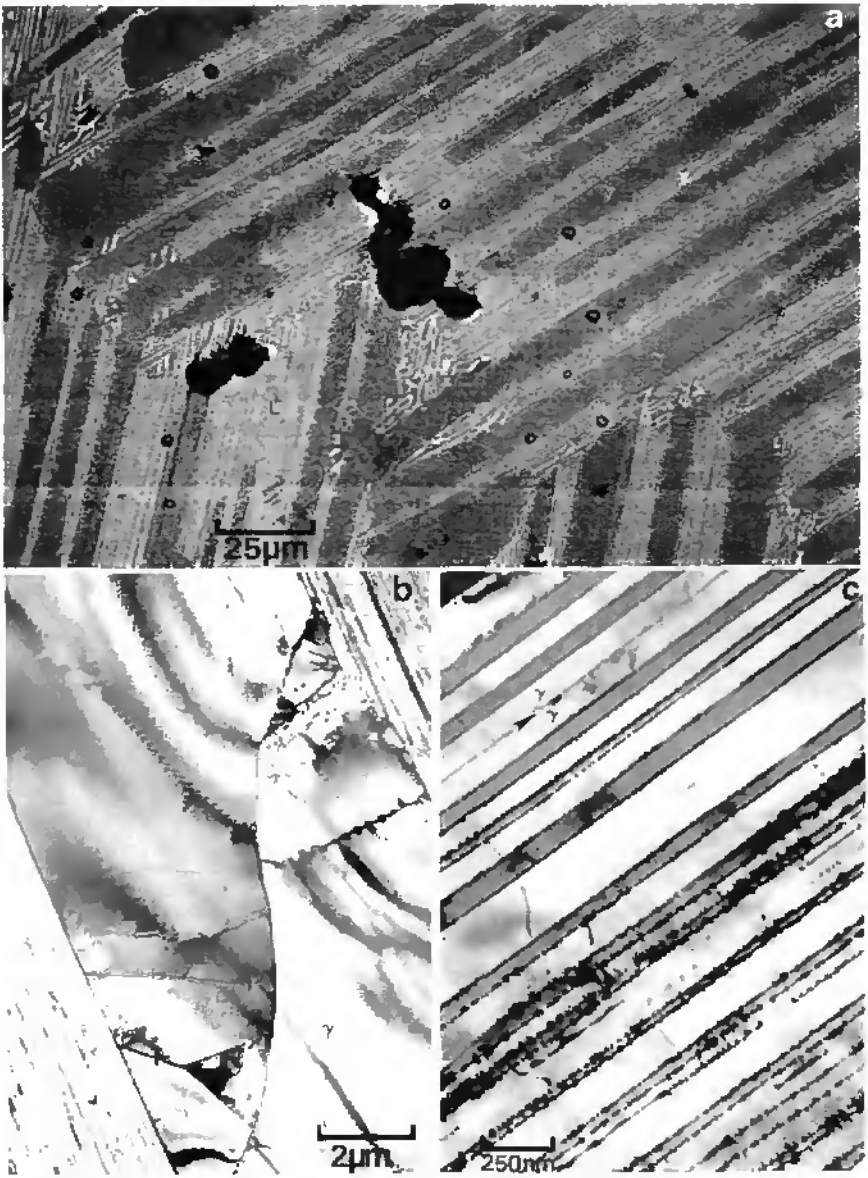

Figure 3.3 : The transformed lamellar microstructure (1270°C, 6.4h) : (a) SEM micrograph showing the general features of this structure and TEM micrographs revealing the defect structures in the coarse γ lamellae (b) and the details of the fine lamellar regions (c).

lamellar regions and 1.2% Al_2O_3 particles (ave. diameter 4.6μm). Within the fine lamellar regions of this structure, 30% were α_2 phase lamellae (51 nm thick), while the γ lamellae are approximately twice as thick (ave. 106 nm). In comparison, the as-cast structure contained 30% α_2 lamellae (115 nm), 68% γ lamellae (200 nm) and 1.6% Al_2O_3 particles. Finally, the equiaxed microstructure consisted of 89% γ grains (grain size between 5-30μm), 10 % elongated α_2 particles and 0.7% Al_2O_3 (5.0μm). Accordingly, the total volume fraction of α_2 phase for the three alloys is 10, 15 and 30 % for the equiaxed, transformed lamellae and as-cast, respectively. The fraction of oxide particles is similar in each material and varies between 0.7-1.6%. This variation is attributed to differences present already in the original as-cast sample and not to any effects created by the heat treatment itself.

It should also be noted that the lamellar structures in both the as-cast fully lamellar material and the heat-treated transformed lamellar regions consisted primarily of alternating γ and α_2 lamellae. Therefore, the dominant interface between lamellae is of the α_2 / γ type. The expected orientation relationship between these lamellae is always obeyed for the lamellar structures. Occasionally, two γ lamellae also come into contact in these lamellar arrangements as noted in Fig 3.3(c). In contrast, no orientation relationship existed between the α_2 and γ phases in the equiaxed microstructure.

Finally, X-ray diffraction was used to confirm the phases which were present and to determine the lattice parameters. Analysis on all alloys indicated that the principal phases present were the γ - TiAl phase and the α_2 - Ti_3Al phases as expected. Additionally, other minor peaks were observed which could be attributed to the α-Al_2O_3 phase corundum. These results, combined with the analysis of the oxide particles above, confirm that the observed particles are aluminum oxide Al_2O_3. The determined lattice parameters of the γ and α_2 phases were within the ranges given in the literature [94,124].

3.1.3 Orientation Relationships

The expected orientation relationship, $\langle\bar{2}110\rangle_{\alpha_2}$ // $\langle 011\rangle_{\gamma}$ and $(0001)_{\alpha_2}$ // $\{111\}_{\gamma}$, is *obeyed* in all the lamellar zones - i.e. for the as-cast fully lamellar structure as well as the fine lamellar regions in the transformed lamellar structure. This is readily verified in Figure 3.4 which shows that the $[\bar{2}110]_{\alpha_2}$ is parallel to the $[011]_{\gamma}$. In contrast, as previously stated, this orientation relationship did *not* exist in the equiaxed structure.

The orientation relationships between adjacent γ lamellae or grains will be presented in Sections 4.2 and 4.1, respectively. The dominant rotation between adjacent γ lamellae is of the true twin, 180° type, while the other rotations are encountered less frequently. In contrast to the lamellar structures, the probability of all three types (60°, 120° or 180°) is equal in the equiaxed structure.

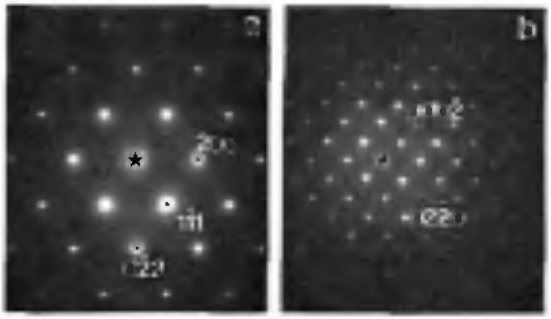

Figure 3.4 : SADPS which demonstrate the orientation relationship between lamellae of the α_2 and γ phases (a) $[011]_\gamma$ and (b) $[\bar{2}110]_{\alpha_2}$.

3.2 Mechanical Properties

A summary of the mechanical properties is given in Table 3.3. Microhardness and compressive properties were measured for the as-cast material and both heat-treated alloys, while bending tests were performed only on the heat-treated materials.

		compression	bending	
Structure	H_v, GPa	$\sigma_{0.2}$, MPa	$\sigma_{failure}$, MPa	$\varepsilon_{failure}$, %
as-cast	418 ± 19	740	---	---
equiaxed	339 ± 25	525	840	≈0.1
transformed lamellar	355 ± 24	605	460	<0.05

Table 3.3 : Microhardness, compressive yield strength and stress and elongation to failure in bending.

As can be seen from the table, both heat treatments lead to a reduction in strength and hardness compared to the as-cast condition. Moreover, both the microhardness and compressive properties indicate the same trend in strength - namely, the equiaxed structure exhibits the lowest strength, the transformed structure is slightly stronger and the as-cast structure exhibits the highest strength. Finally, the bending ductility of both alloys was quite low. For the transformed lamellar structure, no plasticity was observed and the samples fractured at a stress below the compressive yield strength. However, the equiaxed samples did show some plasticity and, thus, fractured at a much higher stress level. It is unclear if this low measured ductility can be attributed to a low intrinsic ductility of the materials or if it is due to an external effect such as the coarse oxide particles which are present in the current materials. In either case, it should be noted that the equiaxed structure was weaker than the transformed lamellar structure and it exhibited a greater tendency to deform prior to failure in bending.

4. Results : Deformation Studies

4.1 Equiaxed Microstructure

In this section, the deformation mechanisms identified in the equiaxed microstructure after compressive deformation at room temperature will be presented. It should be recalled that this microstructure was created by the heat treatment at 1000°C for 168h. Initially, an aggregate of four grains will be presented which will serve to identify some of the typical features of the equiaxed structure and present the basic methods of analysis. Subsequently, further details of the individual deformation mechanisms will be presented. Finally, the closing part of this section will summarize all of the results on this microstructure and attempt to relate the mechanisms of deformation to the grain orientation.

4.1.1 General Characteristics

An overview of the microstructure created by the 1000°C heat treatment is shown in Figure 4.1 which clearly reveals the equiaxed nature of this structure. Four neighboring γ grains can be seen as indicated by the letters A, B, E and F. The γ grain size is rather large ($\geq$10 μm) and round or elongated, coarse α_2 particles are frequently located at the boundaries between the γ grains. The interface between grains E and B seen at the far right of the Figure 4.1 can be seen nearly flat and appears to be regular and straight along some sections of the boundary. Contrarily, the interfaces A/E, A/F and E/F are seen more edge-on and are irregular or curved in nature. The boundary plane between these grains cannot be described by a plane. However, there exist well defined orientation relationships between each of the grains and these will be presented below. In contrast, the orientation relationship between the γ and α_2 is not retained in this structure and this results in an incoherent particle / matrix interface.

Significant stress concentrations exist within the α_2 phase as can be seen by the bending contours which radiate from the particle / matrix interface. However, no individual deformation structures have been identified within these particles. The active deformation mechanisms in the γ grains are seen to vary from grain to grain. While grains B and F deformed primarily by the glide of dislocations, A and E deform by profuse twinning. In addition, various deformation systems can be activated locally (usually at grain boundaries or in the vicinity of α_2 particles) and this is an important and general characteristic of the equiaxed microstructure. Since this collection of grains presents many generalities of the structure, the deformation mechanisms within each grain will be presented in detail. This analysis will also provide typical examples of the methods of identification used in this work. Finally, important distinctions are made between deformation mechanisms which are generally active throughout a given grain and those which are only found in localized regions of the grain.

Figure 4.1 : Four grains showing the typical deformation mechanisms in the equiaxed microstructure.

In order to define the orientation relationships between the grains, selected area diffraction patterns (SADP) were taken in each grain at various orientations as shown in Figure 4.2(a). For position 1, all grains were aligned with the incident beam parallel to a <101] type direction. However, the pattern in A is rotated 180° compared to B, E and F. For the tilt position 2, the beam is parallel to a <211] type direction in A, B and F, while E exhibits a <112] type zone axis. The common <111> diffraction spot in both zones in all grains is taken as the pole of rotation and the orientation relationships are defined using the method presented in Section 2.2.2. This common plane of rotation has been defined as $(\bar{1}11)$ and, hence, unique identification of the diffraction patterns can be subsequently carried out. Schematic representations of the zone axes identified at positions 1 and 2 are shown in Fig 4.2(b) with the specific reflections appropriately indexed. These diagrams clearly demonstrate the plane of rotation as $(\bar{1}11)$ which is represented by the large spots in the figure. These rotations defined by the first two zones can then be confirmed by the nature and orientation of a third axis, which in this case is a <001] type zone axis shown in Fig 4.2(a). Grain A is taken as the 0° reference orientation and rotations between individual grains can then be taken by adding or subtracting the necessary rotations. It should be noted that, in the strictest sense, the rotations are not fully described as a multiple rotation of 60° about <111> since an additional, 2-3° misorientation whose pole is not the primary <111> pole is superposed upon the primary 60° rotation. However, this secondary deviation is small and, therefore, inconsequential in comparison to the primary rotation.

With these orientation relationships defined, the specific deformation mechanisms of each of the grains will be examined. Shown in Figure 4.3 are the deformation mechanisms for grain B. In Fig 4.3(a), an overview is shown which reveals significant activity of dislocations on both sides of an elongated α_2 particle and two different twinning systems on each side of the particle. Only few twins were present in localized regions of this grain. The Burgers vectors of the dislocations immediately to the left of this particle are identified by the contrast experiments shown in Fig 4.3(b) to (d). Since all dislocations are invisible for 002g Fig 4.3(d), it is clear that only ordinary dislocations are present. In Fig 4.3(b), the $1/2[1\bar{1}0]$ dislocations are shown, while the 1/2[110] dislocations are visible in Fig 4.3(c). The preferred line direction for both types of dislocation is screw. However, trace analysis was performed on segments of the dislocations (usually the ends) which were not in screw orientation to identify the active slip systems as $1/2[1\bar{1}0](111)$ and $1/2[110](1\bar{1}1)$. These determinations must be made with due caution since these discontinuities in the line direction at the ends can be due to relaxation phenomenon at the foil surface and must not necessarily indicate the actual slip plane during deformation. Trace analysis was also used to determine the twin plane as (111). However, since these are the only three twins of this type within the grain, they are not considered to play an important role in the room temperature compressive deformation. Significant inhomogeneity of the deformation mechanisms were seen within this grain. In addition to these localized twins, shown in Fig 4.3(c) is an area of the grain which is to the left of the area shown in Fig 4.3(a) and borders an adjacent grain. Although only ordinary dislocations are identified in the region shown in Fig 4.3(a), significant activity of superdislocations is seen in Fig 4.3(c). This is

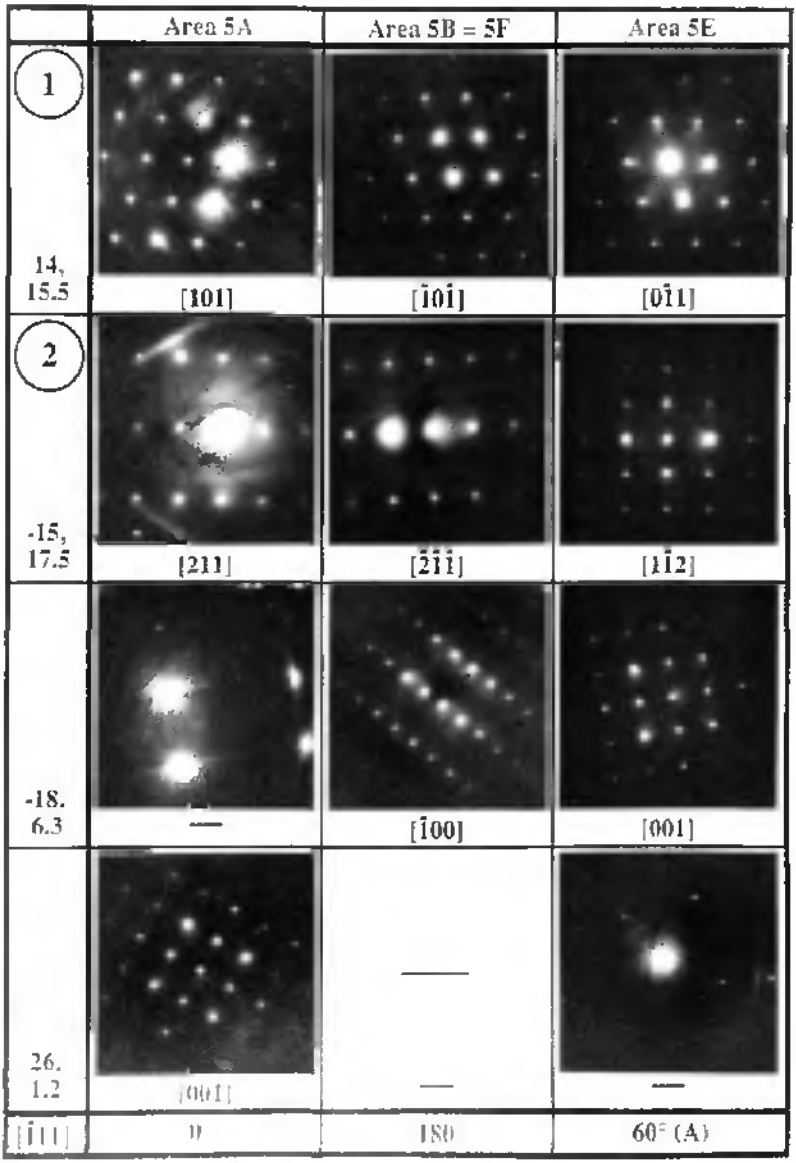

Figure 4.2(a) : Selected area diffraction patterns (SADP) corresponding to the grains A, B, E and F shown in Figure 4.1 obtained after tilting to the values of the angles (goniometer reading) shown on the left of the figure such that specific orientations were reached. From this series of SADPs, the specific rotations of each grain about the [$\bar{1}11$] axis have been measured as shown at the bottom.

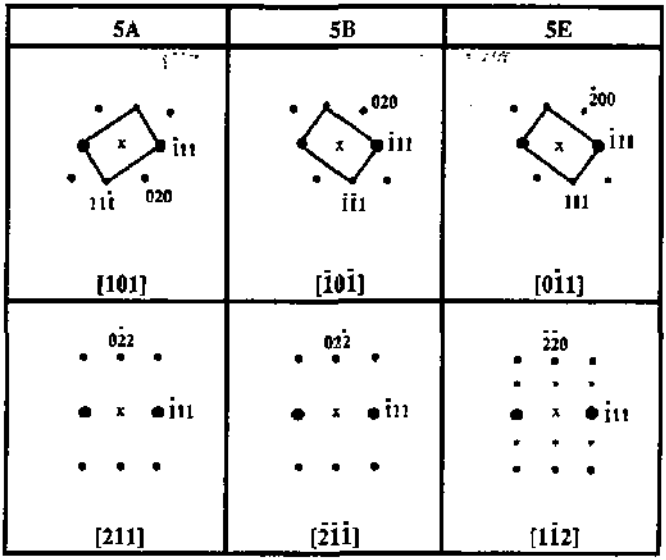

Figure 4.2(b) : Schematic diagram of the SADPs corresponding with the orientations 1 and 2 in Fig 4.2(a) with selected reflections identified. The large spots correspond with the plane of rotation and clearly show the rotation of the reflections about this plane. Solid spots are fundamental reflections while the starred spots indicate the position of superlattice spots.

readily verified since all dislocations visible with the 002g must be of a superdislocation type. Unfortunately, the foil thickness in this region prevented unique identification of the Burgers vector of these dislocations.

An overview of the grain F is shown in Figure 4.4(a). It can be seen that this grain is adjacent to two of the other regions - namely, grain E borders to the lower right side while grain A is to the lower left. Contrast analysis on the dislocations in the area near A (where the F is positioned in the micrograph) is shown in Fig 4.4(b) to (d). Virtually all of the dislocations are invisible in Fig 4.4(d) with the 002g which indicates that these are all ordinary dislocations. In Fig 4.4(b), the dislocations with b=1/2[110] (labelled 1) are visible, while in Fig 4.4(c) all the dislocations visible are of the type 1/2{$1\bar{1}0$] (labelled 2). The line direction was again near screw and trace analysis was used to confirm that segments of both types of dislocations can be found on both of the possible {111] glide planes. A zone along the A/F interface and well removed from this primary region, as indicated by the arrow in Fig 4.4(a), has also been examined. It can be seen in Fig 4.4(e) that many superdislocations are visible with a 002g. These dislocations are associated with the twins in A and do not propagate far into the grain F. Again, the foil thickness prevented identification of these dislocations; however, it is necessary to emphasize the point that the local activation of deformation modes which are different

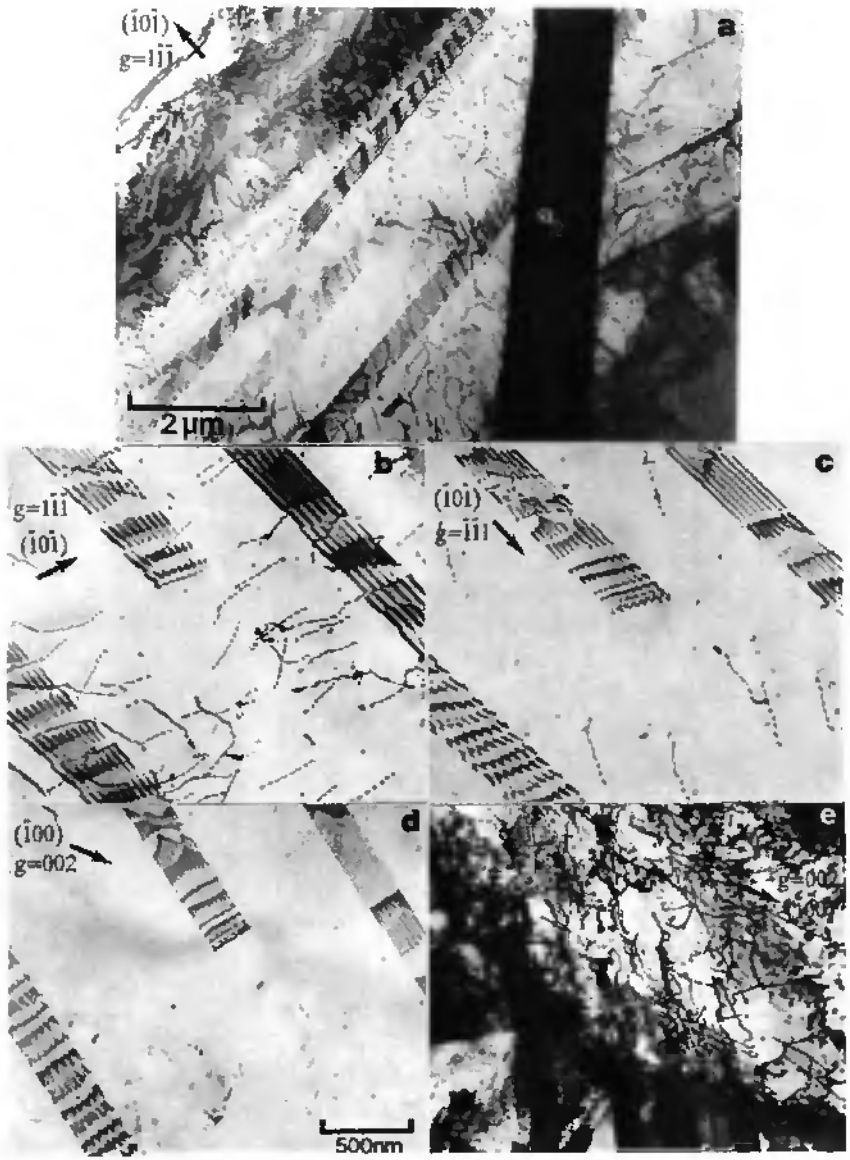

Figure 4.3 : Deformation mechanisms in grain B.

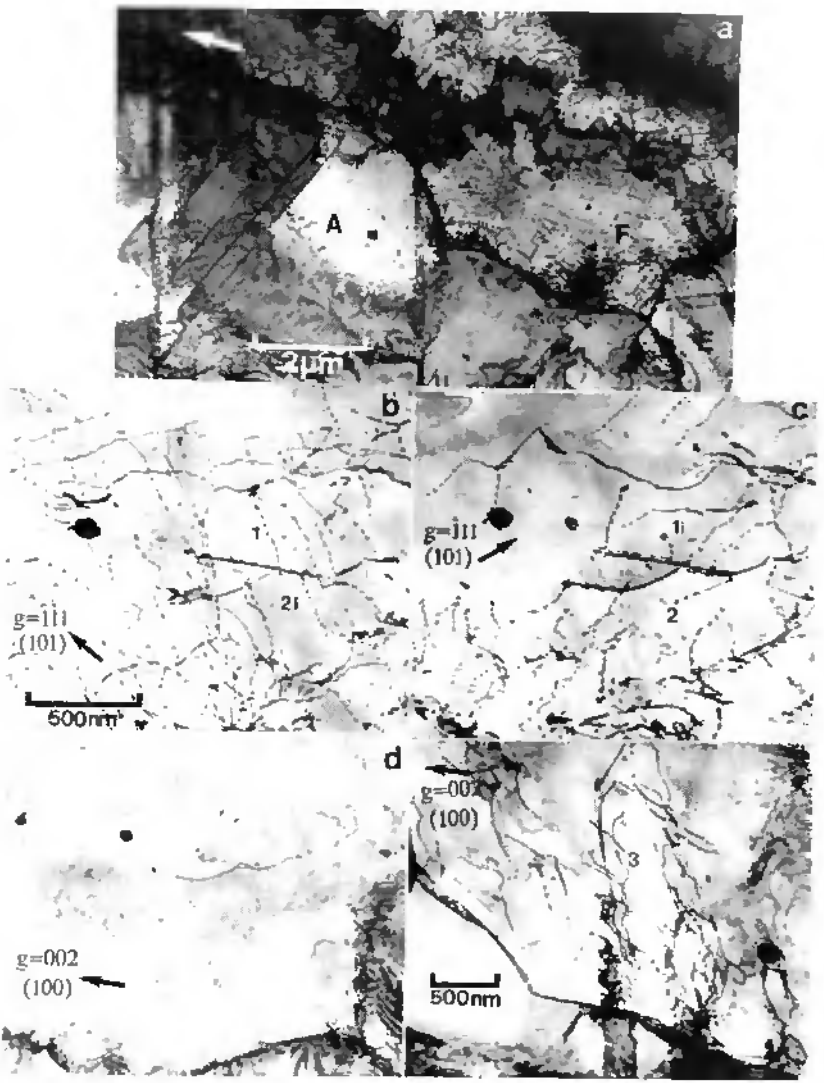

Figure 4.4 : Deformation mechanisms in grain F.

from the modes that are homogeneous throughout the grain is an important feature of the deformation of the equiaxed structure. This point will be discussed in more detail in Section 4.3.

It is appropriate to note that both grains B and F have the same orientation with respect to the compressive axis during loading (as shown in Figure 4.2) and that they also deform primarily by the glide of ordinary dislocations. This would indicate that, as a first approach, the grain orientation with respect to the deformation axis plays an important role in activation of the various possible deformation modes.

Overviews of area A are shown in Figures 4.5(a)&(b). Fig 4.5(a) shows that one twinning system is dominant in the grain near the A / F interface, while a second twinning system dominates the deformation structure in the region which borders area E as shown in Fig 4.5(b). In order to identify the active twinning systems and dislocations in this region, a more detailed analysis was performed on the area indicated by the boxed region at the right of Fig 4.5(b). Trace analysis was used to determine the twin plane of the system near area E as $(1\bar{1}1)$ since the twin plane is viewed parallel to the beam direction B=[121] in Fig 4.5(d). Similarly, the twinning system dominant near area F is confirmed to be on $(\bar{1}11)$ in Fig 4.5(c). The majority of the dislocations in this grain have the Burgers vector 1/2[110] since they are visible with 020g and invisible with $1\bar{1}1$g and $\bar{1}11$g Figs 4.5(d)&(e). Trace analysis showed the line directions of the dislocations to be near [121] and [011] (30° and 60° from screw orientation, respectively) and, thus, the glide plane is defined as $(1\bar{1}1)$. These dislocations were found to be homogeneously distributed throughout the entire grain which is in contrast to the activation of the twinning systems that are active in varying density depending upon the location within the grain. A minor number of dislocations with the Burgers vector $1/2[1\bar{1}0]$ were identified to be on the (001) plane; however, due to the low density of these dislocations plus the fact that (001) is not expected to be a glide plane at room temperature, it is assumed that these were created during thermal treatment or the subsequent cooling process.

Finally, it is necessary to identify the deformation mechanisms in grain E as shown in Figure 4.6. Two twinning systems are active throughout this grain and a lesser number of dislocations are present as shown in Fig 4.6(a). Two regions selected for further analysis are indicated in Fig 4.6(a) with the numbers 1 and 2. Analysis of area 1 (Figs 4.6 (b)-(d)) showed that the direction of intersection of the two twin planes is [011] and this fact, combined with trace analysis of the twin plane, determines the twin planes as $(1\bar{1}1)$ and $(\bar{1}\bar{1}1)$ as indicated in Fig 4.6(d). The preferred line directions of the twinning partial dislocations are screw and 15° from screw, respectively. The dislocations in Figs 4.6(b)&(c) become invisible with $1\bar{1}$g, thus defining b=1/2[110]. The preferred line directions are near $[\bar{2}11]$, $[\bar{1}01]$ and [011] (30° and 60° from screw, respectively) which defines the slip plane as $(1\bar{1}1)$. These dislocations are present throughout the grain in a low density. In contrast, a second type of dislocation is seen only locally, as for example in area 2, and is described by $b=1/2[1\bar{1}0]$ as shown in Figs 4.6(e)&(f). These dislocations are near the twin / twin intersection and have been

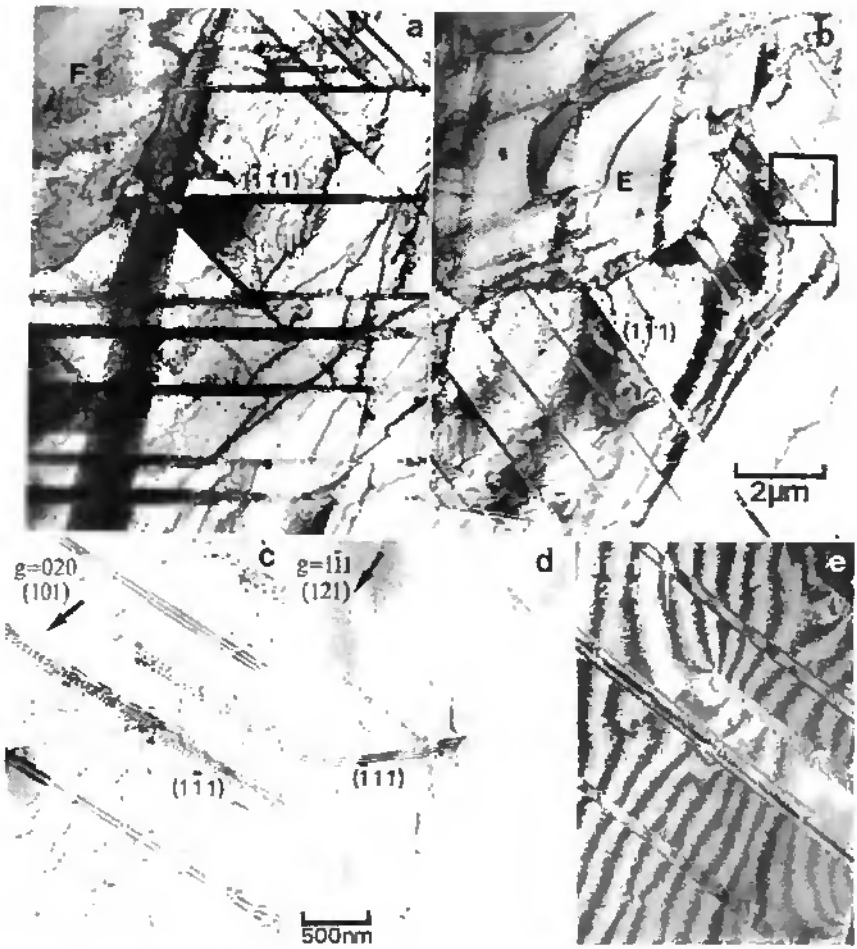

Figure 4.5 : Deformation mechanisms in grain A.

determined to lie on the (001) plane. However, it is not clear whether these are due to the twin intersection process or were created during the heat treatment since dislocations on (001) would not be expected for this twin intersection geometry. Another example of localized deformation is seen in an area to the right of the area shown in Fig 4.6(a). This region is shown in Fig 4.6(g) where twinning on the (111) and ($\bar{1}$11) planes, as indicated by the arrows, is identified *only* in this region surrounding

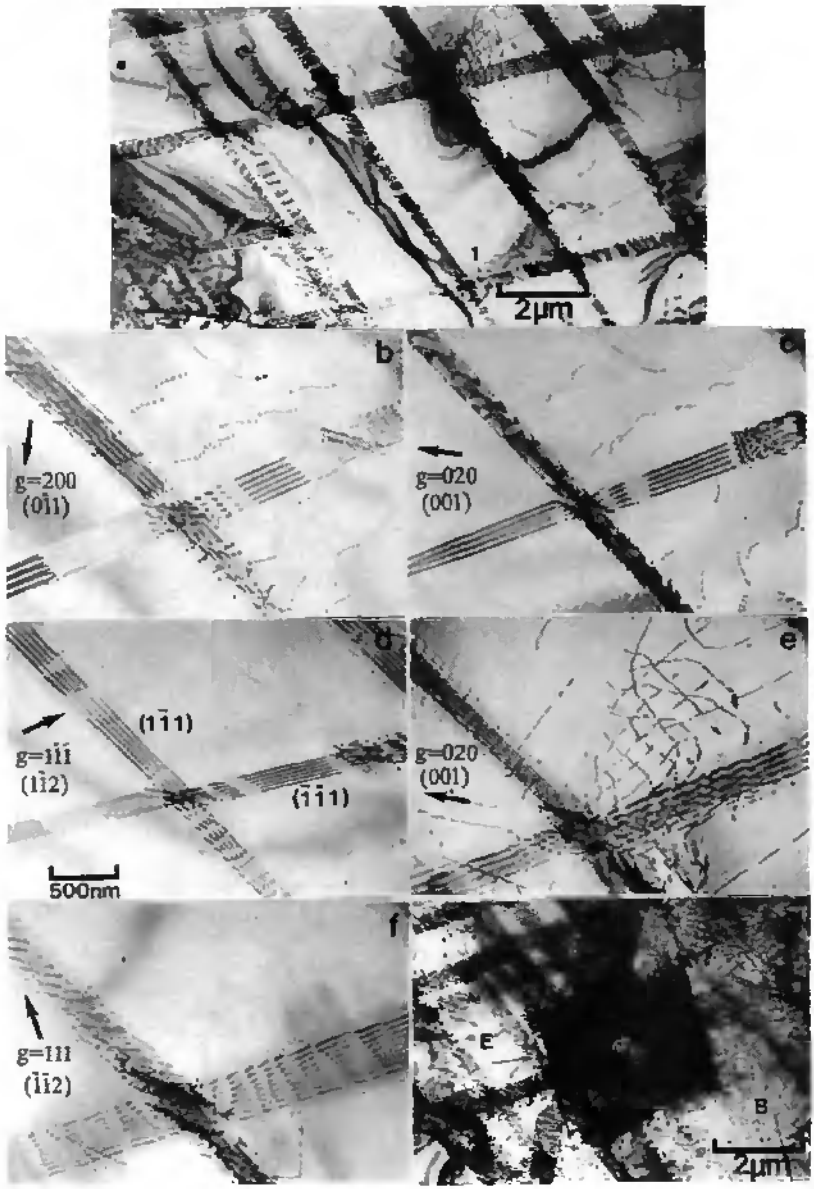

Figure 4.6 : Deformation mechanisms in grain E.

the α_2 particle. Hence, it has been shown that ordinary dislocations, superdislocations and twinning can all be locally activated depending upon the specific stress distribution within the grain.

A summary of deformation systems which were found to be homogeneously active throughout each of the grains is given in the schematic diagram shown in Figure 4.7. Also given in the figure are the orientation relationships between the grains defined as a rotation about [$\bar{1}$11] and the Schmid factor, m, for each of the deformation mechanisms. In a general manner, it can be noted that the active deformation systems correspond to the possible systems with the largest resolved shear stress. However, exceptions to this statement occur regarding the activation of superdislocations. For instance, Table 4.1 gives the Schmid factors for the observed twinning and ordinary dislocation systems and the highly stressed superdislocation systems which were *not* observed (or seen only locally as in Fig 4.3(e) or Fig 4.4(e)).

	Mechanism	Grain A	Grain B = F	Grain E
Observed	ordinary 1/2<110] dislocations	.32	.48 .47	.22
	twinning systems	.34 .29	-	.47 .46
Not Observed	superdislocations <101]	.45 .37	.34 .32	.50 .48
	superdislocations 1/2<112]	-	.26	.34

Table 4.1: Schmid factors for the ordinary dislocation and twinning systems which were observed in the grains A, B, E and F. Also listed are the Schmid factors for the most highly stressed superdislocation systems which were *not* active.

As can be seen in the table, there exist several highly stressed superdislocation systems in each grain which could be expected to be activated solely on the basis of resolved shear stress calculations. However, these systems are not activated and this demonstrates that twinning and glide of ordinary dislocations are the preferred deformation modes. Hence, in addition to the resolved shear stress, other factors such as elastic energy, Peierls lattice fraction and considerations of the mobility and fault energies of these dislocations must play a role in activity of the mechanisms. Likewise, propagation of 1/6<112] partial dislocations to form a twin appears to be more favorable than glide of 1/2<112] dislocations since the former has been observed in spite of the fact that the resolved shear stress on a 1/2<112] superdislocation would be the same.

Finally, it is appropriate to conclude this section with a brief synopsis of some of the essential features of deformation in the equiaxed microstructure:

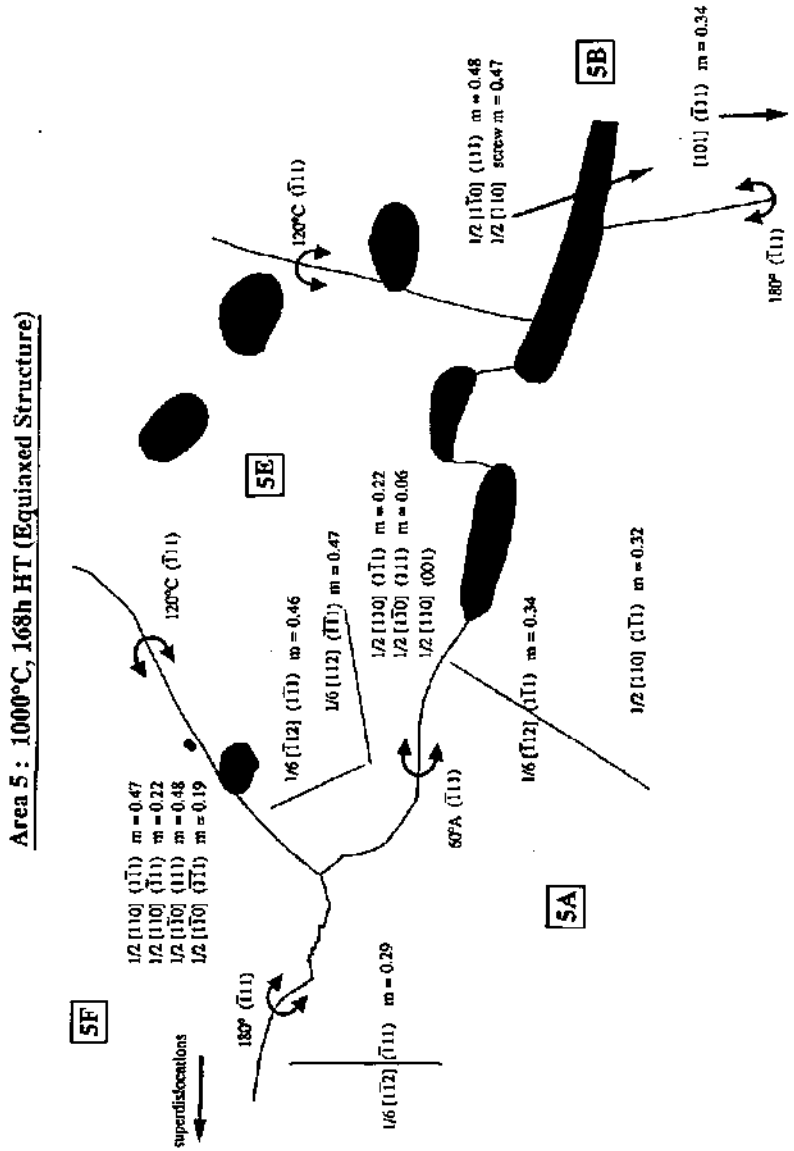

Figure 4.7 : Schematic diagram of the four grains shown in Fig 4.1 with the deformation mechanisms identified in each grain and the corresponding Schmid factors.

1.) several deformation systems are active within each grain which vary from grain to grain.
2.) generally, 1/2<110] ordinary dislocations and twinning are the preferred deformation modes.
3.) the active deformation systems can generally be predicted by calculation of the Schmid factor. However, this is certainly modified by the energy and critical resolved shear stress of the specific system as discussed above.
4.) significant local activation of additional systems near grain boundaries or α_2 particles is possible depending on the local stress distribution.
5.) the α_2 phase does not deform and, as such, is only a source of stress concentration which is partially relieved by flow in the surrounding γ phase.

4.1.2 Role of Twinning

In order to completely describe the active twinning systems, it is necessary to determine both the twin plane as well as the partial dislocation responsible for the twin shear. In the previous section, only the twin plane was determined and the shear direction was taken to be <112] in accordance with the requirements of ordered twinning in the $L1_0$ structure [21-22]. However, it is necessary to verify this assumption by performing detailed contrast analysis of the twinning partial dislocations.

It is generally difficult to identify the partial dislocations with the twin fault in contrast since the visibility criterion for partial dislocation overlapping a stacking fault are complex and sensitive to the deviation parameter, foil thickness and depth in the foil [125-126]. However, when diffraction conditions are used with the twin stacking fault is invisible - namely $\mathbf{g}\cdot\mathbf{R_F} = 0, \pm 1$ or ± 2 - the twin partial dislocations may be directly analyzed. Analysis of this type is presented in Figure 4.8 which shows a small segment of twin in grain E (Fig 4.6) on the $(1\bar{1}1)$ plane. The first step in the identification process is to assure that this fault indeed corresponds to a region of twinned material and is not just an arrangement of overlapping stacking faults. This can usually be done by tilting the twin so that the incident beam direction is parallel to the twin plane (i.e. edge-on) to verify that a finite region of twinned material exists and the nature of the twin can be verified by the appropriate rotation of the lattice as seen in the diffraction patterns. Since it was not possible to tilt the current twin into the edge-on position, verification of the twinned material was obtained through knowledge of the twin plane. For a twin on the $(1\bar{1}1)$ plane, the appropriate matrix transformation was used (as given in Section 2.3.3) to calculate that the $[1\bar{1}0]$ zone of the twin is parallel with the $[1\bar{1}4]$ zone in the matrix. Diffraction patterns taken in the matrix with B=$[1\bar{1}4]$ and in the twin, as shown in Figs 4.8(b)&(c), confirm that a region of twinned material exists.

Hence, the twin was imaged using four conditions of fault invisibility as shown in Figs 4.8(d)-(g). For the 220g and 311g the partial dislocations are invisible, while for $\bar{1}31$g and $\bar{3}11$g the partials are visible. Since the twin plane has been determined to be $(1\bar{1}1)$, the partials must be one of the three Shockley partials in this plane. A summary of the observed and predicted contrast for these partial dislocations is given in Table 4.2.

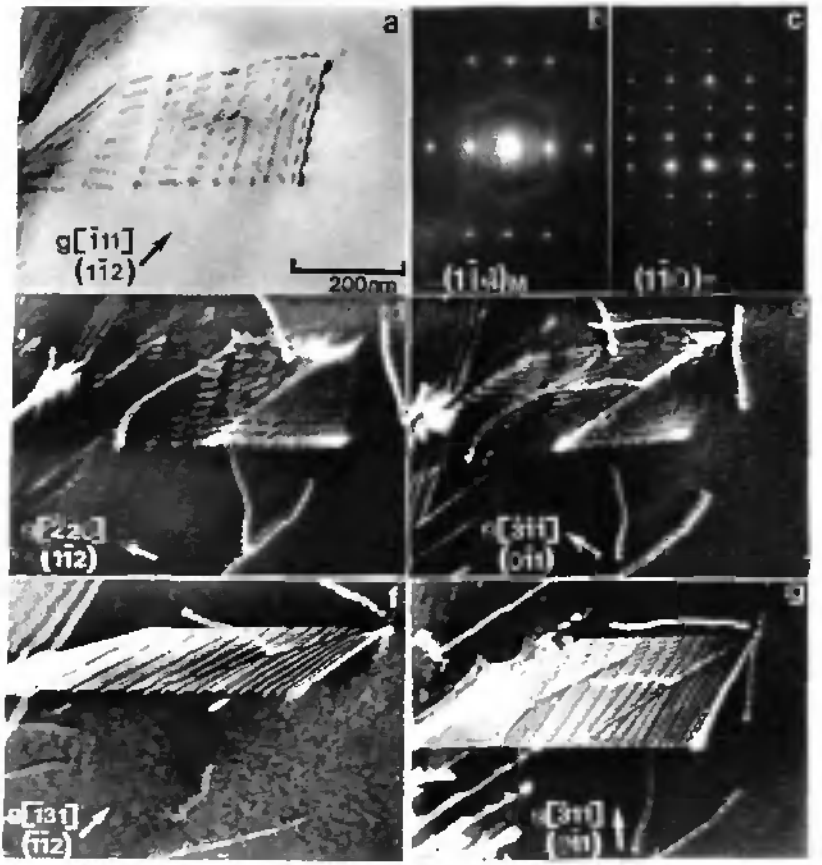

Figure 4.8 : Detailed analysis of the twin partial dislocations. (a) *BF* image of a ($1\bar{1}1$) deformation twin, (b) the ($1\bar{1}4$) matrix and (c) ($11\bar{2}0$) diffraction patterns, (d) - (g) weak beam analysis with stacking fault invisibility such that the twin partial dislocations may be directly identified.

In Table 4.2, the observed contrast fully matches the contrast expected for a 1/6[$\bar{1}$12] partial dislocation. Hence, the twinning system can be uniquely defined by 1/6[$\bar{1}$12](1$\bar{1}$1). This indicates that only twinning of the type 1/6<112]{111} is possible in this alloy and for the experimental conditions under investigation.

g	experimental	$g \cdot b_p$ 1/6[$\bar{1}$12]	$g \cdot b_p$ 1/6[121]	$g \cdot b_p$ 1/6[2$\bar{1}$1]
$\bar{2}\bar{2}0$	invisible	0 invis	-1 vis	-1 vis
$\bar{3}\bar{1}\bar{1}$	invisible	0 invis	-1 vis	-1 vis
$\bar{1}31$	visible	1 vis	1 vis	0 invis
$\bar{3}11$	visible	1 vis	0 invis	-1 vis

Table 4.2 : Observed contrast for the twin partial dislocations plus the values of $g \cdot b_p$ for the three Shockley partial dislocations on the (1$\bar{1}$1) plane and the predicted image contrast [127].

The line direction of the twinning partial is important since it may play a role in the mobility of the dislocation and, hence, affect twin propagation. As previously mentioned, the twinning partial tends to align along the screw orientation. For a total of 14 twins in which the orientation of the partial was determined, three lie almost exactly in screw orientation, five almost exactly in 30° from screw (along a <101] direction), five in intermediate orientations between 0-30° and one at 60°. Thus, it is clear that near screw orientations are favorable in almost all grains and under all loading conditions.

In several grains, it appears that the twins are able to propagate in both directions within the grain. This is an unexpected result since polarity of the twinning process exists for single-crystals [128-129] and would be expected to apply in polycrystal samples as well. An example of this opposite sense of propagation is observed for the (1$\bar{1}$1) twinning in grain E (Fig 4.6). Figure 4.9(a) shows a twin which initiates at the twin / matrix interface and appears to propagate in an upward direction. In contrast, the twin adjacent to the boundary with grain A appears to propagate downward, Fig 4.9(b).

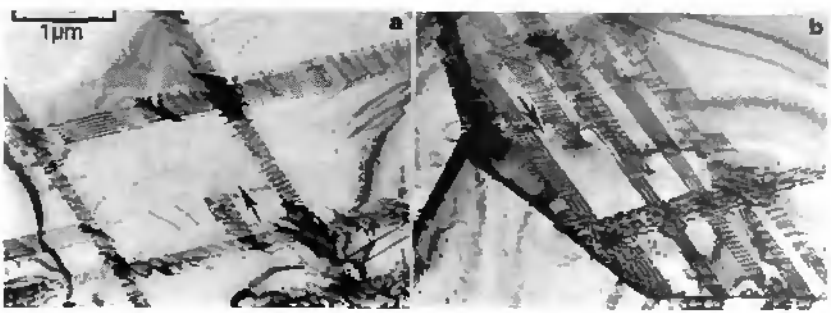

Figure 4.9 : Apparent propagation of (111) twins in the opposite sense (grain E). In (a), the twin appears to propagate in an upward sense, while in (b) a downward sense of propagation is observed.

Using the identification methods shown previously, the partial dislocations of both twins have been determined to be parallel to [$\bar{1}$12]. Additional bright field experiments were performed in order to provide further identification of the twin partials and to exploit the contrast asymmetry associated with

$\mathbf{g}\cdot\mathbf{b}_p = \pm 2/3$. The results of these bright field, $\pm g$ experiments are shown in Figure 4.10 for presumed values of $\mathbf{g}\cdot\mathbf{b}_p = \pm 1/3$ and $\mathbf{g}\cdot\mathbf{b}_p = \pm 2/3$. The images for the upward twin in Fig 4.9(a) are shown in the left column of Fig 4.10, while the downward twin images in Fig 4.9(b) are shown in Fig 4.10 at the right. Also, the diffraction conditions indicated on the left micrograph apply equally to the right micrograph. For all micrographs, the value of the rocking parameter, $w = s\cdot\xi_g$, was controlled between 1.0-1.4. Experiments were conducted to investigate the influence of w on the contrast behavior, however, these did not bring any additional information and are not presented here. A summary of the experimental observations of the first partial dislocation is given in Table 4.3 along with the contrast expected for possible partial dislocations.

	Observed Contrast		$\mathbf{g}\cdot\mathbf{b}_p$ for possible partials			
g	Upward	Downward	1/6[$\bar{1}$12]	1/6[1$\bar{1}\bar{2}$]	1/3[$\bar{1}$12]	1/3[1$\bar{1}\bar{2}$]
$\bar{1}$11	vis	vis	+2/3 vis	-2/3 in	+4/3 in	-4/3 vis
1$\bar{1}\bar{1}$	invis	invis	-2/3 in	+2/3 vis	-4/3 vis	+4/3 in
$\bar{2}$00	invis	invis	+1/3 in	-1/3 in	+2/3 vis	-2/3 in
200	invis	invis	-1/3 in	+1/3 in	-2/3 in	+2/3 vis

Table 4.3 : Observed contrast for the upward and downward twins (Fig 4.10) compared with the value of $\mathbf{g}\cdot\mathbf{b}_p$ and expected visibility of the possible partial dislocations [127].

From Table 4.3, it can be concluded that the 1/3 type partial dislocations are not possible since the characteristic image asymmetry for $\pm 4/3$ is not observed for the $\pm g$ experiments with 200g. Thus, it would appear that both partial dislocations are 1/6[$\bar{1}$12] by comparison of the observed and predicted contrast behavior. However, it must be noted that the contrast rules defined for the visibility conditions of +2/3 or -2/3 are defined for a partial dislocation to the right side of the stacking fault [126-127]. When the partial dislocation is to the left of the fault, these visibility conditions are reversed. Based on this criterion, it would appear that the two partial dislocations are, thus, of opposite sign. However, this rule was determined by Clareborough for stacking faults bound by unlike Shockley partial dislocations. In contrast, Silcock noted that the contrast behavior of the partial dislocation on the right and left side of a faulted loop was identical when the fault was surrounded by a Frank partial dislocation [128]. This latter work needs to be applied to analysis of the present twinning since these twins must correctly be considered as loops. This loop should then show similar contrast on both the left and right side in accordance with Silcock, as was correctly observed experimentally. The apparent opposite sense of propagation is only an effect created by viewing the projection of an expanding twin loop. Crystallographically, the sign of the partial dislocation is the same around the entire loop as it must be, while the projected direction of motion will clearly depend on which part of the loop is observed. Careful analysis of these contrast experiments, therefore, is fully consistent with the polarity of the twinning process and verifies that only passage of 1/6<112] partials in the defined sense creates a twinned crystal. The complexity of this contrast analysis clearly shows the need to 1.) consider how the projected two-dimensional image of electron micrographs

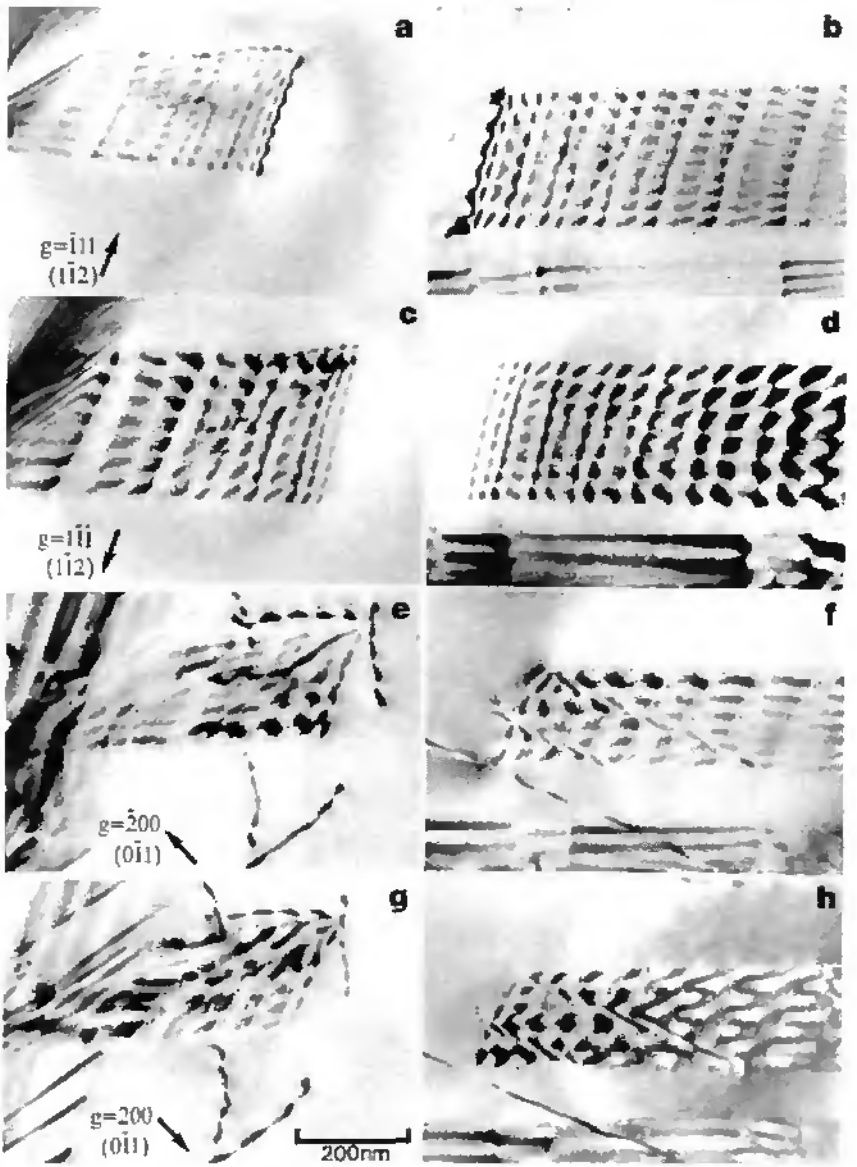

Figure 4.10: Detailed analysis of the twins which appear to propagate in the opposite sense as shown in Figure 4.9. Micrographs at the left correspond with the upward twin in Fig 4.9(a), while the micrographs at the right are of the downward twin in Fig 4.9 (b).

compares to the three-dimension physical event and 2.) to apply generalized contrast rules only with extreme caution and to verify the conditions under which these rules may apply.

It can be concluded that twinning plays an important role in the deformation behavior of the equiaxed structure. Twinning may either be present homogeneously throughout the grain or be active locally to relieve stress concentrations (for example, see Fig 4.6). An example of the importance of twinning deformation is shown in Figure 4.11 where all four twinning systems can be identified within a single grain. However, since twinning was also commonly observed in the as-heat treated condition, it is not possible to determine whether these twins were created during the thermal treatment or were created as a direct result of the compression at room temperature. Finally, it should be noted that ordinary dislocations are frequently active in grains in which twinning is also active. In contrast, twinning is usually not accompanied by glide of superdislocations.

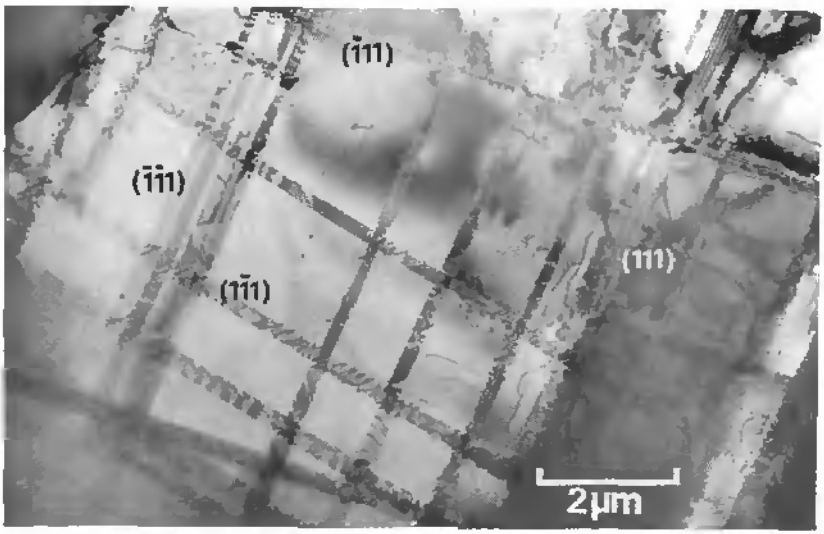

Figure 4.11 : Activation of the four possible 1/6<112]{111} twinning systems within the same grain.

4.1.3 Ordinary Dislocations

1/2<110] ordinary dislocations have been observed in every grain and play an important role in the deformation of this structure. Usually at least one system is active homogeneously throughout the grain as shown in all four of the grains identified in detail in Section 4.1.1. Additional slip of ordinary dislocation systems are also frequently seen to be active locally or inhomogeneously within a grain. An example of the local activation of ordinary dislocations near a twin / twin intersection was

shown in Figure 4.6(c). They are also commonly observed associated with α_2 particles. When observed to be associated with the particles, these are often found to lie on the (001) cube plane which would indicate that they were formed during the thermal heat treatment.

Although groups of dislocations associated with the particles or random individual dislocations were identified on the (001) plane, the vast majority of dislocations were shown to be glissile on the {111} octahedral planes as expected. Most of the ordinary dislocations were found to tend to be in screw or near screw orientation. Of the 20 systems analyzed in detail, 18 showed a definite preference for the screw orientation. Although the dislocations were most often screw, it was possible to define the slip planes by trace analysis of segments of the dislocations (usually at the foil surface) which were not exactly in screw orientation. The dominance of dislocations in the screw orientation is emphasized by the distribution of 1/2{110] dislocations shown in Figure 4.12(a). Since the foil normal is approximately parallel to [110], these screw dislocations are almost completely contained in the plane of the foil. Hence, the long screw segments of the dislocations are clearly visible. However, these

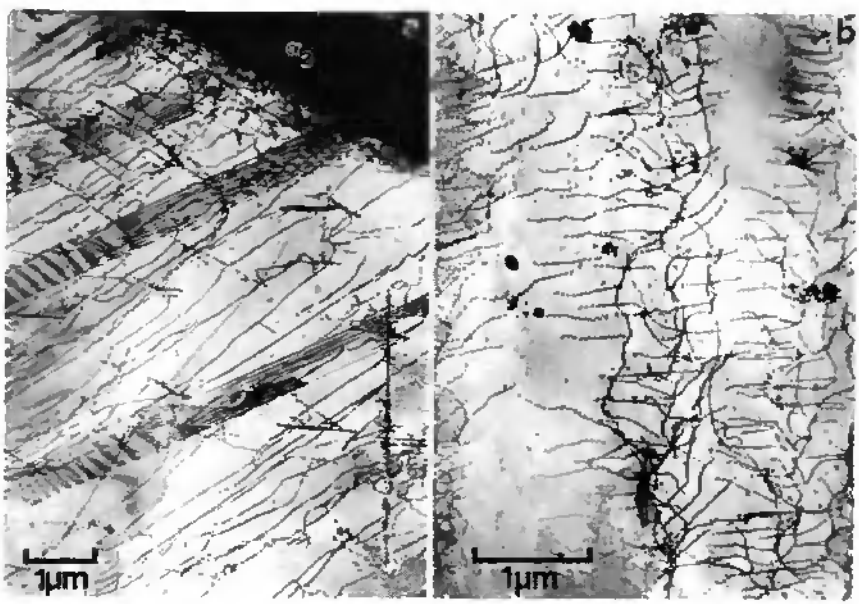

Figure 4.12 : Typical examples of 1/2<110} screw dislocations in the equiaxed microstructure (a) grain 6E and (b) grain 5F (from Table 4.5).

dislocations are only nominally in the screw orientation and frequent cusps or local changes in the line direction occur. Apart from the screw orientation, dislocations or dislocation segments are

occasionally found in orientations 30° from screw orientation (u=<211]) and, rather infrequently, 60° from screw (u=<011]). Edge dislocations were virtually never encountered. The ordinary dislocations also exhibit a tendency to form long, approximately planar pile-ups as shown in Fig 4.12(b). Again, these dislocations tend to align in the screw orientation. Due to the gentle curvature of the dislocations in both of these micrographs, it can be concluded that these dislocations are mobile.

4.1.4 Superdislocations and Faulted Dipoles

In the previous sections, superdislocations have been shown to be activated only in localized areas (Figures 4.3 & 4.4). However, under the loading conditions which result in a sufficiently large Schmid factor, superdislocations can be active throughout an entire grain. In this section, three types of deformation structures will be presented and identified in detail: <101] superdislocations, 1/2<112] superdislocations and faulted dipoles. It must be noted that, in contrast to the widespread activation of twinning and ordinary dislocations, these mechanisms are found only in limited grains.

An example of a grain containing many superdislocations is shown in Fig 4.13(a), where twinning, dislocations and numerous stacking faults can be seen to the right of an elongated α_2 particle. All the visible dislocations in Fig 4.13(a) are of the superdislocation type and the twin plane was identified as $(1\bar{1}1)$. A higher magnification view of the central region of the micrograph indicated by the arrow is shown in Fig 4.13(b) where the nature of the faulted dipoles becomes clearer. The Burgers vector of the dislocations associated with the dipoles was determined to be $1/2[\bar{1}12]$ from appropriate contrast experiments and the dislocation and stacking fault are coplanar on the $(1\bar{1}1)$ plane. The elongated direction of the stacking fault was found to be $[\bar{1}01]$. Isolated stacking faults on the $(1\bar{1}1)$ plane are also seen throughout the grain. A more complete identification of these dipoles will be given below.

At the left of the particle, the deformation structure is considerably different. No more twinning is seen and only superdislocations of the type <101] have been identified. Several dislocation pile-ups are seen on this side of the particle as indicated by the arrow in Fig 4.13(a) and a representative pile-up of these dislocations is shown in more detail in Figure 4.14(a). Since these dislocations are visible with 002g, they must be of a superdislocation type. Furthermore, as shown in Fig 4.14(b), this pile-up apparently consists of dislocations with two different Burgers vectors. Two dislocations in this pile-up, indicated by the 1 and 2 in Figs 4.14(a)&(b) were selected for the detailed contrast analysis given in Figs 4.14(c) to (l). A summary of these contrast experiments is also given in Table 4.4.

It can be straightforwardly noted from Table 4.4 that the observed contrast matches the Burgers vectors $[\bar{1}01]$ and $[0\bar{1}1]$ for dislocations 1 and 2, respectively. Furthermore, detailed observation of the dislocation dissociation and glide plane reveals additional information. The line direction of dislocation 1 was determined to be $[\bar{1}01]$, thus indicating that the dislocation is in the screw

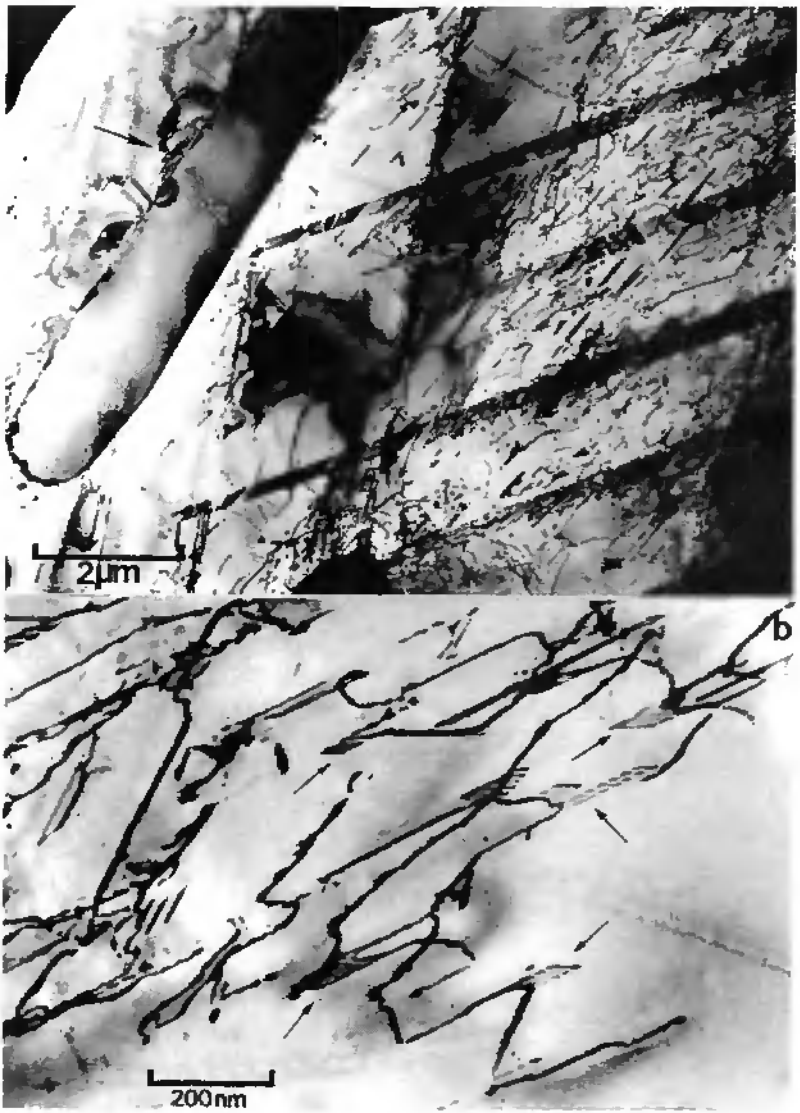

Figure 4.13 : (a) A typical grain (e.g. 6B) containing many superdislocations and (b) an enlarged view which shows the nature of the faulted dipoles which are abundant in this grain.

diffracting conditions	1 Observed	g·[$\bar{1}$01]	2 Observed	g·[0$\bar{1}$1]
($\bar{1}\bar{1}$0) 002g	visible	2	visible, dissociated	2
($\bar{1}\bar{1}$0) 1$\bar{1}$1g	invisible	0	visible, dissociated	-2
($\bar{1}\bar{1}$0) $\bar{1}$11g	visible	2	invisible	0
($\bar{1}\bar{2}$1) $\bar{1}$11g	visible, dissociated	2	-----	--
($\bar{1}$00) 00$\bar{2}$g	visible, dissociated	-2	visible, dissociated	-2
(0$\bar{1}$1) $\bar{2}$00g	visible	2	invisible	0
(0$\bar{1}$1) 1$\bar{1}$1g	invisible	0	invisible	0

Table 4.4 : Summary of the contrast experiments for dislocations 1 and 2. The observed contrast is given for both dislocations along with any evidence of dissociation and the value of g·b for the proposed Burgers vectors.

orientation. Trace analysis of the direction containing the ends of the dislocations in the pile-up (assuming that the dislocations are glissile on the same plane) determined the glide plane to be (111). It should be noted that this is also the plane with the higher Schmid factor, m = 0.35, versus m = 0.23 for the glide plane (1$\bar{1}$1). However, dissociation of the dislocation is observed on the a plane other than (111). This is observed by comparing, for example Figs 4.14(j) with (k). For the same diffracting vector 002, the dislocation is seen to be dissociated for the beam direction ($\bar{1}$00), while only a single image is observed for the ($\bar{1}\bar{1}$0) beam direction. Similarly, no dissociation is seen for the 1$\bar{1}$1g in the ($\bar{1}\bar{1}$0) beam direction Fig 4.14(i), while a dissociation is again observed for B=($\bar{1}\bar{2}$1) - Fig 4.14(g). This indicates that the dislocation must be dissociated on the (1$\bar{1}$1) plane since the dissociation is not visible when the beam direction is contained within this plane. Thus, the observed plane of dissociation is different than the glide plane during deformation. It cannot be determined whether this dissociation configuration occurred during the actual deformation process or was created during any relaxation processes associated with unloading, foil preparation and foil observation. The observation of two partial dislocations and no stacking fault fringes between the partials indicates that the superdislocation is dissociated according to :

$$[\bar{1}01] \Rightarrow 1/2[\bar{1}01] + \text{APB} + 1/2[\bar{1}01] \qquad 4.2.)$$

In regard to dislocation 2 with b_2=[0$\bar{1}$1], the line direction was found to be near [$\bar{1}\bar{1}$2] and, thus, the glide plane is uniquely defined as (111). The observation that both dislocations 1 and 2 appear to be piled-up on the same glide plane, Fig 4.14(a), plus the unique glide plane of dislocation 2 further verifies the conclusion from above that the glide plane of dislocation 1 was also (111). Dislocation 2 is also trailed by a small stacking fault. Analysis of the edges of the fault indicates that they lie along the directions [101] and [0$\bar{1}$1], respectively. Thus, the arrangement of partial dislocations and stacking fault is coplanar on the (111) plane. It should be noted that the dislocation to the right of b_2 is a 1/2[110] ordinary dislocation.

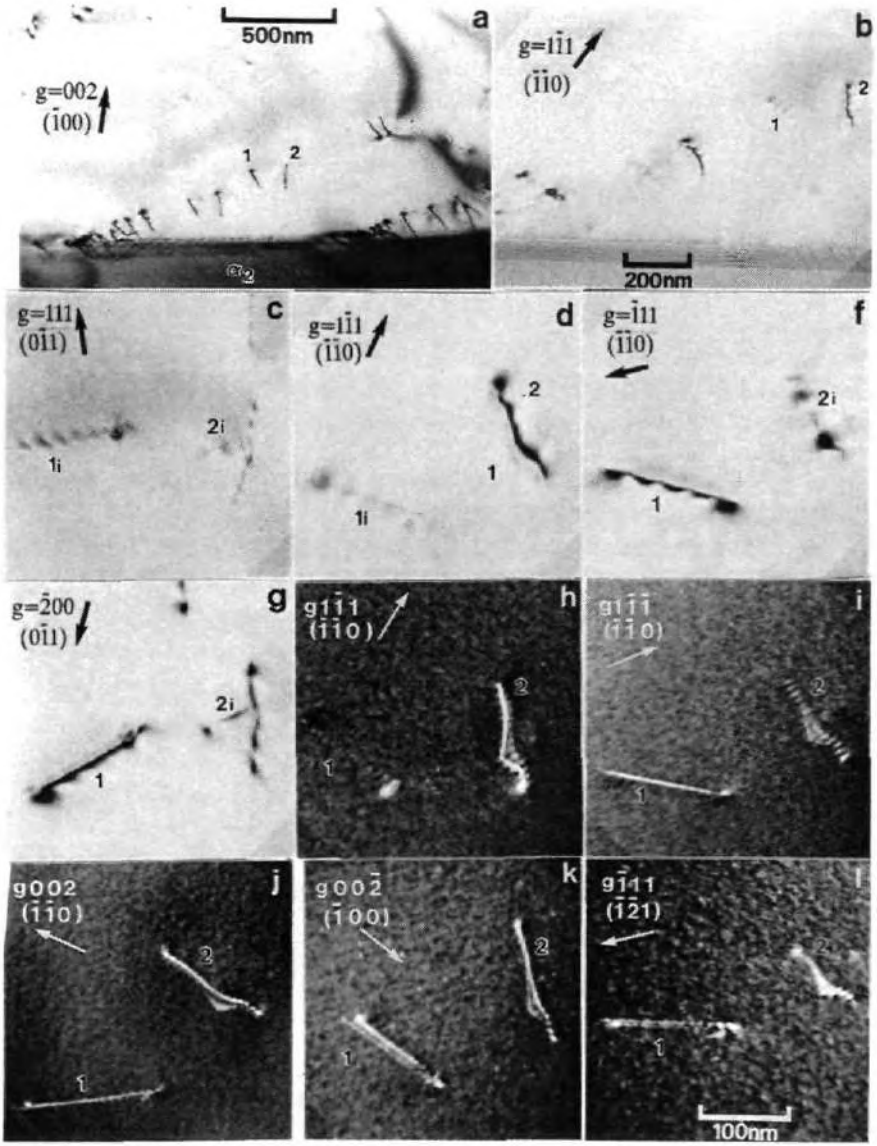

Figure 4.14 : (a) A pile-up of superdislocations at the α_2 particle shown in Fig 4.13 and (b) shows that two types of dislocations are present in this pile-up. (c) - (l) detailed contrast analysis used to identify the two slip systems which are summarized in Table 4.4.

Additionally, superdislocations may be involved in reactions or decompositions with ordinary dislocations. An example of this is shown in Figure 4.15 where a long, irregular dislocation labelled 2 is seen to be associated with multiple stacking faults which vary in width from 5-50nm. Since this dislocation is visible with 111g, 11$\bar{1}$g and 020g, its Burgers vector must be parallel to either [1$\bar{1}$2] or [$\bar{1}$12]. The Burgers vector is uniquely determined to be parallel to [1$\bar{1}$2] by its visibility with the $\bar{1}$31g (Fig 4.15(f)) and is assumed to be 1/2[1$\bar{1}$2]. Both the dislocation 2 and the stacking fault are found to be on the ($\bar{1}$11) plane by trace analysis. Contrast analysis tentatively identifies the partial dislocation surrounding the stacking fault as 1/6[1$\bar{1}$2]; however, a complete analysis of the partials surrounding the dipoles is deferred until Section 4.2.3. One segment of dislocation 2 is seen to exhibit different contrast behavior and has, thus, been indicated by 1. Since this dislocation is invisible for 020g and 11$\bar{1}$g, its Burgers vector is defined by [101]. Finally, the segments labelled 3 are 1/2[110] dislocations as verified by the invisibility for 002g and visibility for 111g and these segments are also on the ($\bar{1}$11) plane. From the identification of the Burgers vectors and the form of the dislocations, it is postulated that the following decomposition is responsible for the observed arrangement :

$$[101] \quad \Rightarrow \quad 1/2[1\bar{1}2] + 1/2[110] \qquad 4.3.)$$

followed by the reaction :

$$1/2[1\bar{1}2] \quad \Rightarrow \quad 1/6[1\bar{1}2] + SF + 1/3[1\bar{1}2] \qquad 4.4.)$$

A schematic diagram with a summary of the Burgers vectors and line directions of the full arrangement is given in Fig 4.15(g). It is necessary to note that all faulted dipole arrangements identified are associated with 1/2<112] type dislocations and that the elongated line direction of the fault is always a <101] type direction.

The propensity of the 1/2<112] superdislocations to form faulted dipoles depends upon the individual grain orientation. For instance, the right side of the grain in Figure 4.13 was shown to be dominated by stacking faults and faulted dipoles. In contrast, a grain is shown in Figure 4.16 where a large number of superdislocations are present, but only a negligible fraction of these form faulted dipoles. All the dislocations visible in Fig 4.16(a) with the 002g must be of the superdislocation type. These superdislocations have been identified to be [011] screw dislocations. However, as shown in Fig 4.16(b), there is little tendency for these superdislocations to form faulted dipoles. Only five faulted dipoles and four isolated stacking faults have been identified in this area. This is very low in comparison to the density shown in Figure 4.13.

In summary, the most important points from this section are:

1.) superdislocations can be active throughout a grain, though they are less common than ordinary dislocations and twinning.

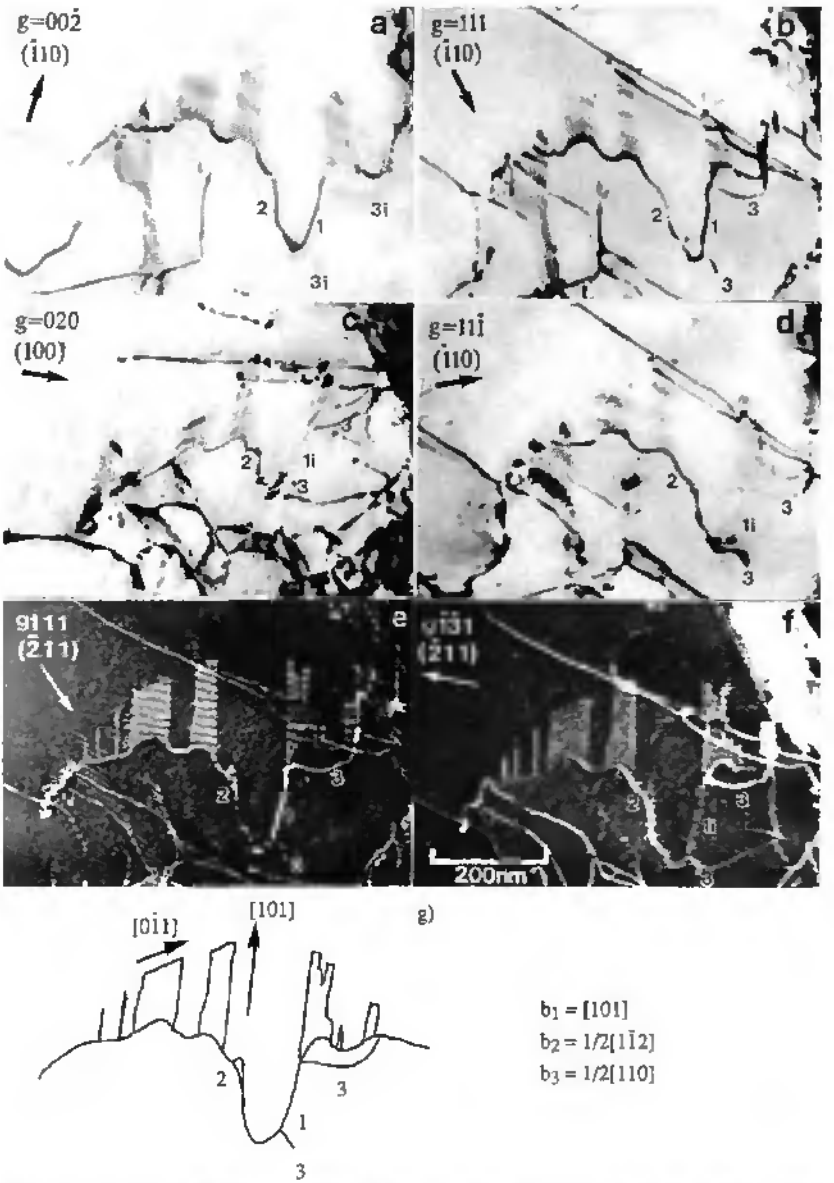

Figure 4.15 : Detailed contrast experiments which reveal the structure of the faulted dipole. Note the decomposition of the [101] superdislocation into two full dislocations of 1/2[1$\bar{1}$2] and 1/2[110]. A schematic diagram of this arrangement is shown in (g).

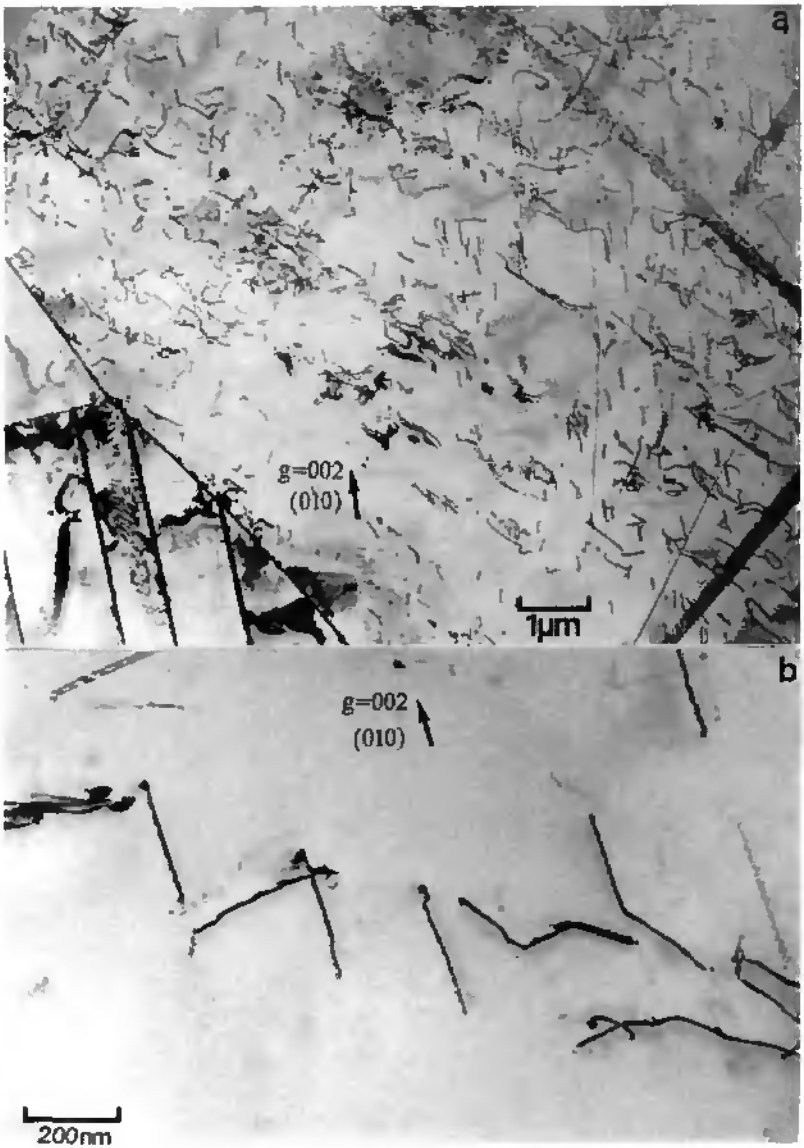

Figure 4.16 : An example of a grain (8F) which deforms extensively by glide of superdislocations (a), but shows little tendency for these superdislocations to form faulted dipole arrangements (b).

2.) <101] superdislocations are usually straight, screw segments, they can be dissociated on {111} planes and they may decompose into 1/2<112] and 1/2<110] dislocations.
3.) 1/2<112] dislocations are observed to be irregular in shape and can decompose to form elongated faulted dipole arrangements.
4.) the tendency of the superdislocations to form faulted dipoles varies from grain to grain.

4.1.5 Summary

At this point it is appropriate to summarize all of the deformation structures which have been observed in the equiaxed microstructure. The distinction has been clearly pointed out between the deformation mechanisms which are globally active within a grain and those which are only present locally. In this section, only the deformation mechanisms which were active homogeneously throughout the grains will be considered.

Table 4.5 lists the Schmid factor for the deformation mechanisms which were observed in each grain. Also listed in the table is the plane of stacking faults / faulted dipoles when they were observed throughout a grain, the total number of systems active in the grain and the approximate grain size. The identification code for the grain is only an internal system, however, it can be noted that the grains 5A, 5B, 5E and 5F correspond to the grains A, B, E and F presented in Section 4.1.1. When two Schmid factors have been listed (for example, in the case of the ordinary dislocations), this indicates either that the dislocations are only found in the screw orientation and a unique slip plane cannot be defined or that segments on both possible slip planes have been identified. In the case where deformation twins and 1/2<112] superdislocations were found on the same plane, these were taken as two separate mechanisms of deformation.

The relative importance of the different deformation modes is readily seen from the table. Of the 15 grains which were examined, all but one contained at least one ordinary dislocation system. For this one exception (i.e. 6A), four twinning systems were activated and $m < 0.12$ for all ordinary dislocations. Hence, it can be stated that the ordinary dislocations are generally activated for $m > 0.25$. Only in one case was $m > 0.25$ and the ordinary dislocations were not active. Likewise, deformation twinning is favorable for values of $m > 0.30$. Of the twinning systems observed, 18 were active for $m > 0.30$, while 5 were active for values less than this. However, since significant deformation twinning was observed in the as-heat treated condition, it can not be determined with certainty whether these other 5 twinning systems were created during the room temperature compression or the heat treatment process. Also, it must be noted that there are grains where $m > 0.30$ for a twinning system yet it was not activated. Also, 1/2<112] dislocations are sometimes observed instead of twinning. These topics will be addressed in more detail in the discussion. Finally, it should be observed that the superdislocations were only observed for $m > 0.35$ with the exception of grain 6B where 1/2<112] dislocations were observed for $m = 0.12$. It should also be noted that 6B

observed	5A	5B	5E	5F	6A	6B	6C	6E	6F	8A	8B	8E	8F	7E	7D
ordinary 1/2<110] dislocations	.32	.48 .47	.22	.47/.22 .49/.19	-	.26/.24	.32 .31	.12/.11 .12	.34 .27	.39/.09	.49/.10 .44/.16	.32	.42/.34 .46	.29/.08	(1)
twinning systems	.34 .29	-	.47 .46	-	.38 .45 .47 .50	.12	.38 .36	*.47* *.01*	.35 .35	.32 .28 .14	.07	.39 .37	-	.39	*.02*
<101) superdislocations	-	(.34) local	-	local	-	.35 .34	-	.41 (.35)	-	-	-	-	.45	-	(1)
1/2<112] superdislocations	-	-	-	-	-	.12	-	.47 .41	-	-	-	-	.34	-	-
faulted dipoles	-	-	-	-	-	(1$\bar{1}$1)	-	-	-	-	-	-	-	-	-
total systems	3	2(3)	3	2(3)	4	4	4	7	4	4	3	3	4	2	3
ϕ, μm	>15	>15	12	>15	>15	25	15	7	5	>15	8	>10	>20	-	>10

Table 4.5 : Summary of the Schmid factors, m, for slip systems that have been observed in each equiaxed grain. Also given is the plane of any stacking faults or faulted dipoles that were observed, the total number of deformation systems active in the grain and the approximate grain diameter, ϕ. If specific system wasn't identified in detail, the number of systems of this type are then given in parentheses. For screw dislocations where a unique slip plane cannot be defined, the Schmid factor for both slip systems is given. If the Schmid factor for twinning is in *italics*, this designates twinning that would result in single crystal extension.

was unusual in that it was the only grain where the faulted dipoles were a common occurrence. As pointed out previously, for grains where twinning was observed, there exists at least one <101] superdislocation system where m > 0.40. Despite this large Schmid factor, the superdislocations are not active; therefore, it is clear that twinning is more favorable than glide of superdislocations and that superdislocations will only become active in grains where the twinning process is unfavorable.

Finally, the orientation of the investigated grains is summarized in Figure 4.17(a) and the active deformation mechanisms have been correlated with the axis of the applied compressive loading as shown in Fig 4.17(b). A full [001] stereographic projection has been used in place of a standard triangle in order to preserve the consistent indexing method. However, in the current analysis, the grains are considered as separate entities that deform independently of one another. In contrast, the consistent indexing will be exploited in Section 4.3 in order to examine the influence of the orientation relationships on the active deformation mechanisms.

It is worthwhile to note some of the general features of the influence of loading orientation on the deformation mechanisms. Firstly, twinning appears to be prevalent for loading orientations nearly parallel to [001], while superdislocations are only observed for loading orientations at the "perimeter" of the projection or nearly parallel to the (001) plane. As stated earlier, ordinary dislocations are seen for all loading orientations. Finally, extensive faulted dipole and stacking fault arrangements are seen only in the grain which is loaded nearly parallel to a <111> direction. These observations will be compared to the lamellar structure and treated in detail in the discussion. (Note : a schematic summary of these observations is presented in Fig 4.26(c) in order to aid the reader in visualizing the loading orientations where the various deformation mechanisms have been observed.)

a.)

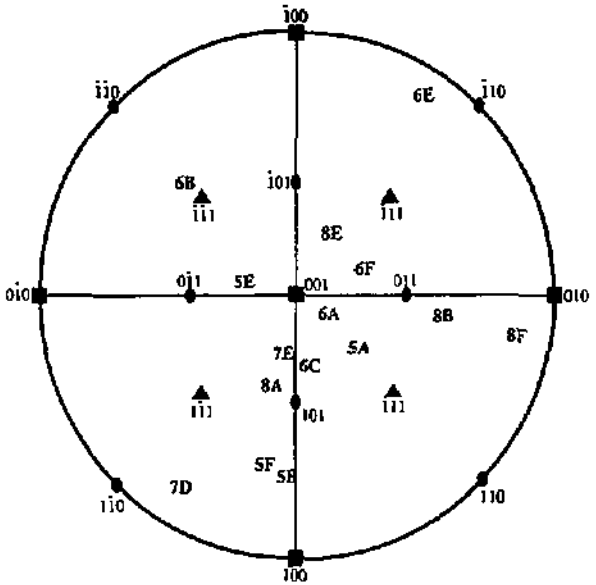

b.)

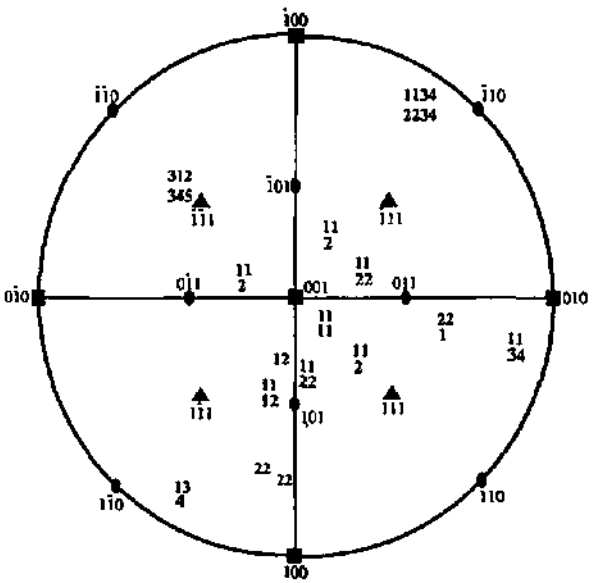

Figure 4.17 : Summary of the influence of (a) loading orientation on (b) the deformation mechanisms in the equiaxed structure 1) twinning, 2) 1/2<110], 3) <101], 4) 1/2<112] and 5) faulted dipoles.

4.2) Transformed Lamellar Structure

In this section, the deformation mechanisms of the transformed lamellar structure (1270°C, 64h) will be presented. In the first part, the deformation characteristics of the coarse lamellar grains will be described by presenting the analysis of a collection of four lamellae in detail in order to emphasize the general characteristics of this structure. A general rule used in the section to differentiate "coarse" from "fine" lamellae has been defined at approximately 1μm and the choice of this value will become apparent in Section 4.2.2. Next, some further details will be given concerning the formation of the faulted dipoles and the twinning. Subsequently, the differences between the deformation of the coarse and fine lamellae will be presented along with some further details of the mechanisms in the fine lamellae. This analysis will then be concluded with a summary of all results on the lamellar structure and these results will again be related to the loading orientation. Attention will also be given in this summary to the so-called "hard" and "easy" modes of deformation [1].

Furthermore, since the α_2 phase may play an important role during the deformation of this structure, a final section will be included to present some of the observations of deformation in the α_2 lamellae. Although no deformation structures were observed in the α_2 lamellae in the heat-treated and deformed material, observations were carried out on the as-cast and deformed material.

4.2.1 General Characteristics

In order to introduce the general characteristics of deformation, an overview of four coarse lamellae is shown in Figure 4.18. Two types of interfacial boundaries exist between these four grains. Firstly, the interface between lamellae A/B and E/F is a flat, regular interface characterized and the rotation between these grains is described as a 180° rotation about a {111} plane. It should be noted that the vast majority of interfaces between the adjacent γ lamellae are of this 180° type. The second type of boundary is that between the lamellae A/E and B/F which separates a single lamella into two differently ordered regions. These interfaces are irregular in nature and cannot be described by a low index plane. However, it should be noted that these ordered domains within a single lamella can only be described as a 90° rotation about a cube axis (or equivalently, 120° rotation about a <111>). For the current example, both relationships between lamellae A/E and B/F have been described by a 90° rotation about [010]. The SADPs used to determine these orientation relationships plus the zone axes corresponding with each SADP plus the orientation relationships between the lamellae are shown in Figure 4.19(a). Schematic diagrams of the zone axes at the tilt positions 1, 2 and 3 are presented in Fig 4.19(b) in order to facilitate visualisation of the rotations between the grains.

Figure 4.18 : Typical deformation characteristics of the coarse lamellar structure.

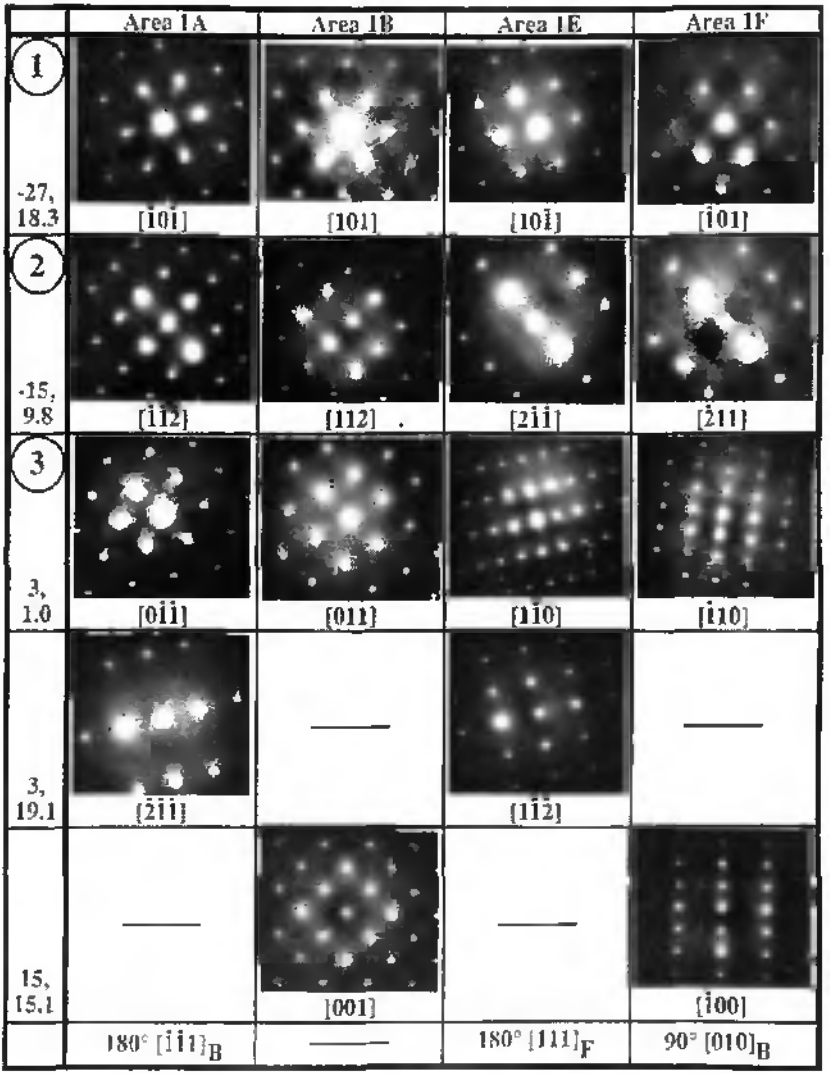

Figure 4.19(a) : Selected area diffraction patterns (SADP) corresponding to the four lamellae A, B, E and F shown in Figure 4.18 obtained after tilting to the values of the angles (goniometer reading) shown on the left of the figure such that specific orientations were reached. From this series of SADPs, the specific rotations of each lamella relative to the others have been defined.

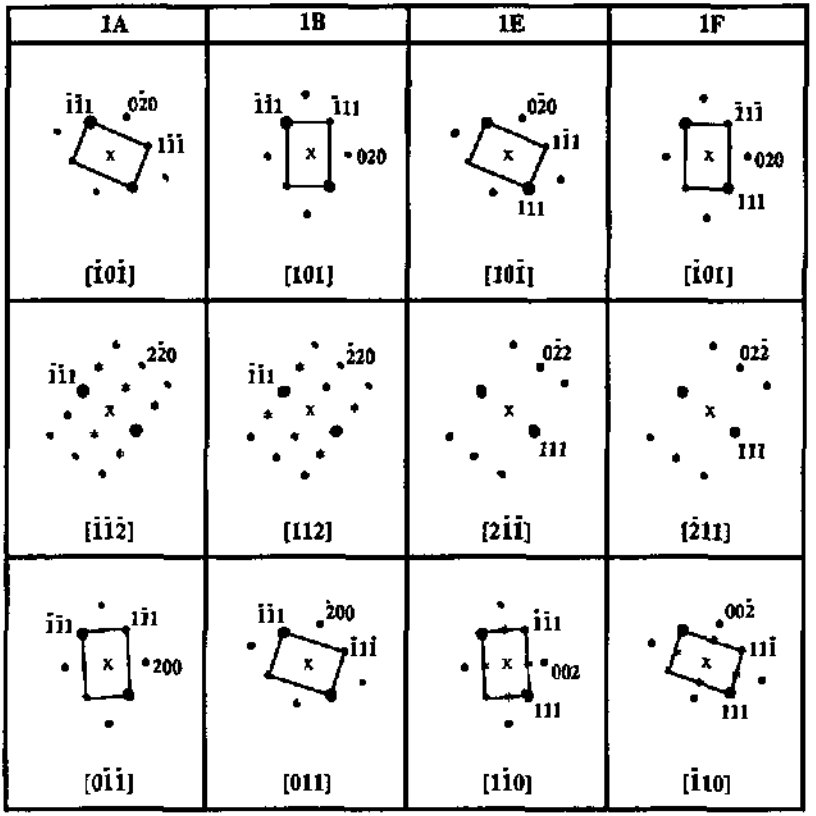

Figure 4.19(b) : Schematic diagram of the SADPs corresponding with the orientations 1, 2 and 3 in Fig 4.19(a) with selected reflections identified. The large spots indicate the plane of rotation common to all the zones. Solid spots are fundamental reflections while the starred spots indicate the position of superlattice spots.

It is readily seen in Figure 4.18 that the deformation mechanisms tend to vary from lamella to lamella, but that they are homogeneously distributed within any given lamella. In each coarse lamella, at least two deformation mechanisms are active and this is more clearly demonstrated in Figure 4.20. In Figs 4.20(a)&(b), the deformation mechanisms of lamella A are shown to be deformation twinning on the ($\bar{1}$11) plane, few 1/2[110] ordinary dislocations (indicated by the 2), few 1/2[1$\bar{1}$2] dislocations (dislocations labelled 1) and some isolated stacking faults on ($\bar{1}$11), marked with the number 3. Also seen are several 1/2[1$\bar{1}$2] dislocations which have transformed to yield faulted dipoles. Fig 4.20(b) shows that all deformation structures are invisible with the $\bar{1}$11g which confirms that the Burgers vectors of all dislocations are contained within this plane. It is also interesting to note that both

1/6[1$\bar{1}$2] twinning and 1/2[1$\bar{1}$2] superdislocations are identified in this lamella. The deformation structure in lamella B is straightforward and consists of deformation twinning on the (111) and ($\bar{1}$11) planes and a low density of 1/2[110] ordinary dislocations - see Fig 4.20(c).

The deformation structure in lamella E consists of many stacking faults and dipole arrangements, Fig 4.20(d), and it can also be seen that a significant density of superdislocations is also present, Fig 4.20(f) with 002g. These faulted dipoles are associated with 1/2[$\bar{1}$$\bar{1}$2] dislocations (labelled with 1) and the other isolated faults also lie on the (111) plane. Several of the superdislocations have been identified as [10$\bar{1}$] (identified with 2) on the (1$\bar{1}$1) plane. Finally, Fig 4.20(e) demonstrates that a low density of 1/2[$\bar{1}$10] screw dislocations (designated by 3) is also present in the lamella. Finally, lamella F contains a high density of dislocations and these have been identified as both ordinary 1/2[110] dislocations (labelled with a 3) and [101] (labelled 2) or 1/2[1$\bar{1}$2] (labelled 1) superdislocations as indicated in the Figs 4.20(g)&(h). The nature of the superdislocations is confirmed by the visibility with 002g as shown in Fig 4.20(h).

A summary of these active mechanisms is given in the schematic diagram shown in Figure 4.21 along with the Schmid factor for these systems. Similar to the equiaxed microstructure, the active systems generally correspond to those with the highest Schmid factors. Again, it is also clear that twinning is generally more favorable than the glide of superdislocations in grains. One notable exception to the observation that the active systems correspond to the systems with the largest resolved shear stress is the low Schmid factor for the dislocations associated with the faulted dipoles in E (m = 0.07). A low factor for the dislocations associated with the faulted dipoles is frequently observed in this microstructure. It should also be noted that the tendency of the 1/2<112] superdislocations to form dipoles tends to vary between grains (for example, lamella F vs. A and E).

4.2.2 Fine Lamellar Zones

The deformation structure in the fine lamellae adjacent to lamella A is shown in Figure 4.22. This structure consists of alternating, fine lamellae of γ and α_2 as previously shown, with only occasional examples of adjacent γ lamellae. Although stress concentrations are observed in the α_2 lamellae, individual deformation structures are infrequently identified. Thus, a larger proportion of the total deformation occurs in the γ lamellae and the propagation of deformation from γ to γ lamellae is impeded by the α_2 lamella between the two. However, for sufficiently thin α_2 the deformation does appear to be transmitted from one side to the other as indicated by the arrow to the right of the figure. The orientation of most of the γ lamellae here is the same as that of lamella B (Fig 4.18) and it can be seen that these all deform predominantly by deformation twinning on the ($\bar{1}$11) plane. Few dislocations are visible in the other γ lamellae. Hence, it it is shown that this lamellar colony tends to deform as a unit such that the lamellae with similar orientation deform by the same deformation mechanisms. The influence of lamellar thickness is also clearly seen by comparison of

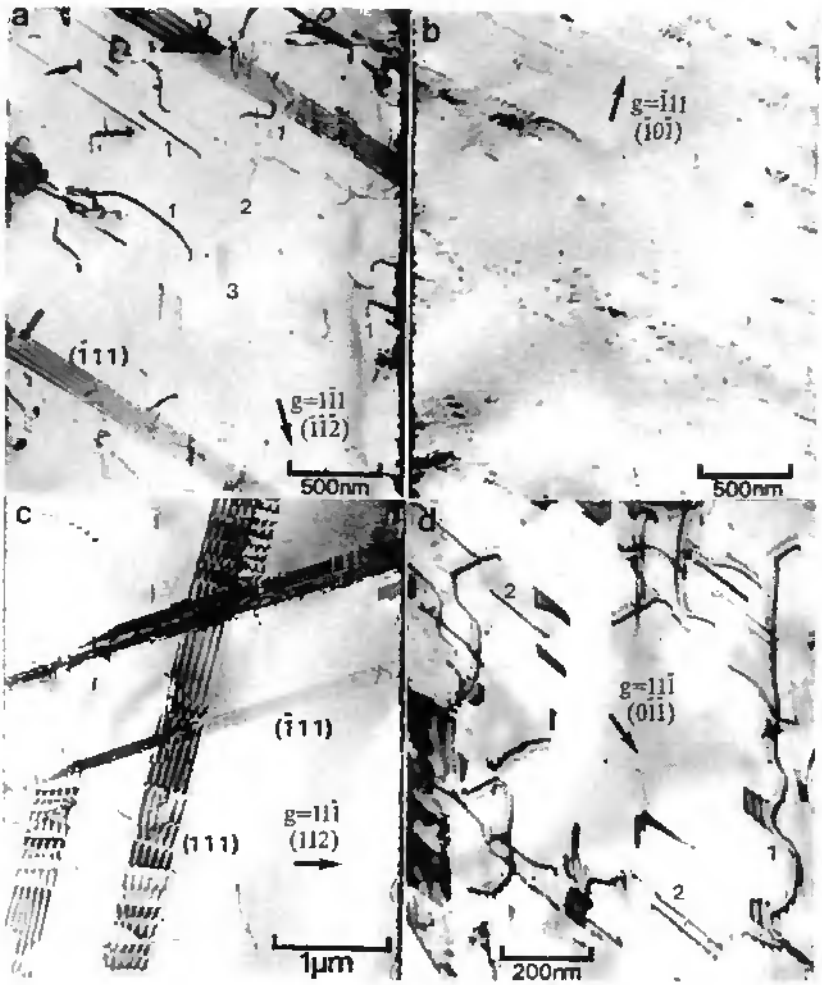

Figure 4.20 : Higher magnification micrographs of the deformation structures identified in the lamellae shown in Fig 4.18 (a) - (b) lamella A, (c) lamellae B and (d) lamellae E.

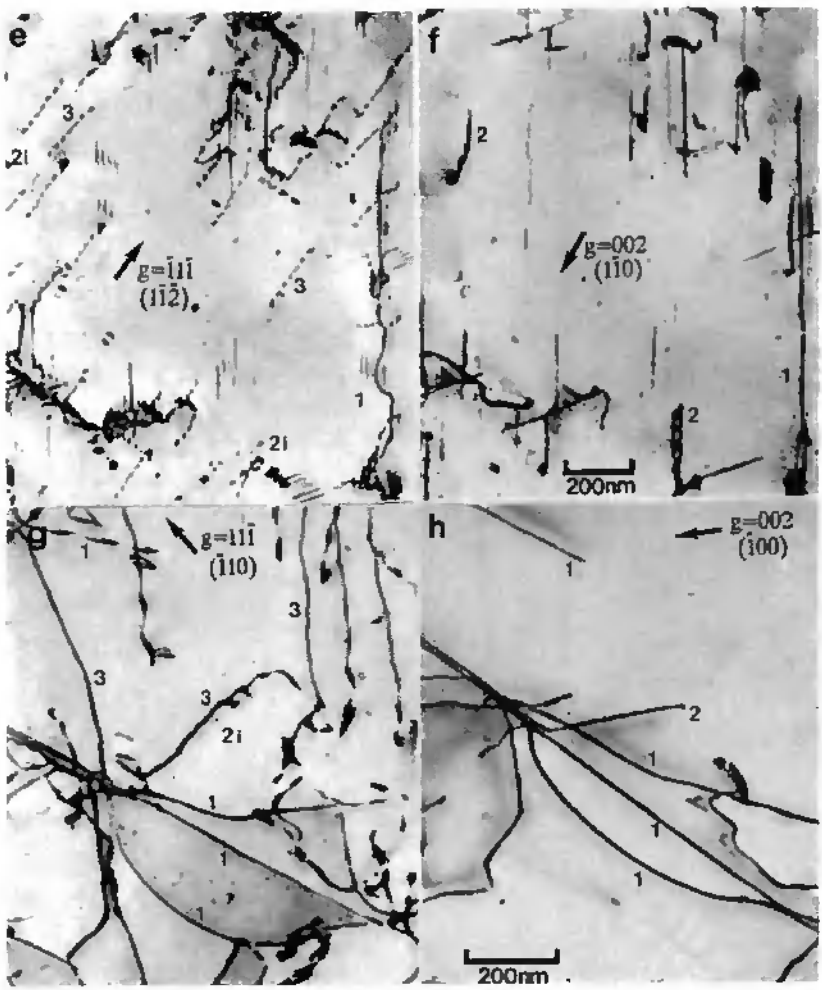

Figure 4.20 cont : Higher magnification micrographs of the deformation structures identified in the lamellae shown in Fig 4.18 (e) - (f) lamella E and (g) - (h) lamellae F.

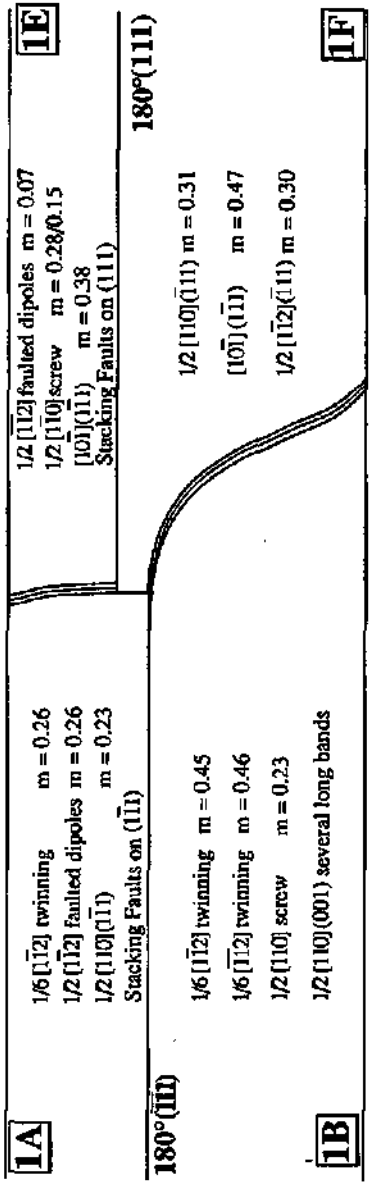

Figure 4.21 : Schematic representation of the lamellae in Fig 4.18 and a summary of the observed deformation mechanisms in each grain. Also given are the Schmid factors for each mechanism.

Figs 4.18 & 4.22. While lamella B deformed by two modes of twinning and one system of ordinary dislocations, the similarly oriented fine lamellae deform by only a single mode of twinning. It is a general observation that the fine lamellae tend to deform primarily by only a single mechanism and this is clearly shown by the observations summarized in Table 4.8 (Section 4.2.5) where the total number of deformation systems is given in relationship to the lamellar thickness.

Figure 4.22 : Deformation in the fine lamellar regions which is concentrated in the γ phase. Note that for the lamellae with the same orientation as B (Fig 4.18) only one twinning system is active.

4.2.3 Faulted Dipoles

In order to investigate the grain to grain variation in the tendency to form faulted dipoles, three further lamellae are presented in Figure 4.23. In Fig 4.23(a), dense faulting dominates the deformation structure and rather few dislocations are seen. Several of these dislocations have been identified as [101] and trace analysis has been used to determine that the preferred orientation is screw. Some segments have, however, been found to be on the $(\bar{1}11)$ plane with m = 0.24, which is in contradiction with the higher Schmid factor, m = 0.33, for the $(\bar{1}\bar{1}1)$ glide plane. It is readily shown that the stacking faults also lie on the $(\bar{1}11)$ plane as shown in Fig 4.23(b) where all the faults are viewed edge-on for the beam parallel to [211]. This grain also contained a low density of $1/2[110]$ $(\bar{1}11)$ dislocations which are not shown in the photos.

Similarly, the lamella shown in Figs 4.23(c)&(d) also contained a high density of stacking faults which are verified to be on the (111) plane. Although the lamella contained numerous isolated stacking faults (i.e. presumed to be faulted dipoles for which the associated superdislocation is not contained within the thin foil section), faulted dipoles were also observed to be associated with 1/2[$\bar{1}\bar{1}$2] dislocations (labelled 2) for which the Schmid factor m = 0.18. Fewer [10$\bar{1}$] (111) dislocations, labelled 1, (m = 0.34) were also observed in the grain as were a low density of 1/2[1$\bar{1}$0](111) ordinary dislocations (m = 0.37). The invisibility of most of the deformation structures with the 111g confirms that the Burgers vectors of most dislocations in this grain are contained in the (111) plane.

Finally, an example is shown in Figs 4.23 (e)&(f) where superdislocations are active (visible with the 002g in Fig 4.23e) which show little tendency to form faulted dipoles. These dislocations have been identified to be of the type b_2 = [011] (m = 0.49) and b_3 = 1/2[$\bar{1}$$\bar{1}$2] (m = 0.30). Also active in this lamella is a low density of dislocations b_1 = 1/2[1$\bar{1}$0] as shown in Fig 4.23(f).

One important difference between the lamellae which formed the faulted dipole arrangements and those which did not is the proximity of the loading orientation to a <111> direction. For instance, the three lamellae which have been shown to contain a high density of faulted dipoles (lamella E in Figure 4.20(d) and the two lamellae containing faults in Figs 4.23 (a)&(c)), are 11°, 12° and 8°, respectively, from a <111> direction. In contrast, for the two lamellae shown which contain many superdislocations without any stacking faults (grain F in Fig 4.20(h) and Fig 4.23 (e)) are 33° and 30° from a <111> loading direction. It should be noted that this propensity to form dipoles near <111> loading directions was also observed in the equiaxed microstructure. Thus, there appear to be two necessary conditions for the formation of the faulted dipoles and stacking faults to dominate the deformation structure:

1.) activation of 1/2<112] and / or <101] superdislocations

2.) and a loading orientation nearly parallel to a <111> direction.

Returning to the faulted dipoles presented in lamella A (Figure 4.20), detailed contrast experiments have been performed in order to identify the dislocation associated with the fault and the partial dislocations surrounding the fault. The results of this analysis are reproduced in Figure 4.24 and summarized in Table 4.6. Since the main dislocation is invisible for $\bar{1}$11g Fig 4.24(d), the possible Burgers vectors would be [101], [01$\bar{1}$] and 1/2[1$\bar{1}$2]. The dislocation is visible with both the 200g and 020g such that the Burgers vector must then be 1/2[1$\bar{1}$2]. Similarly, since the fault is shown by trace analysis to be on the ($\bar{1}$11) plane, then the possible Shockley partials surrounding the fault would be 1/6[1$\bar{1}$2], 1/6[$\bar{1}$12] or 1/6[211]. The invisibility of the partials for the 0$\bar{2}$2g and $\bar{1}$$\bar{1}$1g, plus the ±2/3 contrast asymmetry for the 1$\bar{1}$1g confirms that the direction of the Burgers vector of the partial

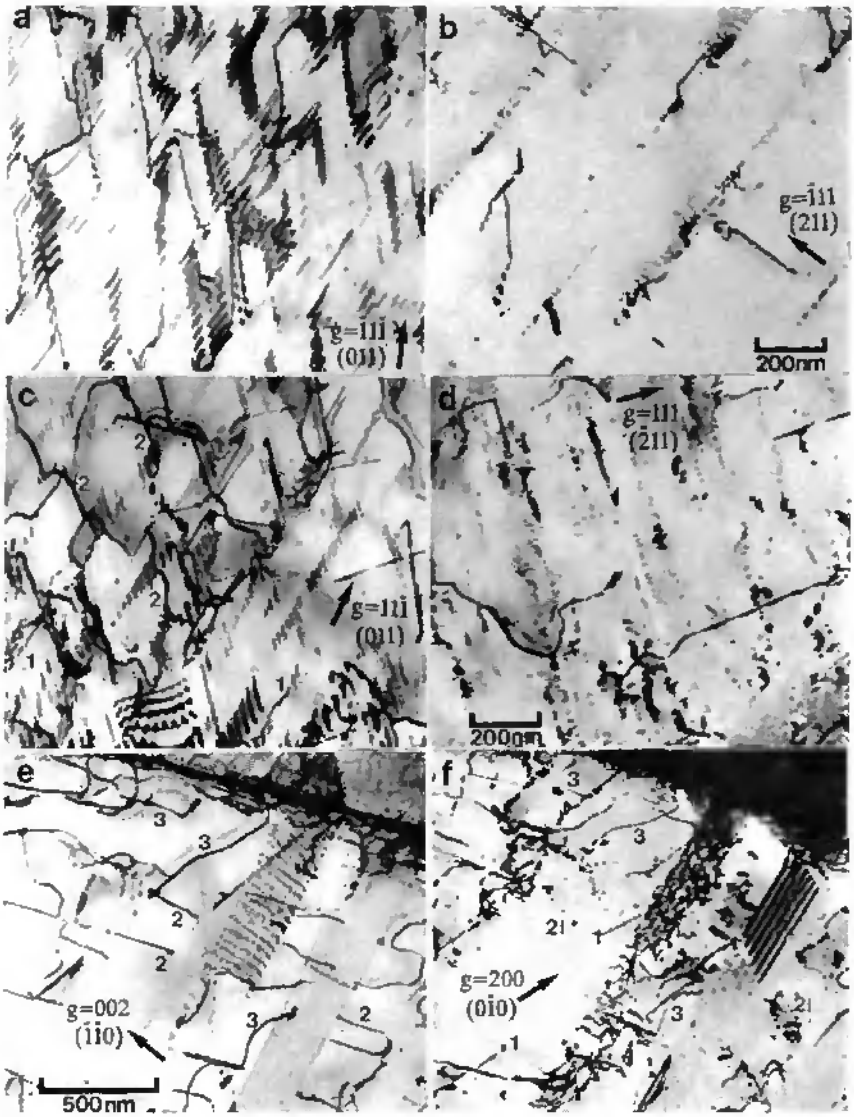

Figure 4.23 : Three lamellae that all contain a large number of superdislocations. The lamellae in (a)-(b) and in (c)-(d) also contain a large number of faulted dipoles or isolated stacking faults. In contrast, the third lamella (e)-(f) contained no stacking faults.

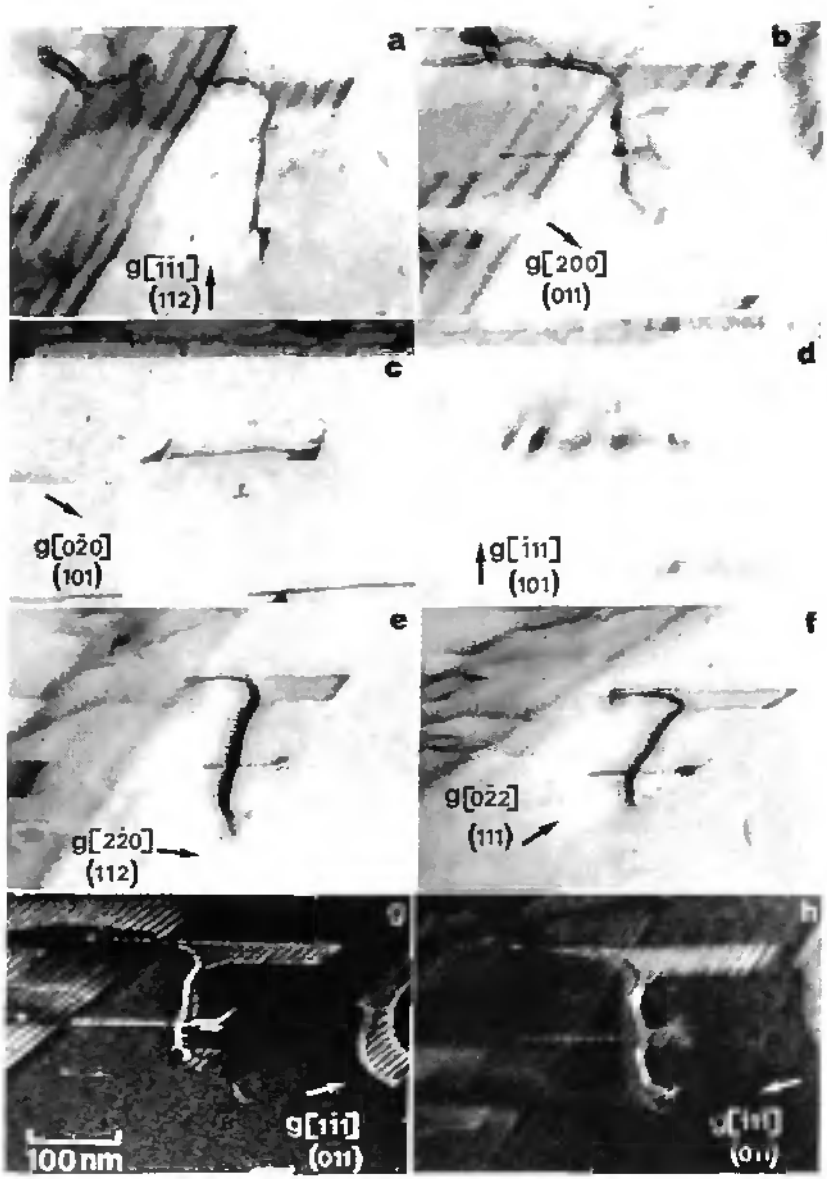

Figure 4.24 : Detailed analysis of a faulted dipole (lamella A Fig 4.20).

dislocation must be 1/6[1$\bar{1}$2]. The stacking fault is elongated in the [10$\bar{1}$] direction and the line direction of the long segment of the dislocation is [110].

	Dislocation	$g \cdot b_1$ = 1/2[1$\bar{1}$2]	Partial	$g \cdot b_p$ = 1/6[1$\bar{1}$2]	$g \cdot b_p$ = 1/6[12$\bar{1}$]	$g \cdot b_p$ = 1/6[211]
(112) $\bar{1}\bar{1}$1g	vis normal	1	in	+1/3	-2/3	-1/3
(011) 200g	vis normal	1	in	+1/3	+1/3	+2/3
(101) 0$\bar{2}$0g	vis normal	1	--	--	--	--
(10$\bar{1}$) $\bar{1}$11g	invis	0	--	--	--	--
(112) 2$\bar{2}$0g	vis double	2	vis	+2/3	+1/3	+1/3
(111) 0$\bar{2}$2g	vis double	3	vis	+1	-1	0
(011) 1$\bar{1}$1g	vis double	2	vis	+2/3	-1/3	+1/3
(011) $\bar{1}$11g	vis	-2	in	-2/3	+1/3	-1/3
(011) 11$\bar{1}$g **	vis	-1	in	-1/3	+2/3	1/3

Table 4.6 : Observed contrast for the main dislocation and the partial dislocation surrounding the fault and the predicted contrast for possible Burgers vectors. ** not shown in the Figure 4.24.

Grain	Dislocation	m	Line Direction	Plane	Fault Direction	Other Mechanisms in Grain
1A	1/2[1$\bar{1}$2]	0.26	[10$\bar{1}$] / [110]	($\bar{1}$11)	[10$\bar{1}$]	1/2[110]($\bar{1}\bar{1}$1), ($\bar{1}$11) twin
1E	1/2[$\bar{1}\bar{1}$2]	0.08	[0$\bar{1}$1]	(111)	[$\bar{1}$01]	1/2[1$\bar{1}$0] (111) ($\bar{1}\bar{1}$1), [10$\bar{1}$]($\bar{1}\bar{1}$1)
2A	--	0.11	---	($\bar{1}$11)	[10$\bar{1}$]	1/2[110]($\bar{1}$11), [101]($\bar{1}$11), [011]($\bar{1}\bar{1}$1)
2C	1/2[$\bar{1}\bar{1}$2]	0.18	[0$\bar{1}$1]	(111)	[$\bar{1}$01]	1/2[1$\bar{1}$0](111), [10$\bar{1}$](111)
6B	1/2[$\bar{1}$12]	0.12	---	($\bar{1}\bar{1}$1)	[$\bar{1}$01]	1/2[110] ($\bar{1}$11) ($\bar{1}\bar{1}$1), [10$\bar{1}$](111), [0$\bar{1}$1](111)

Table 4.7 : Summary of observations for the formation of faulted dipoles (both microstructures).

Finally, a summary of the observations of the faulted dipoles is given in Table 4.7 including the dislocation associated with the fault, the Schmid factor for this slip system, the direction of the dislocation line and fault and other mechanisms which were identified within the grain. It is interesting to note that the elongated fault direction is always along a <101] direction since this is proposed to play an important role in the formation mechanism of the faults [20]. It should also be noted that the dipole arrangements are often seen for low values of the Schmid factor, m.

In conclusion, it has been shown in this section that :

1.) the faulted dipoles are associated with 1/2<112] superdislocations,
2.) the faults are only surrounded by partial dislocations of the type 1/6<112],
3.) the faults are elongated in a <101] direction,
4.) and the dislocation and fault are coplanar.

4.2.4 Twinning

The observations of twinning in this structure are similar to those presented for the equiaxed structure and will, therefore, not be repeated here. Again, the apparent possibility for the twin to propagate in either direction is shown in Figure 4.25. It is seen that two twins on the $(1\bar{1}1)$ plane intersect a third twin on the $(\bar{1}\bar{1}1)$ plane. For the lower twin labelled A, the partial dislocations appear to move from left to right (according to their curvature) and are stopped at a third twin, thus, forming a pile-up to the left of the intersected twin. Contrarily, the curvature of the partial dislocations in the upper twin indicated by B indicates a sense of movement from right to left and the pile-up on the right side of the twin supports this sense of movement.

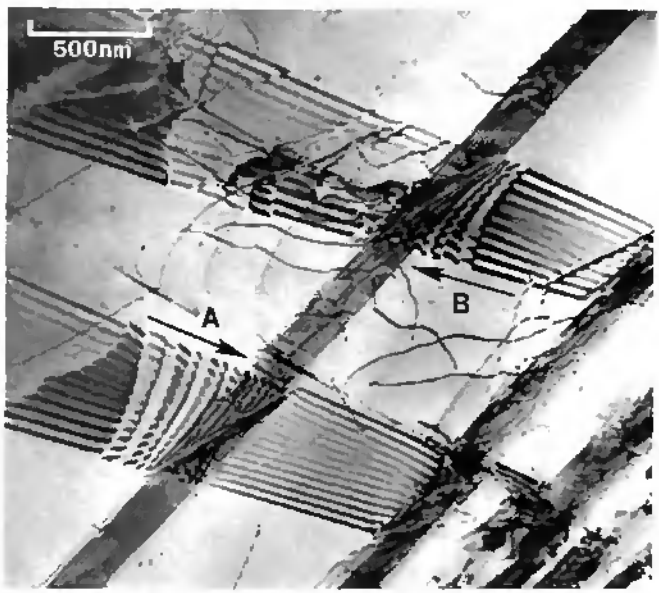

Figure 4.25 : Apparent propagation of the twinning dislocations in the opposite sense.

4.2.5 Summary

A summary of all observations of the lamellar microstructure is given in Table 4.8 which gives the Schmid factor for the systems which were identified in each grain. In Table 4.8(a), a summary is given of the coarse lamellae, while the results of the analysis of the fine lamellae are given in Table 4.8(b). It can be seen that the results on the coarse lamellae are comparable to those of the equiaxed microstructure in that several mechanisms are active in each grain at roughly similar values of m and that twinning and ordinary dislocations are the preferred deformation modes. Superdislocations and stacking faults are relatively more common in the lamellar structure, while less twinning is observed. The orientations of the grains identified is summarized in Figure 4.26(a) and the influence of loading orientation on the deformation mechanisms is shown in Fig 4.26(b). The differences in the deformation mechanisms in the two microstructures can be partially explained by differences in the orientations of the sample population for each structure.

The influence of loading orientation on the deformation mechanisms is presented schematically in Fig 4.26(c) and can be summarized by the following generalizations :

1.) ordinary dislocations are active in virtually every grain (except for the lamella where four twinning systems were activated) and for $m > 0.25$.

2.) twinning is prevalent for loading orientations near [001] and for values of $m > 0.25$. One notable exception to this is twinning observed in the area designated 3L with $m = 0.06$. This observation will be discussed separately below.

3.) in lamellae where twinning doesn't appear to be favorable, superdislocations may be observed. <101] superdislocations are observed for $m = 0.21$ to 0.49, while 1/2<112] superdislocations are observed at both high and low values of m. As in the equiaxed structure, there are many grains for which $m > 0.35$ for a <101] superdislocation slip system, but only twinning and ordinary dislocations are observed. This again indicates that twinning and ordinary dislocations are the preferred deformation modes and superdislocations are only observed in grains where twinning is unfavorable.

4.) extensive stacking faults and faulted dipoles are observed only in grains with a loading direction 10-15° from <111>.

These observations are essentially in agreement with the conclusions presented for the equiaxed structure.

observed	1A	1B	1B	1F	2A	2B	2C	2D	2G	4	6	3C	3D	3L	3Z
ordinary 1/2<110] dislocations	.23	.23/.16	.28/.15	.31	.31	.30/.21	.37	.49/.14 .41/.22	.35/.24	.25	.47 .49	.31/.18	.35/.24	.44	-
twinning systems	.26	.46 .45	-	-	-	-	-	-	.26	.46 .46	-	.40	.30 .24	.06	.48 .39 .28 .45
<101] superdislocations	-	-	.38	.47	.38 .24	.49	.34	-	-	-	(.21)	-	-	-	-
1/2<112] superdislocations	.26	-	.07	.30	-	.42 .30	.18	-	.26	-	(1)	-	-	.17	-
faulted dipoles or stacking faults	(1̄11)	-	(111)	-	(1̄11) (11̄1)	-	(111)	-	(111)	-	-	-	-	(111)	-
total sys	3	3	3	3	3	4	3	2	3	3	4	2	3	3	4
° boundary	80	76	78	78	79	79	77	72	83	73	79	84	86	85	52
mode	hard	hard	hard	hard	hard	hard	hard	hard	hard	hard	hard	hard	hard	mixed	hard
t, μm	2.3	5.4	1.7	5.4	5.5	3.0	2.4	1.7	2.2	4.6	4.1	1.9	1.0	4.6	3.5

Table 4.8(a) : Summary of the Schmid factors, m, for slip systems that have been observed in the coarse lamellae. Also given is the plane of any stacking faults or faulted dipoles that were observed, the total number of deformation systems active in the grain, the approximate lamellar thickness, t, the angle between the loading direction and the normal to the lamellar interface and the dominant deformation mode, hard or easy. If specific system wasn't identified in detail, the number of systems of this type are then given in parentheses. For screw dislocations where a unique slip plane cannot be defined, *the Schmid factor for both slip systems is given.*

observed	1G	1H	10B	10C	10E	10X	4A	4B
ordinary 1/2<110] dislocations	-	-	.44/.27	.28	-	.46	-	-
twinning systems	.45	-	-	.35	.08	.05	-	.50
<101] superdislocations	-	.37	-	-	-	-	.45	-
1/2<112] superdislocations	-	-	-	-	-	-	-	-
faulted dipoles	-	-	-	-	-	-	-	-
total systems	1	1	1	2	1	2	1	1
mode	hard	hard	mixed	mixed	hard	hard	hard	hard
° boundary	77	80	62	56	62	85	60	60
t, nm	270	170	450	460	130	700	230	150

Table 4.8(b) : Summary of the Schmid factors, m, for slip systems that have been observed in the fine lamellae. Also given is the plane of any stacking faults or faulted dipoles that were observed, the total number of deformation systems active in the grain, the approximate lamellar thickness, t, the angle between the loading direction and the normal to the lamellar interface and the dominant deformation mode, hard or easy. If specific system wasn't identified in detail, the number of systems of this type are then given in parentheses. For screw dislocations where a unique slip plane cannot be defined, the Schmid factor for both slip systems is given.

a.)

b.)

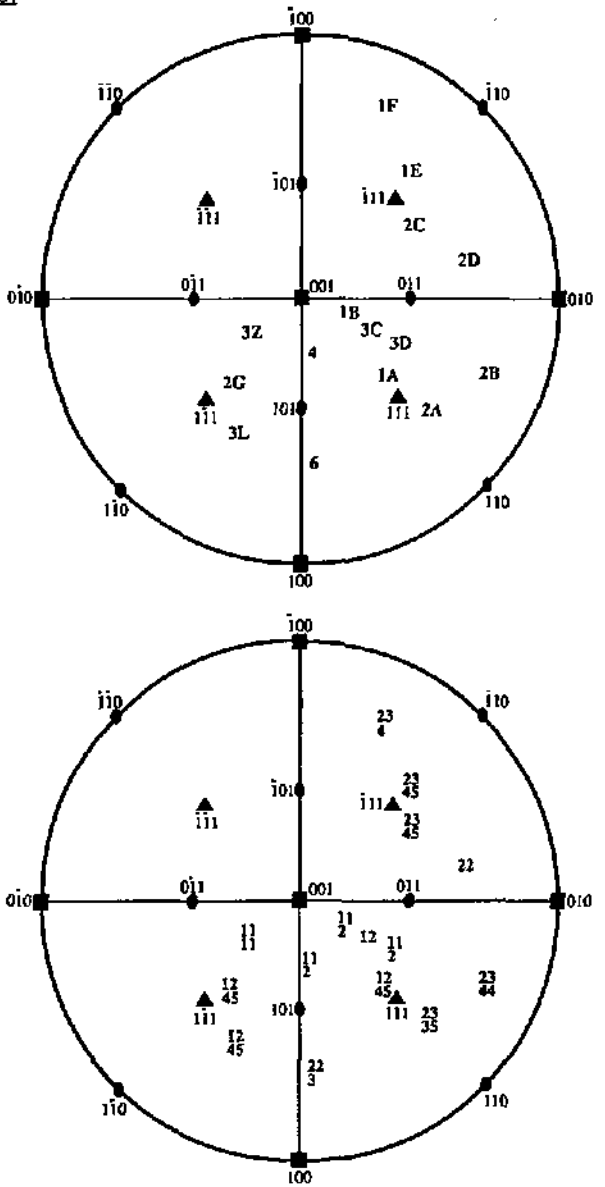

Figure 4.26 : Summary of the influence of (a) loading orientation on (b) the deformation mechanisms in the coarse lamellar structure 1) twinning, 2) 1/2<110], 3) <101], 4) 1/2<112] and 5) faulted dipoles.

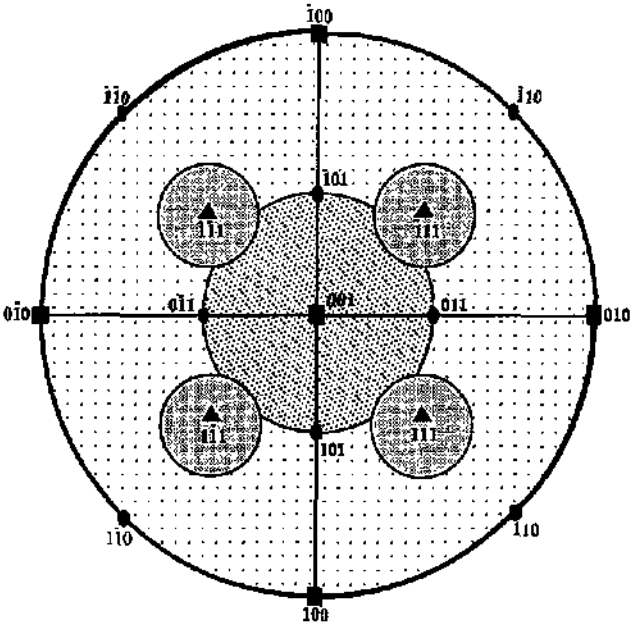

Figure 4.26(c) : Schematic diagram showing the influence of loading orientation on the observed deformation mechanisms. Deformation twinning is most frequently observed in the central shaded portion centered on the [001] pole, while <101] and 1/2<112] superdislocations are confined to the regions outside of this area (lightly shaded). Finally, the circles around the <111> poles indicate the areas where faulted dipoles have been identified as an important deformation feature. Ordinary dislocations are observed for all loading orientations.

4.2.6 Influence of Lamellar Thickness

The deformation behavior of the fine lamellar regions differs from the coarse structures in two ways. Firstly, there tends to be one dominant mechanism throughout the lamellae. This is clearly shown by comparison of grain B (Figure 4.18) with similarly oriented fine lamellae in Figure 4.22. Secondly, there appears to be less preference for the ordinary dislocation modes since superdislocations were observed in lamellae *1H* and *4A* even though ordinary dislocation systems with m = *0.48* or *0.41* and m = 0.40 were available for the two lamellae, respectively. It should be noted that lamellae 10B, 10C, 10E and 10X correspond to deformation structures in the as-cast material.

4.2.7 Hard versus Easy Modes of Deformation

In the lamellar microstructures, two types of deformation are possible which have been defined as the "hard" and "easy" types [11]. As previously stated, for the easy types of deformation, dislocation glide or deformation twinning occurs on {111} planes which are parallel to the lamellar interface. In contrast, hard modes of deformation occur on {111} planes which are inclined to the lamellar boundary. It has been stated that the hard modes of deformation are active when the loading orientation is nearly parallel or perpendicular to the lamellar interface, while the easy mode is active for intermediate loading orientations. In light of this, the angle between the loading direction and the normal to the lamellar interface, ϕ, is given in Table 4.8 along with the observed mode (hard, easy or mixed). It can be seen that all of the coarse lamellae deform by the hard mode of deformation, even for the lamella with ϕ=52° (3Z). This tendency is also emphasized in the fine lamellar structures since all grains either exhibit only hard or mixed deformation modes even for the angles down to 56°.

The lamella designated 3L in Table 4.8 exhibited unusual behavior in that 1.) twinning was observed for a Schmid factor m = 0.06 and that 2.) this was the only coarse lamella which deformed extensively by the easy mode. An overview of this lamella and the surrounding area is shown in Fig 4.27(a). In this micrograph, the deformation twins are viewed edge-on. The hole of the thin film foil is seen to the left of the micrograph, while in the upper right region a coarse, equlaxed γ grain is seen as indicated with the star. In Fig 4.27(b), the deformation twinning on the $(\bar{1}\bar{1}1)$ planes parallel to the lamellar boundary (m = 0.06) is no longer viewed edge-on and, therefore, is clearly seen. $1/2[1\bar{1}0](111)$ ordinary dislocations (m = 0.44), $1/2[\bar{1}\bar{1}2](111)$ dislocations (m = 0.17) and many stacking faults on the (111) plane are also identified in this lamella. While the dislocations and stacking faults could be expected on the basis of the Schmid factors and loading orientation, deformation twinning on the $(\bar{1}\bar{1}1)$ plane is not expected for such a low value of m. However, as shown in Fig 4.27(a), this lamella is adjacent to an equiaxed γ grain and it could be expected that the stress distribution in this boundary region could be significantly different than that expected on the basis of the applied load. Hence, it is presumed that these twins are created because of localized stress concentrations at the grain boundary rather than directly due to the applied loading. This is substantiated by the observation that all eight of these twins end after propagating only a short distance into the lamella. The longest twin propagates approximately 15μm into the grain - presumably where the localized boundary stress decreases to insufficient values and the stress distribution is better predicted by the loading orientation.

A second example of the influence of the easy mode of deformation is observed in the lamella 3Z where all four twinning systems were activated. In the large area examined (16 μm long), only two twins parallel to the $(\bar{1}\bar{1}1)$ interface, i.e. the easy mode, were observed in spite of a Schmid factor m = 0.45. In contrast, seven $(1\bar{1}1)$ twins were observed with m = 0.48, nine (111) twins with m = 0.39 and even three $(\bar{1}11)$ for m = 0.28. Thus, even though the Schmid factor is rather high

for $(\bar{1}\bar{1}1)$ twinning and it would be expected to be a dominant deformation mechanism, all three hard twinning systems are more prevalent.

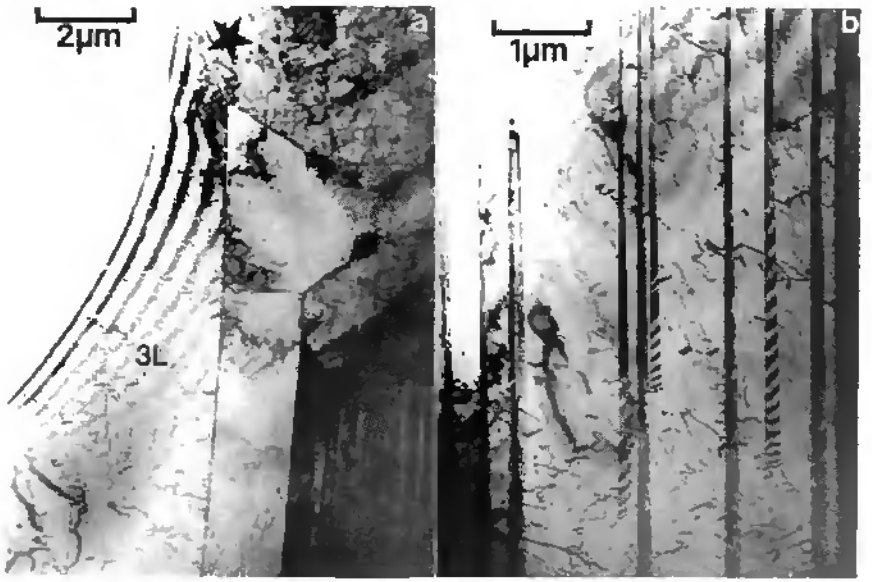

Figure 4.27 : Deformation twinning which occurs on the plane parallel to the lamellar interface. (a) An overview showing that this area is adjacent to an equiaxed zone and (b) twins clearly shown.

In conclusion, it can be said that the hard modes of deformation are much more common than the easy modes. This is even true for loading orientations of 52-56° where the easy modes could be expected to occur. However, deformation on planes parallel to the boundary plane can be activated in the grain boundary regions due to localized stress concentrations at the boundary. For this localized activation, the slip systems will propagate only when the localized stress is sufficiently large.

4.2.8 Deformation in the α_2 Phase

As previously stated, deformation structures were rarely observed in the α_2 phase of the fine lamellar zones in the heat-treated and deformed lamellar structure. However, it was possible to observe deformation structures in the α_2 phase in the as-cast and deformed material, presumably since these lamellae are coarser than those in the transformed lamellar structure. For example, in Figure 4.28 some typical deformation structures in a coarse (350 *nm*) α_2 lamella are seen. In this lamella, a row of straight dislocations is observed along with a deformation twin. In this lamellar colony, both curved or straight dislocations and twins are commonly observed in all the coarse α_2 lamellae.

However, it must be noted that the density of dislocations and twins is significantly lower than that observed in the adjacent γ lamellae.

Figure 4.28 : Deformation structures observed in a coarse α_2 lamella including individual dislocations and a deformation twin.

Further observations of another lamellar colony are given in Figures 4.29 and 4.30. In Fig 4.29(a), two coarse, similarly oriented γ lamellae are seen to be separated by a coarse α_2 lamella (indicated A). Also, within both of the γ lamellae, fine α_2 lamella are seen. The influence of α_2 thickness on the propagation of the twins in γ is clearly seen by comparing the behavior of the lamellae A and B. For the coarse lamella A (~430 nm thick), the twins are stopped at the boundary and there is no correspondence with the twins in the neighboring γ. In contrast, the twins appear to be transmitted directly through lamella B (~25nm thick) since there is a one-to-one correspondence with twins on either side of the lamella. Therefore, it is readily concluded that the α_2 lamellar thickness plays an important role in the transmission of deformation through the lamellar structure.

In the thick lamella A, two different types of dislocation structures were observed. A low density of dislocations were observed throughout the thickness of the lamella and these were distributed rather homogeneously along the length of the lamella (these are invisible in Fig 4.29a). In contrast, a second type of dislocations are limited to the interface regions immediately adjacent to the γ as indicated by the arrows (Fig 4.29a). Contrast experiments to identify the dislocations within the lamella are shown in Figs 4.29(b)-(e). Since the dislocations are invisible in Fig 4.29(b) with the 0002g, they must be <a> type dislocations. Furthermore, since they are visible with the $22\bar{4}0$g, they must be either $[11\bar{2}0]$ or $[1\bar{2}10]$ dislocations. The assumed slip planes for these dislocations would then be $(1\bar{1}00)$ or $(10\bar{1}0)$, respectively. Although the contrast experiments provide no further differentiation between these two systems, trace analysis was used to determine the line direction of the dislocations to be approximately parallel to $[11\bar{2}0]$. If the Burgers vector was also parallel to $[1\bar{2}10]$, then the slip plane would be defined by (0001). However, this cannot be the case since the dislocations are not straight as would be expected if they were glissile on the basal plane. However, if the Burgers vector is parallel to $[11\bar{2}0]$, then these dislocations would be in the screw orientation on

the $(1\bar{1}00)$ plane. Geometrical consideration of the length of the dislocations confirms the conclusion that these are $[11\bar{2}0]$ dislocations on the $(1\bar{1}00)$ plane since they appear the longest for $B = 1\bar{1}00$ (viewed nearly flat in the foil) and are roughly half the length for $B = 10\bar{1}0$ (inclined in the foil 60° and cos60° = 0.50). Thus, it is confirmed that these dislocations are $1/6[11\bar{2}0]$ dislocations on the $(1\bar{1}00)$ plane for which m = 0.48. It is interesting to note that these dislocations appear to be present either individually or in pairs (1) and that complex dissociations may also be possible (2).

The dislocations in the vicinity of the interface are examined in more detail in Figure 4.30. It is immediately seen that these dislocations are visible for the 0002g and, thus, must be either <a>+<c> or <c> type dislocations. However, since the dislocations are invisible for both $02\bar{2}0$g and $2\bar{4}20$g, they can only be of the Burgers vector [0001]. Again, by comparison of the length of the dislocation in different beam directions, it can be determined that the probable slip plane is near $(1\bar{1}00)$. This is readily verified in Figs 4.30(a)&(b) where the dislocation is the longest for $B = (1\bar{1}00)$ and approximately half the length for $B = (10\bar{1}0)$. Of the possible $\{1\bar{1}00\}$ and $\{11\bar{2}0\}$ type planes, only the $(1\bar{1}00)$ plane matches these geometrical observations. It is possible that other higher index planes very near $(1\bar{1}00)$ could also be the slip plane, however, the current analysis cannot provide any more precision for the slip plane. It must again be emphasized that these were only found as loops or short segments immediately adjacent to the interface and were often associated with a twin in the γ lamella. The Schmid factor for this system is only m = 0.05 and, thus, it is unlikely that these can be attributed directly to the applied loading. The origin of these dislocations will be discussed in more detail in Section 5.1.5.

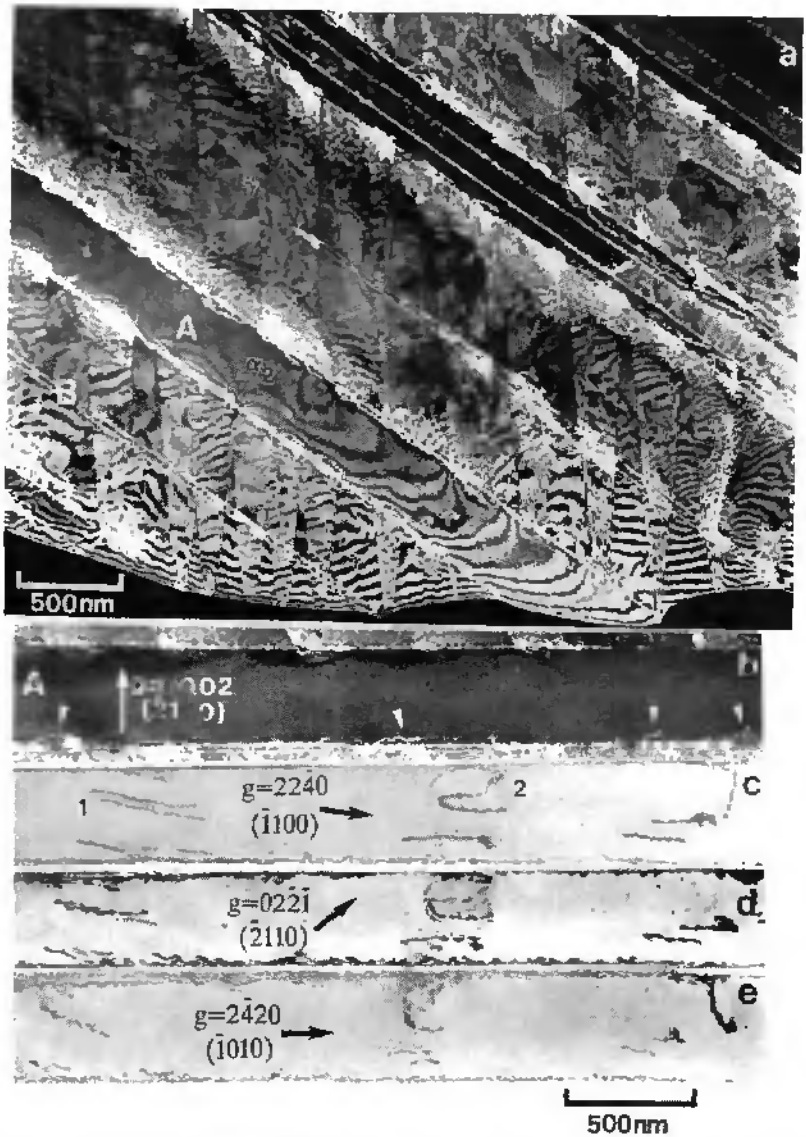

Figure 4.29 : (a) Deformation of a typical lamellar zone, (b) weak beam micrograph showing the occurrence of many short dislocation segments at the γ/α_2 interface in the α_2 lamella A and (c)-(e) contrast analysis to identify dislocations in the interior of the lamella A.

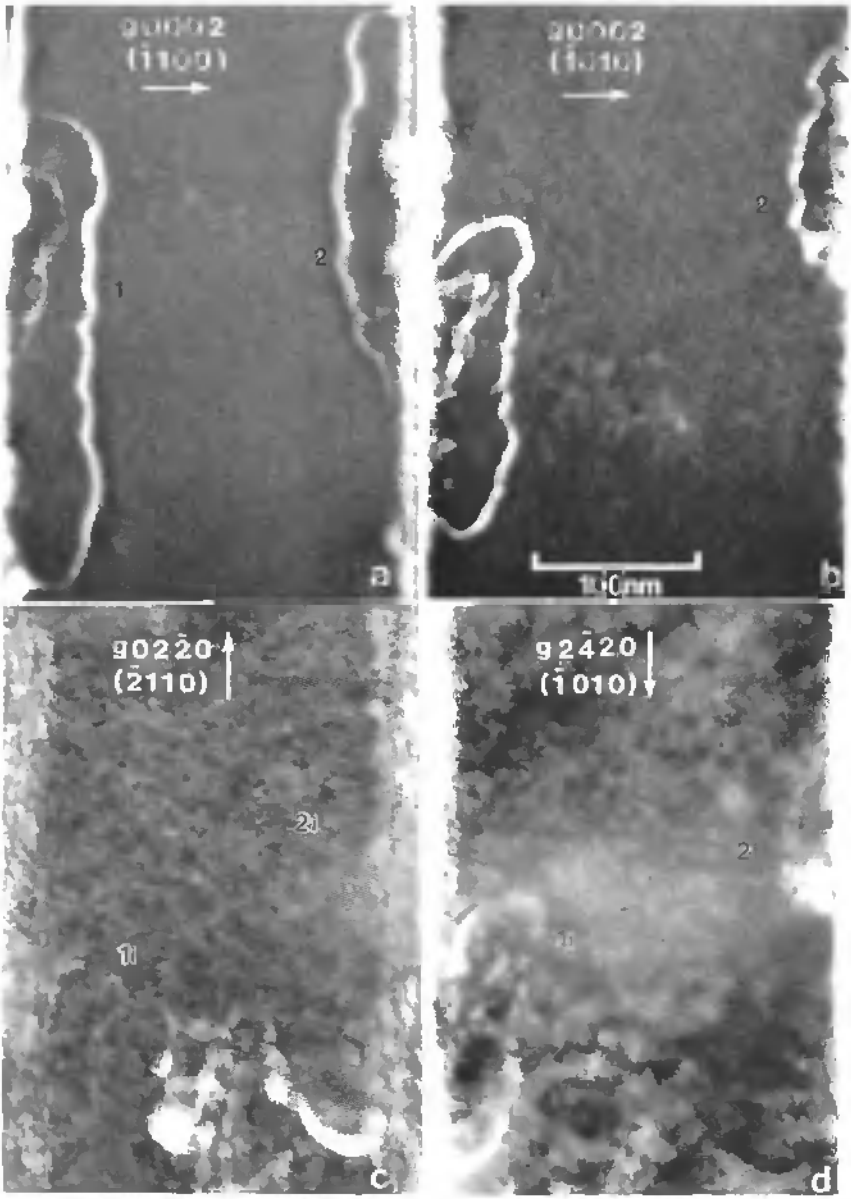

Figure 4.30 : Detailed contrast experiments to identify the dislocations segments confined to the interfacial region in the α_2 lamella A of Fig 4.29(b).

4.3 Geometric Compatibility and Slip Transfer

In this section, the influence of the specific orientation relationships on the activation and transmission of the deformation processes will be investigated. In this context, the geometric compatibility factor which was introduced in Section 1.5.2 will be used to ascertain the compatibility of individual deformation systems in one grain relative to the deformation systems in the adjacent grain. With the help of this factor, it should also be possible to determine whether the specific type of orientation relationship is important in the transfer process. Are the transfer mechanisms the same for the 60°, 120° and 180° rotation orientation relationships? Similarly, does the microstructure have an influence on the transfer of deformation between adjacent grains?

4.3.1 Equiaxed Microstructure

In general, several deformation mechanisms are active within each equiaxed grain. Therefore, it is *difficult to correlate a deformation mechanism in one grain with a single mechanism in the adjacent* grain since several possible combinations exist. However, in some instances, it is possible to directly relate the mechanisms in one grain with the activation of systems in adjacent grains. Several examples of this will be given below for the various rotations.

As an initial example, reference is made to the grains A and E shown in Figure 4.1. Twinning on the $(1\bar{1}1)$ plane is active in each grain and there appears to be a correspondence in the activation of these twinning systems across the grain boundary. This correspondence is emphasized in Figure 4.31(a). A higher magnification micrograph is given in Fig 4.31(b) which shows that a significant pile-up of dislocations occurs at the A / E boundary. Although this grain boundary is generally irregular, trace analysis was used to determine the local boundary plane as (110) and the rotation between the two grains is described by 60° anti-clockwise as given in Figure 4.2. In order to examine how the twinning in E may influence the activation of deformation in A, the compatibility factors have been computed in Table 4.9. Also listed are the appropriate Schmid factors.

As can be seen in Table 4.9, several deformation systems could be expected in grain A on the basis of the Schmid factor and that several possible slip systems would provide moderate compatibility with *the twinning in grain E. Of the five possible systems with $m' > 0.50$, the ordinary dislocation* system can be eliminated since the Schmid factor is very low for this system. Similarly, the three <101] superdislocation systems can be eliminated since these are generally observed only when ordinary dislocations and twinning are not possible. This leaves the two twinning systems which were both identified in grain A - namely, the $(1\bar{1}1)$ and $(\bar{1}11)$ twinning. On the basis of the Schmid factor alone, both systems are more or less equally expected to be distributed homogeneously throughout the grain. However, only the $(1\bar{1}1)$ twinning was observed near the A/E interface and this can be attributed to the better geometric compatibility with the twinning in grain E. Hence, it appears

that the geometric compatibility can be used to understand the preferential activation of the $(1\bar{1}1)$ twinning system at the A/E boundary.

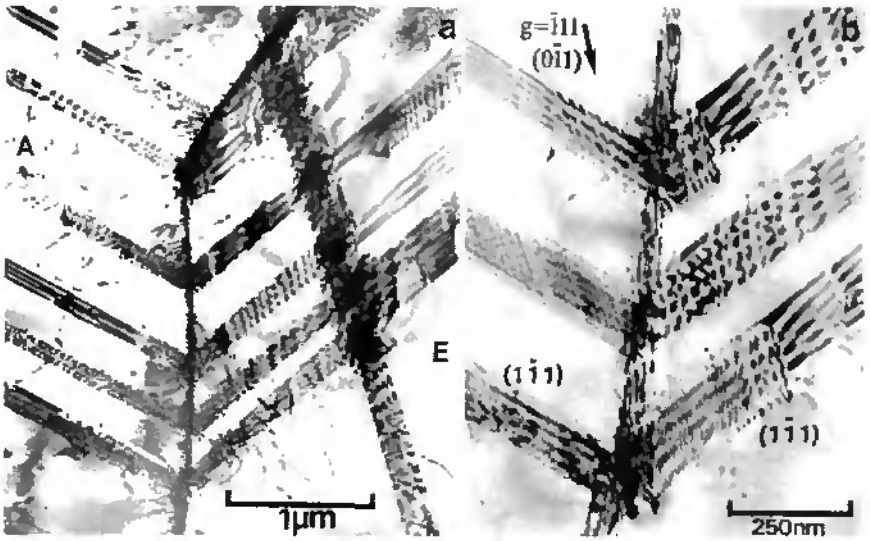

Figure 4.31 : Transmission of deformation twinning from equiaxed grain E to A (from Fig 4.1).

Possible Slip in A	m	m'	Observations
[011] $(1\bar{1}1)$	.28	.54	---
[011] $(\bar{1}\bar{1}1)$	.31	.54	---
$[\bar{1}12]$ $(1\bar{1}1)$	.34	.53	at A/E interface
1/2$[1\bar{1}0]$ (111)	.06	.52	---
$[\bar{1}01]$ (111)	.23	.52	---
$[1\bar{1}2]$ $(\bar{1}11)$	.29	.05	at A/F interface

Table 4.9 : Geometric compatibility of possible slip systems in A for 1/6$[\bar{1}12]$ $(1\bar{1}1)$ twinning in the adjacent grain E which is rotated by 60° anti-clockwise relative to A.

Further information about the geometry of this process is given in the stereographic projection (in area E coordinates) in Figure 4.32. *The trace of the* $(1\bar{1}1)$ *twin plane in grain E is drawn. Using the* 60° rotation relationship, the indices of the twin plane in A can be determined to be (511) in the E coordinate system, while the twinning direction is transformed to $[\bar{2}55]$. The intersection of these two twin planes is given by the direction $[\bar{1}23]$ which is approximately contained in the (110) boundary plane. Apparently, this geometry is not a favorable transfer process since there are dislocation pile-ups or reflection at the interface. In this regard, there does not appear to be a direct transfer of the

deformation from grain to grain. Rather, the pile-up in one grain seems to create a stress concentration which is relieved by flow in the adjacent grain. In this light, it is interesting to note that the geometric compatibility calculation can give some information regarding the selection of the deformation system in the adjacent grain.

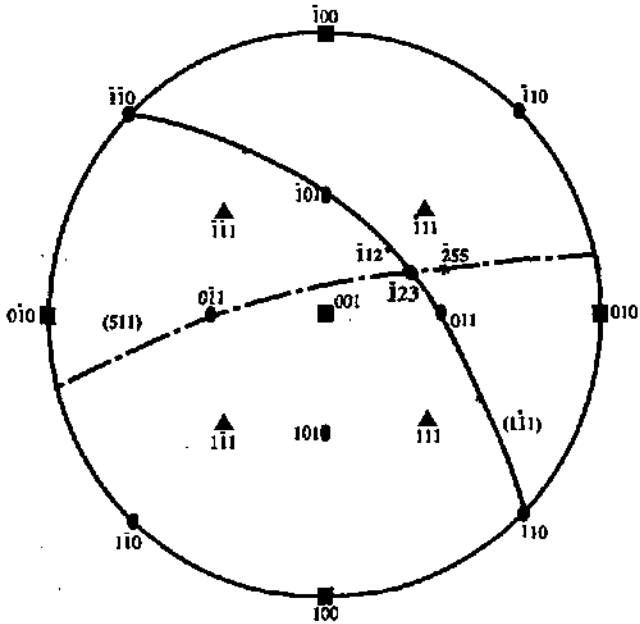

Figure 4.32 : Geometry of the transmission of $(1\bar{1}1)$ twins between grains A and E.

The influence of the geometric compatibility of slip systems in adjacent grains is also seen in the inhomogeneous activation of superdislocations in the grain F (Figure 4.4). In order to recall this physical situation, a schematic diagram of the deformation mechanisms in grain F and the neighboring grains is given in Figure 4.33. It can be seen that in the region near the F/E interface (where grain E deforms primarily by twinning on the $(1\bar{1}1)$ and $(\bar{1}\bar{1}1)$ planes), grain F deforms only by the glide of ordinary dislocations. In contrast, near the F/A interface (where grain A deforms primarily by $(\bar{1}11)$ twinning), localized activation of superdislocations is also observed. The geometric compatibility of the twinning systems in grains E and A have been calculated in Table 4.10 in order to determine the geometrically favorable slip systems in grain F.

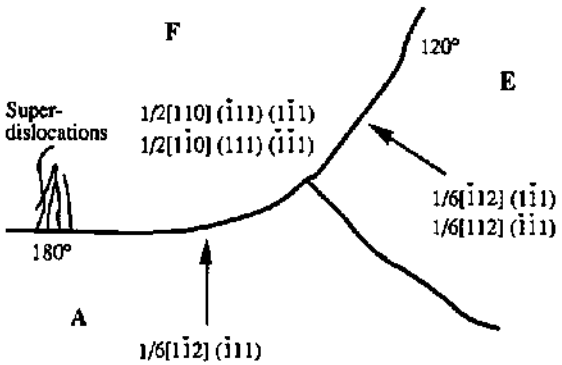

Figure 4.33 : Schematic diagram of the deformation mechanisms in the equiaxed grains A, E and F.

Possible Slip in F	m	m'	Observations
1/2[110] (1$\bar{1}$1)	.47	.87	active in F
[10$\bar{1}$] (1$\bar{1}$1)	.32	.87	---
[$\bar{1}$12] (1$\bar{1}$1)	.11	.50	---
[101] ($\bar{1}$11)	.35	.10	---

Table 4.10(a) : Geometric compatibility of possible slip systems in F with 1/6[112] ($\bar{1}$1$\bar{1}$) twinning in grain E for a 120° rotation about [$\bar{1}$11].

Possible Slip in F	m	m'	Observations
1/2[1$\bar{1}$0] (111)	.49	.87	active in F
[10$\bar{1}$] (111)	.28	.87	---
[$\bar{1}\bar{1}$2] (111)	.02	.50	---
[101] ($\bar{1}$11)	.35	.10	---

Table 4.10(b) : Geometric compatibility of possible slip systems in F with 1/6[$\bar{1}$12] (1$\bar{1}$1) twinning in grain E for a 120° rotation about [$\bar{1}$11].

Possible Slip in F	m	m'	Observations
[1$\bar{1}$2] ($\bar{1}$11)	.27	1.00	activated ??
[101] ($\bar{1}$11)	.35	.87	---
1/2[1$\bar{1}$0] (111)	.49	.19	active in F
1/2[1$\bar{1}$0] ($\bar{1}\bar{1}$1)	.19	.19	active in F
1/2[110] (1$\bar{1}$1)	.47	0.0	active in F
1/2[110] ($\bar{1}$11)	.22	0.0	active in F

Table 4.10(c) : Geometric compatibility of possible slip systems in F with 1/6[1$\bar{1}$2] (1$\bar{1}$1) twinning in grain A for a 180° rotation about [$\bar{1}$11].

Examination of Tables 4.10(a)&(b) reveals that the there is a good compatibility between the deformation systems which have been observed in the grains E and F and, therefore, there is no need for the activation of any other systems. Compatibility can be maintained at the interface without further modes of deformation. In contrast, Table 4.10(c) shows that the compatibility of the deformation systems in grains A and F is low (0.19 and 0.0 for the four ordinary dislocation systems which are active in F). Thus, in order for coherency to be maintained between the two grains, additional deformation modes must be activated in either grain A or F. Thus, activation of a superdislocation system in F appears to be required to maintain coherency at the interface. Unfortunately, the foil thickness did not allow for exact determination of the Burgers vector of these dislocations; however, it is interesting to speculate that these are 1/2[$1\bar{1}2$] superdislocations since these would exhibit complete compatibility. Regardless of the Burgers vector of these dislocations, calculation of the compatibility between the active deformation systems in grains A and F can be used to predict the need for additional slip systems.

A final example of the transfer of deformation between adjacent grains is shown in Figure 4.34. In Fig 4.34(a), five deformation twins are seen in grain I (to the right side of the micrograph) which intersect the adjacent grain II (at the left side). The orientation relationship between these two grains is 120° about [$\bar{1}\bar{1}1$]. The boxed region in Fig 4.34(a) is shown at a higher magnification in Fig 4.34(b) and it can be seen that the intersection of the twinning system in grain I with grain II results in the emission of 5-10 dislocations in the adjacent grain II as indicated by the arrow head. Trace analysis was used to identify the twin plane in grain I as ($\bar{1}\bar{1}1$). Similarly, contrast experiments and trace analysis were also used to determine the dislocations in grain II as 1/2[$\bar{1}10$] dislocations on the ($\bar{1}\bar{1}1$) plane. In Fig 4.34(b), these dislocations appear to be continuous with the twin, while in Fig 4.34(c) the glide plane in II and twin plane in I are both viewed edge-on. This confirms that the deformation continues from grain I to the adjacent grain II on a corresponding slip plane. The schematic diagram of this situation given in Fig 4.34(d) emphasizes that the deformation transfers between the grains on the same {111} plane, which in this case is the ($\bar{1}\bar{1}1$). Calculation of the geometric compatibility of these two systems gives m' = 0.87 which is the maximum possible value for the given twinning system. The Schmid factors for both systems are, however, rather low and it appears that this situation was created during the heat treatment process. Nevertheless, it is a useful example since it shows that the value of m' is apparently an important factor in selection of the deformation system in the adjacent grain, m' is generally high for 120° rotations, and for certain rotations there appears to exist a possibility for continuing deformation from one grain to the next on a corresponding slip plane.

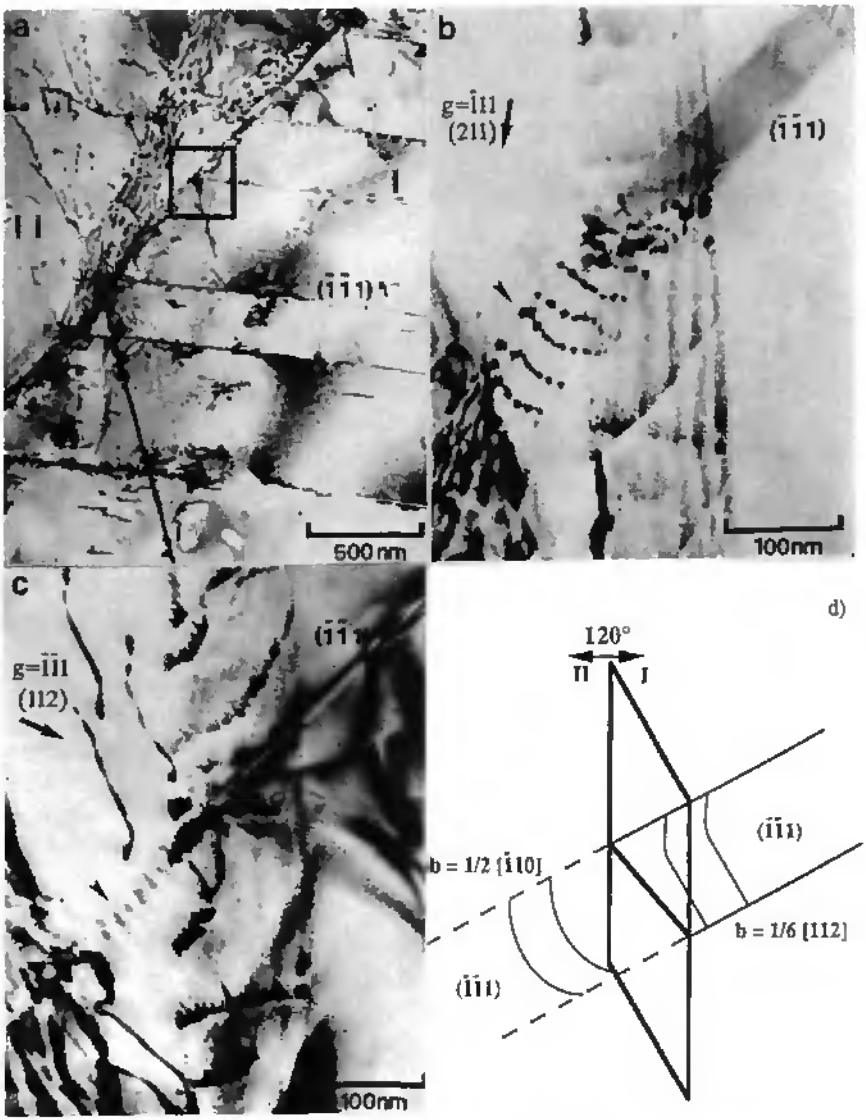

Figure 4.34 : Transfer of deformation between adjacent grains, related by a 120° rotation about [1̄1̄1], from twinning to slip of ordinary dislocations on the corresponding {111} plane.

4.3.2 Transformed Lamellar Structure

An example of the geometric compatibility of deformation systems in the lamellar structure is given in Fig 4.35(a) which shows two thin, adjacent lamellae, labelled A and B, embedded within a large colony of γ and α_2 lamellae. For these two lamellae A and B, the orientation relationship has been determined to be a 120° rotation about the $[\bar{1}\bar{1}1]$. It can be seen in both lamellae that 1.) the density of deformation structures is low and 2.) there appears to be only one active mode in each grain. Further contrast experiments used to identify these modes are shown in Figs 4.35(b)-(e). Since these lamellae are related by a 120° rotation, there is a correspondence between the {111} and {110} in each lamella such that diffraction conditions are simultaneously fulfilled in each grain and only the specific indices vary. Thus, for example, the diffracting conditions in Fig 4.35(b) are $(\bar{1}10)$ $\bar{1}\bar{1}\bar{1}$g in lamella A and $(10\bar{1})$ $\bar{1}11$g in B.

Trace analysis was used to determine the twin plane in lamella B as $(1\bar{1}1)$ and this is confirmed by the invisibility of contrast in Fig 4.35(e) ($\mathbf{g}\cdot\mathbf{R}_F = 0$). The Schmid factor for this twinning system is m = 0.50. In lamella A, a low density of individual dislocations can be seen of which two were examined in detail as indicated in boxed region Fig 4.35(a). Most of the dislocations correspond to the type 1, while only one isolated dislocation was identified like the dislocation 2. Dislocation 1 is invisible with 020g and $\bar{1}\bar{1}$1g and, thus, $\mathbf{b}_1 = [101]$. This is confirmed by the characteristic double contrast for the $\bar{1}\bar{1}\bar{1}$g (i.e. $\mathbf{g}\cdot\mathbf{b} = 2$) and visibility for $2\bar{2}0$g and 002g (not shown). Trace analysis indicated that the line direction was [211] such that the slip plane can be determined to be $(\bar{1}11)$. The contrast for dislocation 2 was unusual in that it appears invisible 020g which would indicate a Burgers vector parallel to [101] or $[\bar{1}01]$. However, the dislocation is visible for both $\bar{1}\bar{1}\bar{1}$g and $\bar{1}\bar{1}$1g which is inconsistent with either possible Burgers vector. Trace analysis indicated that the line direction was parallel to $[\bar{1}12]$ which would indicate that the dislocation should lie in the $(1\bar{1}1)$ plane. The possible Burgers vectors would thus be $[\bar{1}01]$, [011] and $1/2[\bar{1}12]$. [101] can be eliminated on the basis of the visibility for $\bar{1}\bar{1}$1g and [011] is also eliminated due to the visibility with the $\bar{1}$1g and the lack of the characteristic double image for $\bar{1}\bar{1}\bar{1}$g ($\mathbf{g}\cdot\mathbf{b}$ would equal 2). Hence, it is presumed that the dislocation is a $1/2[\bar{1}12]$ and this is confirmed by the invisibility with the $2\bar{2}0$g as shown in Fig 4.35(e). The screw orientation is not common for these dislocations and it is possible that this particular orientation or an unusual dissociation could account for the apparent invisibility seen for the 020g. However, it must be emphasized that this was the only dislocation in this lamella with this Burgers vector and that the rest of the dislocations were identified as $[101](\bar{1}11)$ dislocations.

In order to examine the influence of the compatibility requirements between the two lamellae, the geometric compatibility factor for possible deformation systems in lamella A has been calculated. These results are shown in Table 4.11, along with the Schmid factor for each system.

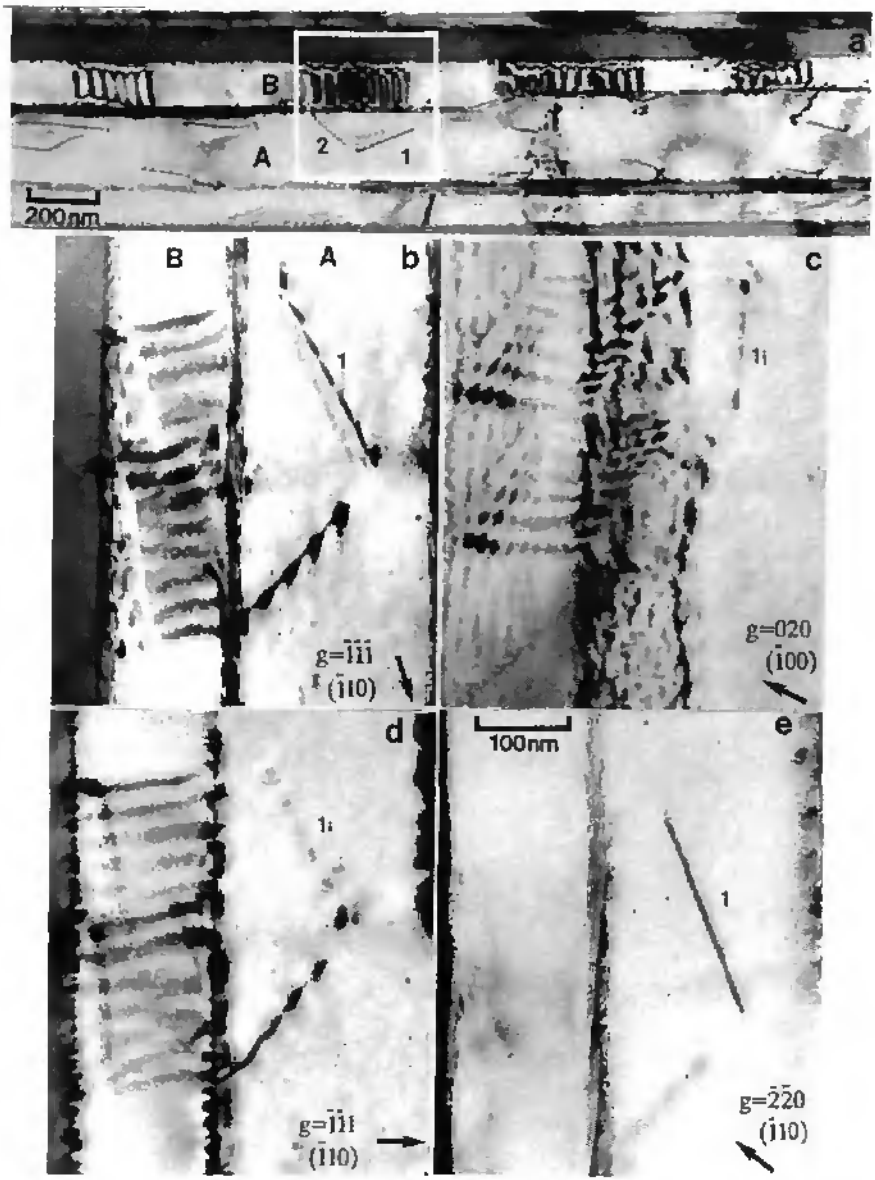

Figure 4.35 : (a) Overview of the deformation mechanisms in fine, adjacent γ lamellae related by a 120° rotation. Detailed contrast analysis of the boxed area in (a) is shown in (b)-(e).

Possible Slip in A	m	m'	Observations
[101] (1̄11)	.45	.87	identified in B
1/2[11̄0] (1̄11)	.40	.87	---
[1̄01] (11̄1)	.45	.10	---
1/2[1̄10] (1̄1̄1)	.40	.10	---
1/2[110] (11̄1)	.34	.28	---

Table 4.11 : Schmid factor and geometric compatibility factor, m', for the deformation systems lamellae A for 1/6[1̄12](1̄1̄1) twinning in the adjacent lamella B and a 120° orientation relationship.

This table indicates that both the Schmid factor and geometric compatibility factor are important in determining which mechanisms are active in the fine lamellae. Although 4-5 systems are possible on the basis of the Schmid factor, the actual deformation mode corresponds with the system which maximizes the compatibility of the two systems. It is interesting to note that the 1/2[11̄0](1̄11) system would give the same geometric compatibility as the [101](1̄11) system, and it also has a large Schmid factor m = 0.40. However, the fact that these ordinary dislocations were not identified would appear to contradict the observation that ordinary dislocations are preferred over the superdislocations.

An example of the compatibility of deformation systems in adjacent γ lamellae which are related by a 180° rotation about the [1̄1̄1] is shown in Figure 4.36. Both lamellae contain only ordinary dislocations and the Burgers vector of the dislocations in both lamellae is seen to be 1/2[11̄0]. A negligible density of 1/2[110] dislocations is also seen. Since practically none of the 1/2[11̄0] dislocations are observed to be straight segments parallel to the (1̄1̄1) lamellar interface, the slip plane of these dislocations cannot be the (1̄1̄1) plane. Thus, the deformation system in each lamella is characterized as 1/2[11̄0) (111). Furthermore, the geometric compatibility calculations for these two systems is given in Table 4.12. It is observed that several possible slip systems in C could be expected solely on the basis of the Schmid factor. However, the active system tends to be that which also yields the maximum geometric compatibility.

Possible Slip in C	m	m'	Observations
1/2[1̄10] (111)	.28	.78	active in C
1/2[1̄10] (1̄1̄1)	.32	.33	---
[11̄2] (1̄11)	.35	0	---
[1̄12] (111)	.34	0	---
[1̄12] (11̄1)	.35	.32	---
[011] (111)	.42	.39	---

Table 4.12 : Geometric compatibility for possible slip systems in C for 1/2[11̄0](111) dislocations in B and an orientation relationship of 180° about [1̄1̄1].

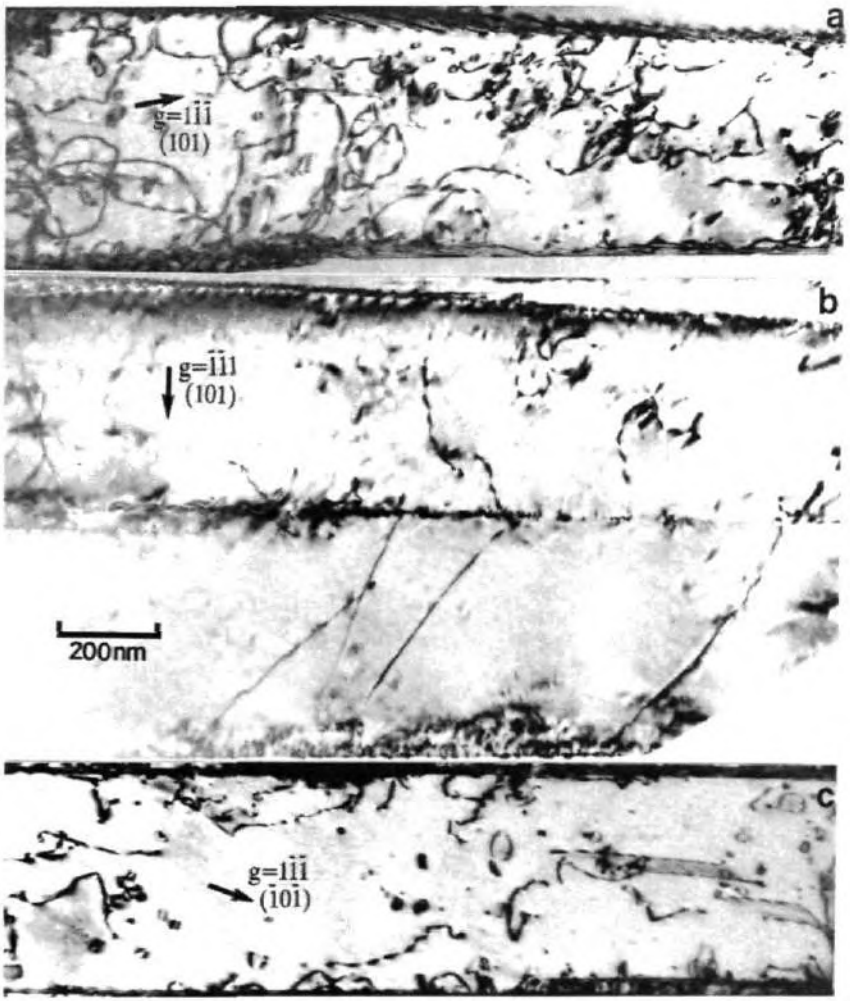

Figure 4.36 : Deformation mechanisms in adjacent γ lamellae which exhibit a true twin, 180° orientation relationship.

Thus, on the basis of these two analyses it is evident that both the Schmid factor and the geometric compatibility play an important role in the activation of the deformation systems in the fine lamellar structures.

Finally, particular mechanism for the transfer of twinning between adjacent grains is shown in Figure 4.37, which gives two examples of the so-called cross-twinning process.[1] In Fig 4.37(a), a micrograph is shown of lamella B (Figure 4.18) which contains a fine lamella with the same orientation as lamella A. It was shown that these two lamellae are related by a rotation of 180° about the $[\bar{1}\bar{1}1]$ - thus, the true twin orientation. This micrograph demonstrates that there exists a one-to-one correspondence of twins on each side of the thin lamellae. A higher magnification view of the boxed region in Fig 4.37(b) reveals that deformation twins are also present in the fine lamella and that they correspond one-to-one with the twins in lamella B. The twinning plane in each lamella has been determined to be $(\bar{1}11)$. This means that twinning occurs in each lamellae on the same plane, and that these two planes are rotated with respect to one another by 180° due to the given orientation relationship. Similarly, the same $1/6[1\bar{1}2]$ partial dislocation is responsible for twinning in each grain, although the true spatial directions of these Burgers vectors is different relative to one another due to the rotation. It should be noted that significant pile-ups are not observed at the interfaces and this seems to indicate that the transfer process between lamellae is rather favorable. A second example of this cross-twinning is shown in Fig 4.37(c) which shows an area containing five lamellae which are all related by consecutive 180° rotations about $[\bar{1}\bar{1}1]$. Analogous to the previous example, twinning on the $(\bar{1}11)$ plane is seen to occur in each of the lamellae and that these twins propagate across the lamellae in an exact correspondence.

Due to the apparent ease of this transfer process, the geometry has been examined in more detail in the stereographic projection shown in Figure 4.38. The trace of the lamellar interface $(\bar{1}\bar{1}1)$ and trace of the twin plane in the initial lamella have been indicated in the projection. In order to locate the trace of the twin plane in the rotated lamella, the $(\bar{1}11)$ twinning system in this adjacent lamellae is transformed to a twinning system on the $(1\bar{5}\bar{1})$ plane in the $[\bar{7}\bar{1}\bar{2}]$ direction in the initial lamella coordinate system. It is immediately evident that the common direction of intersection of the two twin planes is the [101] direction and that this direction is contained in the lamellar boundary. Further analysis of the cross-twinning process will be given in the discussion along with a proposed model which indicates the relative importance of this process.

---

[1] The term cross-twinning was first introduced by Lipsitt [25] to describe the propagation of twins to another plane of the same family when the twin intersects another twin of the same kind. This process was initially noted only over a narrow temperature range.

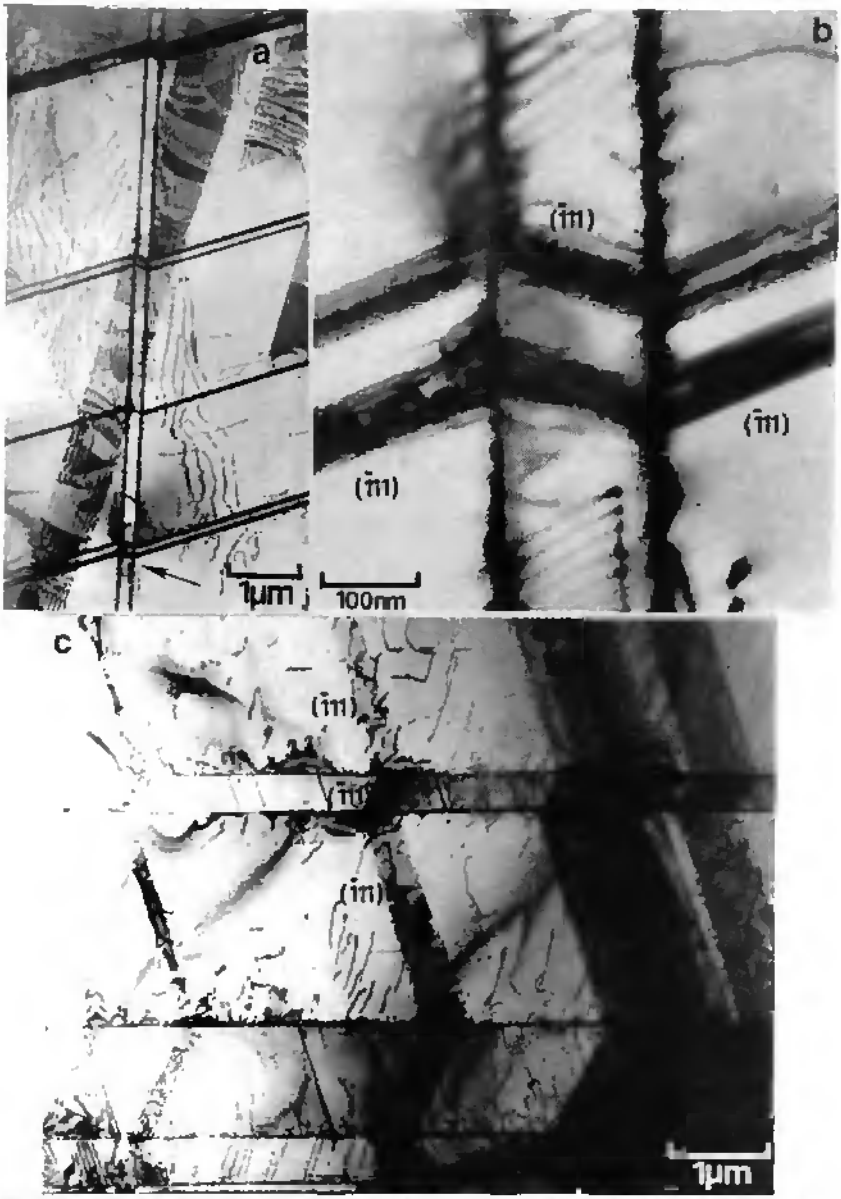

Figure 4.31 : (a) Overview and (b) higher magnification micrographs of the cross-twinning process in lamella B (Fig 4.18). (c) Cross-twins propagate continuously across a series of 180°, true-twin related lamellae.

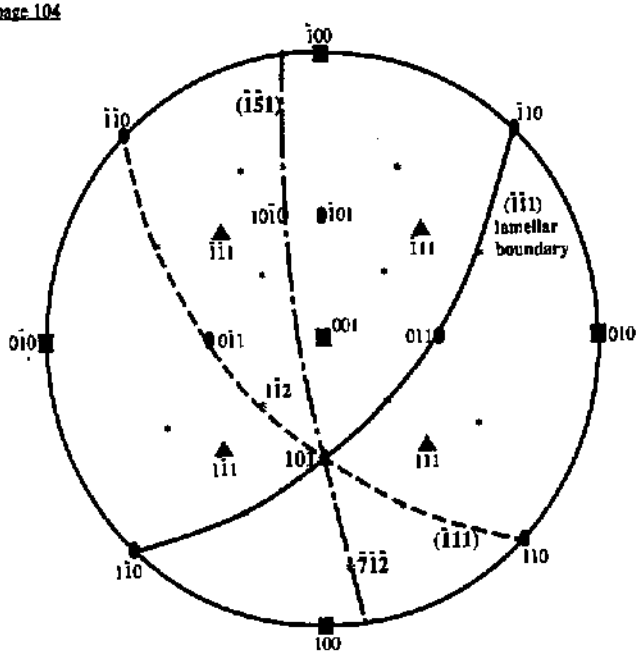

Figure 4.38 : Geometry of the cross-twinning process for (1̄11) twins as shown in Fig 4.37.

4.3.3 Summary

A summary of the geometric compatibility factors for both microstructures is given in Table 4.13. Determination of the compatibility for the fine lamellar structures is straightforward since only one mechanism is usually active in each lamella. However, the situation is less easily defined in the coarse and equiaxed structures since several mechanisms are active in each grain. In this case, the compatibility factors were maximized for each deformation mechanism.

In general, the following observations can be made:

1.) the orientation relationship of 120° rotations tends to yield higher compatibility between slip systems in adjacent grains. Several observations of perfect correspondence (m' = 1.0) have been made and the factors are generally 0.87 or 1.0. In contrast, the rotation relationships of 60° and 180° tend to give much lower values.

2.) the microstructure influences the number and distribution of the types of boundaries present. Furthermore, the 180° relationship exhibits a different behavior in the two microstructures. For the equiaxed structure, perfect correspondence of slip systems may be observed for the case when deformation occurs on the plane of rotation in both equiaxed grains. This is not possible in the lamellar structure.

120° Rotation Equiaxed

System I	m	System II	m	m'
5E ⇒ 5F				
1/6[112](1̄1̄1)	.47	1/2[110](1̄1̄1)	.47/.22	.87
1/6[1̄12](1̄1̄1)	.46	1/2[11$\bar{0}$](111)	.49/.19	.87
7D ⇒ 7E				
1/6[112](1̄1̄1)	.02	1/2[11$\bar{0}$](1̄1̄1)	.06	.87

120° Rotation Lamellar

System I	m	System II	m	m'
1B ⇒ 1F				
1/6[1̄1̄2](111)	.46	1/2[110](1̄11)	.31	.87
1/6[11̄2](1̄11)	.45	[10$\bar{1}$](1$\bar{1}$1)	.47	.87
1A ⇒ 1E				
1/6[11̄2](1̄11)	.26	[10$\bar{1}$](1$\bar{1}$1)	.38	.87
2B ⇒ 2D				
[011](1̄1̄1)	.49	1/2[1$\bar{1}$0](111)	.49/.14	1.0
1/6[112](1̄1̄1)	.42	1/2[1$\bar{1}$0](111)	.49/.14	.87
1/6[1̄1̄2](111)	.30	1/2[110](1̄11)	.41/.22	.87
10E ⇒ 10D				
1/6[1$\bar{1}$2](1̄11)	.08	1/2[1$\bar{1}$0](111)	.28	.87
1/6[1̄1̄2](1̄11)	.08	1/6[112](1̄1̄1)	.35	.06
4B ⇒ 4A				
1/6[1̄12](1$\bar{1}$1)	.50	[101](1̄11)	.45	.87
2A ⇒ 2C				
[011](1̄1̄1)	.38	1/2[1$\bar{1}$0](111)	.37	1.0
[10$\bar{1}$](111)	.34	[101](1̄1̄1)	.33	1.0
		[101](1̄11)	.24	.33

Table 4.13 : Summary of the influence of microstructure and orientation relationship on the observed geometric compatibility factors.

60 ° Rotation Equiaxed

System I	m	System II	m	m'
5E ⇒ 5A				
1/6[$\bar{1}$12](1$\bar{1}$1)	.46	1/6[$\bar{1}$12](1$\bar{1}$1)	.34	.53
1/6[112]($\bar{1}\bar{1}$1)	.47	1/2[110](1$\bar{1}$1)	.32	.67

180 ° Rotation Equiaxed

8E ⇒ 8F				
1/6[112]($\bar{1}\bar{1}$1)	.39	1/2[112]($\bar{1}\bar{1}$1)	.34	1.0
1/2[1$\bar{1}$0]($\bar{1}\bar{1}$1)	.32	1/2[1$\bar{1}$0]($\bar{1}\bar{1}$1)	.42/.34	1.0
[011]($\bar{1}\bar{1}$1)	.45	1/2[112]($\bar{1}\bar{1}$1)	.39	.87
5A ⇒ 5F				
1/6(1$\bar{1}$2]($\bar{1}$11)	.29	1/2[1$\bar{1}$0](111)	.49/.19	.19

180 ° Rotation Lamellar

System I	m	System II	m	m'
1B ⇒ 1A				
1/6[1$\bar{1}$2]($\bar{1}$11)	.45	1/6(1$\bar{1}$2]($\bar{1}$11)	.26	.43
1/6[$\bar{1}\bar{1}$2](111)	.46	1/2[110](1$\bar{1}$1)	.23	.54
2C ⇒ 2D				
(10$\bar{1}$](111)	.34	1/2[110]($\bar{1}$11)	.41/.22	.46
1/6[$\bar{1}\bar{1}$2](111)	.18	1/2[110]($\bar{1}$11)	.41/.22	.54
1/2[1$\bar{1}$0](111)	.37	1/2(1$\bar{1}$0](111)	.49/.14	.78
3D ⇒ 3C				
1/6[1$\bar{1}$2]($\bar{1}$11)	.30	1/2[110]($\bar{1}$11)	.31	.60
1/6[$\bar{1}$12](1$\bar{1}$1)	.24	1/2[110](1$\bar{1}$1)	.18	.60
1/2[110]($\bar{1}$11)	.35	1/6[1$\bar{1}$2]($\bar{1}$11)	.40	.60
10B ⇒ 10C				
1/2[1$\bar{1}$0](111)	.44	1/2[1$\bar{1}$0](111)	.28	.78
1F ⇒ 1E				
[10$\bar{1}$](1$\bar{1}$1)	.47	[10$\bar{1}$](1$\bar{1}$1)	.38	.78
1/6[1$\bar{1}$2]($\bar{1}$11)	.30	1/2[1$\bar{1}$0]($\bar{1}\bar{1}$1)	.28/.15	.32

Table 4.13 cont.: Summary of the influence of microstructure and orientation relationship on the observed geometric compatibility factors.

5. Discussion and Interpretation of Results

Various criteria are applied in an attempt to predict the ductility of a material. Two of the best known of these are the Rice-Thomson model [131] which evaluates the ability of a material to nucleate dislocations at a crack tip in order to blunt an atomistically sharp crack and the von Mises criterion which requires that five independent slip systems must be available for homogeneous deformation to occur in a polycrystalline material [112]. With regard to the latter demand, sufficient slip systems exist in TiAl such that these polycrystalline requirements should be met. It has been shown that both 1/2<110] ordinary dislocations and <101] superdislocations are active in the current alloy and these alone are known to provide five independent slip systems [132]. Further slip in the <112] directions in the form of twinning or 1/2<112] superdislocations provides additional degrees of freedom in fulfilling the required compatible deformation within each grain.

According to the Rice-Thomson model, dislocation emission under the stress concentration at a crack tip will be favorable as long as the following conditions are meet :

$$\frac{G\ b}{\gamma_s} < 7.5 - 10.0 \qquad 5.1)$$

where γ_s is the true surface energy, G the shear modulus and b the length of the Burgers vector. Taking typical values for TiAl, this parameter ranges from 3.5 to 8.5 depending upon the specific dislocation burgers vector and the crack plane (since the surface energy varies slightly with plane) which are used. Hence, for all but the least favorable situation (i.e. <101] superdislocations required to blunt a crack on the (100) plane), the Rice-Thomson criterion for a ductile material is fulfilled. Hence, the obvious question remains. Why is the ductility of TiAl limited to only several percent tensile elongation prior to failure?

Clearly, the above two criteria do not consider all the factors which influence the ductility of intermetallic alloys. In fact, Rice and Thomson were correct to point out that this approximation can be modified by variations in the core size of the dislocation and other geometric considerations. You and Fu [133] also showed that elastic anisotropy plays a crucial role in the dislocation mobility at a crack tip and will modify the ductile / brittle behavior of intermetallic alloys. Recently, the causes of embrittlement of intermetallic phases were reviewed and a number of intrinsic and extrinsic factors causing embrittlement were shown to occur such as difficult nucleation of dislocations, reduced dislocation glide, restricted planar glide, inhibited slip transmittal, impurities and environmental embrittlement [10]. A number of these factors have been shown to be important for TiAl such as embrittlement by interstitial oxygen [29,108] and environmental embrittlement [134-135]. While a great number of studies are being devoted to these factors and the general glide characteristics of individual dislocations, relatively less is known about the "macroscopic" behavior of dislocations

including the role of each mechanism in the deformation process, the influence of microstructure on the activation of deformation mechanisms and the importance of the orientation relationships on the transmission of slip between adjacent grains. The goal of this discussion will be to try to answer a number of questions which will, hopefully, shed further light on the aspects which control the ductility of two-phase TiAl alloys.

5.1 What is the Influence of Loading Orientation on the Deformation Mechanisms ?

Even in a polycrystalline material, it is reasonable to assume that the direction of compressive loading will play an important role in the activation of the deformation mechanisms. While multiple slip systems are expected to be activated at the grain boundaries in order to accommodate the localized stress concentrations due to elastic and plastic incompatibility between adjacent grains, this stress concentration will decrease with increasing distance from the grain boundary. Therefore, only the resolved shear stresses due to the applied load will be significant in the interior of the grain. Obviously, whether grain boundary or applied shear stress effects dominate the deformation behavior will depend sensitively on the grain size.

The influence of loading direction on the deformation behavior of single-phase TiAl has been previously discussed by several authors. In the first comprehensive work on the plastic deformation of TiAl, Shechtman et. al. [22] calculated equi-Schmid factor lines and concluded that inhomogeneous plastic deformation would result from differing abilities of the individual grains to activate the "easy" ordinary dislocation systems. However, no direct experimental observations were given to support this idea. A tensile / compressive asymmetry of the twinning process was indirectly supported by the observation of no more than two systems at a time within a single grain deformed in tension [25]. In the only single-crystal work to date on TiAl, Kawabata was able to directly verify the activity of the various systems as a function of applied loading orientation. These observations corresponded with the calculated Schmid factors in that <101] superdislocations were active for loading parallel to [001] and [$\bar{1}$10], while ordinary dislocations were observed for the loading orientations near [011]. However, it was also shown that Schmids law did not strictly apply since variations in the critical resolved shear stress were observed for different orientations. Unfortunately, no systematic attention was paid to twinning since it was only observed at 673°K. These twins were only observed for the [001] and the near [011] orientations (for compressive loading). Finally, single-crystal deformation behavior was approximated by performing in-situ observations on thin foils [33]. At room temperature, twinning was found to be active for orientations near [1$\bar{1}$0], superdislocations tended to be active near [001] and ordinary dislocations were found in all orientations except those which were closest to [001].

The current results compare favorably with [33] in that ordinary dislocations were identified in most grains regardless of orientation. However, the observations of twinning are inverted relative to the current observations due to the difference in the direction of the applied stress as explained later. The observations in [26] for twinning near [001] is also consistent with the current results. Therefore, it can be concluded that the present results correspond well with previous studies and the influence of loading orientation is the same in both single-phase and two-phase alloys.

The influence of loading orientation on the current material has already been presented in Figures 4.17 and 4.26 and is very generally summarized again in Table 5.1.

Deformation Mode	Orientations Active	Minimum m
1/2<110] ordinary dislocations	all	≥ 0.25
1/6<112] {111} twinning	near [001]	≥ 0.25
<101] superdislocations	near (001)	≥ 0.35
1/2<112] superdislocations	near (001)	various
faulted dipoles	near <111>	---

Table 5.1 : Influence of loading orientation on the active deformation mechanisms and the estimated minimum Schmid factor, m, required for activation.

The value of the minimum Schmid factor is only intended to be interpreted in a very general way and a more precise determination is limited due to the approximations encountered in using a polycrystalline material. However, it is useful to establish such minimum values to construct equi-Schmid factor diagrams which indicate the orientations where the stress should be sufficient to produce an observable dislocation density. The differences in the minimum Schmid factors of the various systems can be attributed to both the ease of nucleation (i.e. the elastic energy) and mobility of the dislocations (i.e. the core structure). On one hand, the lower elastic energy of the ordinary dislocations and twinning partials would indicate that these are easier to nucleate. On the other hand, the differences can also be linked to the mobility of the dislocations which, in turn, depends on the dislocation core structure. A narrow core on the slip plane, extensive core spreading out of the slip plane and the tendency to form locked configurations will all reduce dislocation mobility. Furthermore, the Peierls lattice resistance has also been shown to depend upon crystallographic direction due to covalent-like bonding between aluminum and titanium layers, as well as within the titanium layers [29,43,136]. Therefore, based upon these simple arguments of elastic energy and core structure, ordinary dislocations and twinning would be expected to be the more common modes of deformation. It must again be emphasized that these are only estimated values and are not meant to indicate a precise value of the critical resolved shear stress for the systems.

Using these minimum Schmid factors, it is possible to construct equi-Schmid factor diagrams which indicate the deformation mechanisms that could be expected to be active for any given loading

orientation. For construction of this map, an average value of m ≥ 0.30 was taken to be an approximate value for slip along the <112] directions. The distinction is not yet made between 1/6<112] twinning partial dislocation and the 1/2<112] superdislocation. This point will be discussed below. In Fig 5.1(a), it can be seen that at least one ordinary dislocation system fulfills the minimum Schmid factor for most orientations. Only near [001] loading orientations and <110] loading orientations should ordinary dislocations be difficult to activate. While no ordinary dislocations were observed for the two orientations closest to [001], the only grain examined near <110] was seen to deform extensively by two ordinary dislocation systems. This apparent inconsistency could likely be attributed to two effects. Firstly, since this <110] oriented grain was only about 4μm wide and sandwiched between two coarse α_2, the stress distribution within the grain may be more complex than the simple applied stress would imply. Moreover, for the [001] oriented grains, four twinning systems were active which is presumed to be sufficient for the required deformation and ordinary dislocations are not required. In contrast, for the <110] orientation a mixture of several superdislocation systems was identified. The presumed low mobility of these superdislocations may be insufficient for deformation in this region and, thus, the ordinary dislocation must be activated to satisfy the necessary deformation.

In Fig 5.1(b), it can be seen that <101] superdislocations could be expected for loading directions nearly parallel to [001] or parallel to the (001) plane. However, <101] superdislocations were, in fact, only observed for the loading orientations nearly parallel to the (001). As previously stated, several <101] superdislocation systems are highly stressed for the [001] orientations, yet only twinning is observed. Since twinning partial dislocations may be more easily nucleated than superdislocations due to their reduced elastic energy, they would then be the preferred deformation mode. *Secondly, it could also be considered that <101] superdislocations are, in fact, nucleated* but, instantaneous to the nucleation process, they could undergo a core transformation that emits partial twinning dislocations according to :

$$<101] \Rightarrow 1/6<211] + CSF + 1/6<112] + APB + 1/6<211] + SISF + 1/6<112] \qquad I.3)$$

Thus, a superdislocation could evolve into a pole source of twinning dislocations pinned by the other immobile reaction products. This type of mechanism was, in fact, predicted by Yoo and Fu [133] and this decomposition may be aided due to torque effects among the reaction products. However, it must be noted that this dissociation has never been observed. In any case, it can be concluded that the equi-Schmid lines correctly predicts the activation of superdislocations for loading directions near (001). However, for loading near [001], superdislocations are not observed despite the large resolved shear stress on superdislocation slip systems and this can be attributed to a preferential nucleation of twins.

Finally, in Fig 5.1(c) the equi-Schmid calculations for slip along <112] with m ≥ 0.30 are shown. It can be seen that these lines predict slip along the <112] directions for orientations centered around

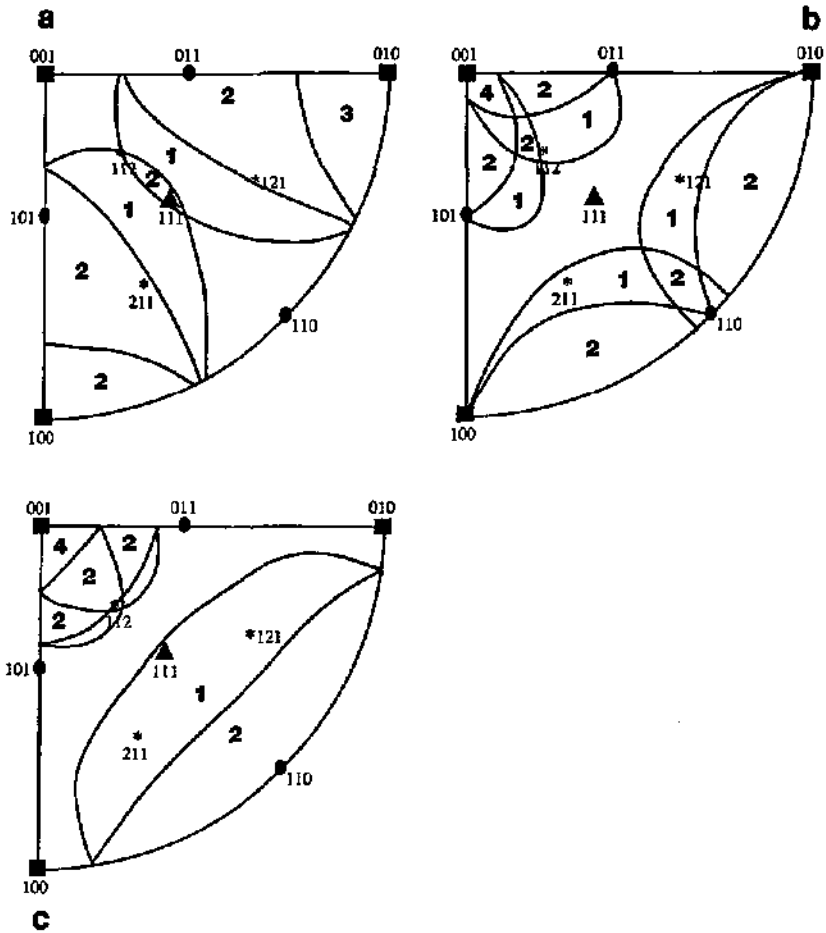

Figure 5.1 : Equi-Schmid factor lines for (a) m > 0.25 for 1/2<110] ordinary dislocations, (b) m > 0.35 for <101] superdislocations and (c) m > 0.30 for slip in <112] directions. The number within the surface indicates the number of slip systems of this type that fulfill the minimum criterion.

[001] and for zones which radiate out from <110]. This correctly predicts the occurrence of twinning with 1/6<112] partial dislocations for the orientations near [001]. For the zone around <110], this also approximately predicts the occurrence of the 1/2<112] superdislocations. The factors influencing the appearance of twinning or 1/2<112] superdislocations will be discussed subsequently.

Hence, this diagram correctly predicts in a qualitative manner the observed deformation behavior when the appropriate exception is taken that twinning is more favorable than glide of <101] superdislocations. It should also be noted from a superposition of the diagrams that, in comparison with fcc crystals, the region surrounding the <111> loading orientation is a zone with few possible slip systems. Stated differently, for <111> loading, the Schmid factor tends to be low for all possible slip systems such that deformation can be difficult for this orientation. Clearly, deformation in these orientations could be restrained and this will be the subject of further discussion.

It is appropriate to now ask the question, why is twinning favored for some orientations, while in other orientations glide of 1/2<112] superdislocations is observed? To answer this question, it is necessary to examine the polarity of the twinning process. In contrast to glide dislocations which can move in either direction depending upon the sense of the applied shear, twinning partial dislocations are restricted to motion in a single direction in order to create the required atomic displacements necessary for the twin stacking arrangement. This process is readily visualized with the aid of Figure 5.2 which shows these atomic displacements. It can be seen that passage of a single Shockley partial dislocation changes the ABCABC stacking sequence of the {111} planes to ABC / BCA BCA where the / indicates the plane on which the partial dislocation has passed. If a second partial dislocation passes on the plane immediately above the initial plane, the stacking sequence becomes ABC / BA B CAB. Thus, it is apparent that the ABCBA stacking sequence of a twin can be created by the passage of Shockley partial dislocations on successive {111} planes. The atomic arrangement has now been changed above the twin plane from the original arrangement indicated by the open circles in Figure 5.2 to the arrangement of atoms indicated by the full circles. Now, if this process is repeated by moving the partial dislocation in the opposite sense (i.e. right to left in the figure), the ABCABC stacking sequence is transformed to ABC / CAB. This CC stacking is a high energy configuration and clearly not favorable. Although a partial dislocation with twice the length (i.e. a 2x1/6<112] = 1/3<112]) could be moved in this opposite direction to achieve the required atomic displacements for creation of a twin, the large energy barrier at the CC saddle point would still need to be overcome. On the basis of this simple atomistic model, the polarity of the twinning process can be understood and it is apparent that twinning dislocations can only be the positive sense Burgers vector (and not the negative). This phenomenon has been verified in single-crystal experiments and is expected to be applicable for polycrystals as well.

The importance of this polarity on the deformation process was first identified by Schmid [137] who noted that twinning will always result in a specific shape change of the crystal. Since this shape change is geometrically fixed, there are loading orientations where the shape change imposed by the applied force violates the shape change that would be created by twinning and, thus, twinning is "forbidden" for these orientations. Based upon this restriction, Schmid stated the simple law that twinning results in extension for all the loading directions contained in the obtuse angle between the twin plane, K1, and the original position of the second invariant plane, K2, while compression occurs

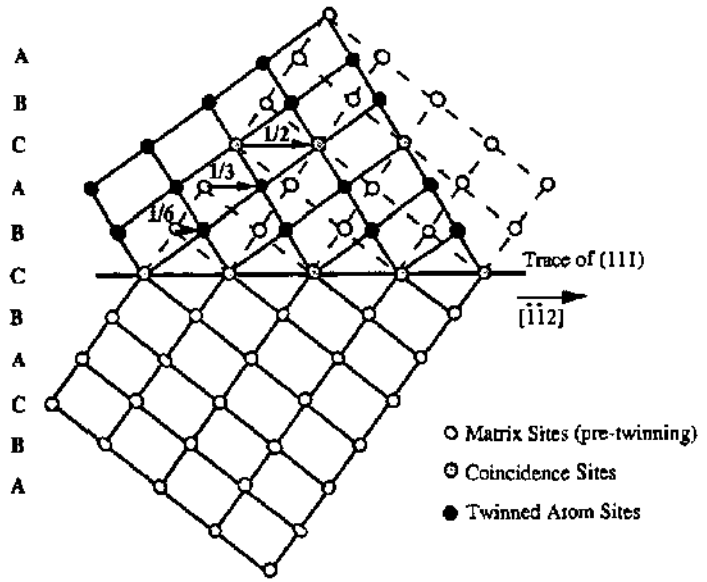

Figure 5.2 : Projection of the $(\bar{1}10)$ plane showing the atomic displacements created by the movement of $1/6[\bar{1}\bar{1}2]$ partial dislocations of successive (111) planes to form a twin.

for orientations within the acute angle of these planes.[1] This law was based on the assumption that the twin occupies the entire volume of the material. However, for situations where only a limited volume of the crystal twins (which is the actual physical situation more frequently encountered), then the extension / compression criterion of Schmid must be extended [130]. For conditions of incomplete twinning, the plane defined by the pole of the shear direction, $\eta 1$, replaces the K2 plane in the rule originally stated by Schmid. Accounting for these modifications, the influence of loading direction can be represented in the stereographic projection in Figure 5.3. The regions hatched indicate where twinning is favorable in compression, while the open areas indicate that twinning would be "forbidden" in compression. It must be noted that the areas favorable for twinning in compression overlap such that all four systems are possible near [001].

Figure 5.3 thus aids in understanding why twinning is experimentally observed for the loading orientations centered about the {001} direction. For these orientations, both the geometric polarity condition as well as the resolved shear stress requirements are fulfilled. Although orientations where twinning is favorable in compression extend as far away from [001] as out to the <110} orientation, the Schmid factor for these twin systems is very low away from {001}. Similarly, Fig 5.1(c) shows

[1] for a definition of the twinning elements K1 and K2 see, for example, ref. [129,138]

that highly stressed <112] systems do occur for the orientations radiating out from <110], but the geometric considerations indicate that these twinning systems would result in extension. Therefore, for these loading orientations, slip in the <112] direction must proceed by the passage of full 1/2<112] superdislocations rather than the twinning partials.

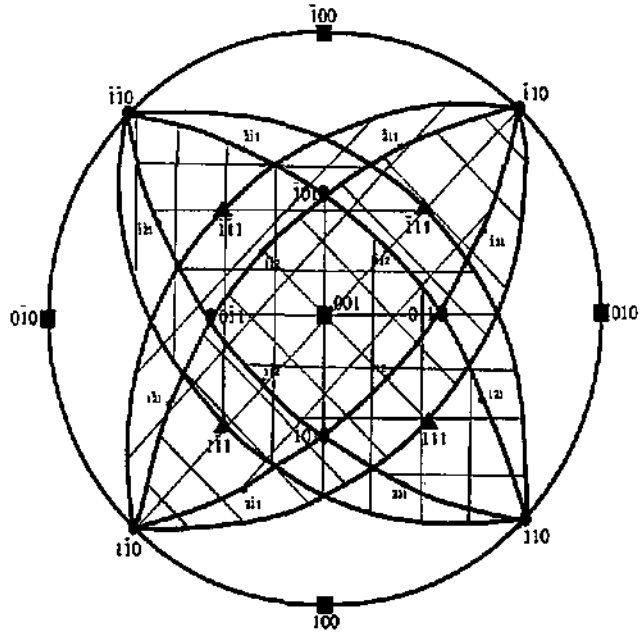

Figure 5.3 : Shaded regions indicate where 1/6<112] twinning is favorable in compression.

It should be mentioned at this point that twinning is often prevalent under conditions of low dislocation mobility such as low temperature deformation [139]. Thus, twinning is generally undesirable in materials and is frequently linked with brittle behavior. Yet, an apparent paradox is encountered in TiAl since alloying additions are desirable which decrease the stacking fault energy and, thus, promote twinning in order to improve the ductility. The observation that twinning is preferred over the glide of <101] superdislocations indirectly verifies the low mobility of the superdislocations. Thus, in the absence of twinning, the low mobility of the superdislocations limits the ductility of the alloy. However, activation of twinning provides some additional ability to deform. Nonetheless, twinning is still not a favorable mode of deformation since large stresses are required to nucleate the twin, large stress concentrations are created at the terminating end and the strain accomplished by twinning is small. Thus, even with twinning active, the tensile ductility of the alloys is still limited to 2-3%. One approach to improving the ductility is, thus, to minimize the stress concentration at the end of the twin and in a subsequent section this topic will be addressed.

Obviously, increasing the mobility of the superdislocations through appropriate alloying additions would also improve the ductility.

Finally, it is appropriate to speculate on why the faulted dipoles show a greater tendency to form for loading orientations near <111>. It could be envisioned that the orientation of the applied load could be important, for instance, in assisting the core transformation which leads to the dipole formation itself. For instance, it has been well established that the orientation of the applied stress is important in the formation of blocked dislocations in the $L1_2$ structure [140-143]. Thus, it is possible to imagine that the applied stress could favor or inhibit the transformations responsible for dipole formation. For instance, the current model to account for the formation of the dipoles assumes that cross-slip of a 1/2<101] superpartial dislocation on an octahedral plane is a necessary step in the formation process and that this cross-slip direction subsequently defines the direction of the fault [20]. It is possible to extend this model to allow for the cross-slip of this superpartial on the cube plane which is driven by a reduced APB energy on the cube plane [19,31,42,43] and, possibly, the applied load. In order to see if this assumption is plausible, the Schmid factor for the cross-slip of the appropriate superpartial onto a cube plane has been calculated. For all of the observed dipoles, $m > 0.45$, and this would indicate that the applied shear stress may act to aid the cross-slip of the superpartial dislocation if the Hug model is extended to include cross-slip onto the cube planes.

Moreover, it was also observed that the Schmid factor for the 1/2<112] superdislocation associated with the faulted dipoles was frequently rather low. Several dislocation reactions have been observed that could account for the formation of these dislocations. Therefore, the observed dislocations could be the immobile reaction product of a dislocation decomposition rather than being direcly nucleated during the deformation process. Similar conclusions have been drawn by both Farenc [33] and Greenberg [37]. For instance, the following two decompositions have both been observed in TiAl [20,37,144-145] and could account for the formation of these 1/2<112] superdislocations:

$$1/2\langle 110] + \langle 101] \Rightarrow 1/2\langle 112] \qquad 1.8)$$

$$\langle 101] \Rightarrow 1/2\langle 110] + 1/2\langle 112] \qquad 1.7)$$

Tentative evidence for the decomposition given in equation 1.7 is shown in Figure 4.15. However, only limited observations of these reactions were performed such that it is inappropriate to attribute the formation of the dislocations associated with a low Schmid factor to either of these reactions. Clearly, more detailed analysis would be necessary to verify which if these decompositions are indeed responsible for the 1/2<112] superdislocations with a low Schmid factor. Similarly, the suggestion that cross-slip of the superpartial onto a cube plane is important during the dipole formation must also be experimentally confirmed.

In conclusion, it has been shown that the deformation mechanisms in both microstructures depend upon the orientation of the grain with respect to the loading orientation. In general, this orientation

dependence can be explained by resolved shear stress calculations shown in Fig 5.1. Due to the ordered $L1_0$ structure, this orientation dependence results in asymmetric deformation behavior. Ordinary dislocations and twinning are clearly the preferred deformation modes. It was also shown that twinning is preferred over <101] superdislocations and the polarity of the twinning process can be used to explain why twinning is active only for limited orientations. Finally, the significance of this analysis on deformation studies should be clear. Attempts to correlate deformation mechanisms with temperature, composition, microstructure, etc. can only be made after a sufficient number of grains have been investigated. Conclusions drawn on limited analysis can be inappropriate due to the influence of loading orientation on the activation of the various deformation mechanisms.

5.2 Does the Microstructural Distribution Influence the Mechanisms of Plastic Deformation ?

By comparison of the results presented in Sections 4.1 and 4.2, it is clear that a number of differences exist in the deformation behavior of the equiaxed and lamellar microstructures. These differences will be defined below and rationalizations for these differences will be proposed. The expected influence of these differences on the ductility of the materials will also be treated.

One obvious influence of microstructure is the role played by the γ grain size or lamellar thickness on the number of deformation systems activated within the grain. In the equiaxed grains and the coarse lamellae ($\geq 1\mu m$), two or more deformation systems were active throughout the grain. In contrast, only one primary deformation system was identified in the fine lamellae below $1\mu m$ thick. This restriction of the deformation to a single primary system will most likely restrict the ductility of the material for two reasons. Firstly, unless the slip systems in adjacent grains are fully compatible, incompatibility stresses will be created at the interface. Without a second slip system to accommodate or minimize these stresses, fracture will ensue at the interface. This effect is treated in more detail in Section 5.4. Secondly, operation of one system will necessarily limit the total amount of strain that can be realized by the grain.

Similarly, it was shown that the equiaxed microstructure readily undergoes localized deformation in regions of presumed stress concentration. This was seen at grain boundaries as well as in the vicinity of large α_2 particles. In contrast, deformation was seen to proceed rather homogeneously along the length of the lamellae in the lamellar structure. This seems to indicate a difficulty in locally activating deformation mechanisms in response to stress concentrations at the various interfaces. Instead of plastic flow in response to the stress concentration, interfacial decohesion or cleavage fracture can occur and, thus, limit the ductility of the alloy.

One exception to this homogeneity of deformation within the lamellar structures was identified in the vicinity of a grain boundary as shown in Figure 4.27. In this lamella, deformation systems were

identified in response to both the applied load, as well as, to presumed stress concentrations at the boundary. Therefore, it appears that only at the grain boundaries of the lamellar colonies does the stress distribution become favorable for the activation of plastic flow in response to a localized stress concentration. In this context, it was noted in Section 1.4.4 that several investigations have found an increase in ductility with decreasing grain sizes. It is generally accepted that reduced grain sizes will result in a more homogeneous distribution of stresses within a material [146-147]. Due to this more homogeneous stress distribution, there will exist more opportunities to activate grain boundary sources. Thus, it it is readily predicted that the contribution of localized deformation systems to the total plastic deformation increases as the grain size decreases. For the one particular case examined, propagation of the localized twinning system was seen to end at approximately 15μm into the lamella. Based on this observation, it could be anticipated that the optimum colony size would be approximately 30μm. However, it must be noted that this optimum size has been estimated for only one specific stress distribution and this size may decrease as smaller grained materials would be examined. Therefore, the current observations form a basis for interpreting the observed influence of grain size on the ductility of TiAl alloys. Notwithstanding these colony size effects, the ductility of the lamellar structure appears to be limited by its inability to locally deform in response to stress concentrations at the interfaces within the structure. This is not the case for the equiaxed microstructure.

The frequency of twinning in the two microstructures also appears to be different. Since twins were identified in 12 of the 15 equiaxed grains examined, and the fact that twins were frequently observed in the equiaxed microstructure in the as-heat treated condition, it seems that the stress distribution in this structure is favorable for the nucleation of twins. In contrast, the lamellar structure contained virtually no twins in the as-heat treated condition and showed a lower propensity for twinning in the deformed materials. Two factors are proposed for this behavior. Since it is known that significant localized stresses are necessary for nucleation of twins, the specific stress distributions in the two microstructures can be used to explain the occurrence of twinning. In the case of the equiaxed grains, large localized stresses are likely to be formed at the irregular grain boundaries under conditions which are favorable for twin nucleation. By favorable, it is implied that components of the stress field *normal to the boundary are necessary to produce a twin at some defined angle to this boundary.* In contrast, more regular stress concentrations are expected in the lamellar structures and these concentrations are less likely to nucleate a twin since the normal component of the stress field may be reduced. In the lamellar structure, twins appear to be created only when the conditions of the applied load are such that the entire length of the lamellae is subjected to a sufficient shear stress and twins are then nucleated homogeneously along the length of the lamellae at interfacial misfit dislocations [73]. By limiting the nucleation of twins to these conditions, the lamellar structure is restricted in its ability to deform by twinning.

A second explanation for more frequent observation of twinning in the equiaxed microstructure could be related to a localized twinning which may result in macroscopic extension. Since the shape change accomplished by twinning is fixed, geometric conditions indicate that twinning will result in either extension or compression of a grain. The large grain size of the lamellar structure indicates that, during compression testing, all grains must undergo compressive deformation and twinning which would result in extension of a single grain is prohibited. These conclusions are supported by the experimental observations. However, due to the smaller grain size of the equiaxed structure, it can be envisioned that some grains *could* undergo extension even though the imposed macroscopic shape change of the sample requires compression. It is envisioned that a small volume of twinning which results in extension of a single grain in response to localized stress concentrations would not disturb the macroscopic compression of the sample. Thus, the strict polarity conditions for the twinning process could be locally relaxed in the equiaxed microstructure. Tentative experimental evidence for twinning in "violation" of the established polarity conditions may be observed, for example, in grain 6E (for both systems) of Table 4.5. It was previously suggested that this twinning is due to the fact that this area is rather thin and sandwiched between two large, elongated α_2 particles which subsequently alters the stress distribution in this area and imposes additional shape changes on the grain. Under these conditions, twinning which results in extension of the grain and contradicts the macroscopic compressive shape change may be locally favored. Unfortunately, it is impossible to verify whether these twins were created during the deformation process or were residual twins present after the heat treatment. Therefore, it is impossible to establish without doubt that local relaxation of the polarity law has occurred. However, based on the above arguments, it is reasonable to suggest that local "violations" of the polarity of the twinning process may occur in the fine, equiaxed microstructure, while it would be less likely in the coarse lamellar grains.

The shape and distribution of the α_2 phase also assumes a critical role in the deformation process. In the equiaxed microstructure, the coarse particles play only a minor role in the deformation behavior of the material. The large spacing between particles indicates that Orowan strengthening is negligible. Hence, these particles only locally modify the stress distributions in the γ phase and act as coarse barriers to dislocation motion. In contrast, it could be expected that the α_2 phase plays a decisive role in the deformation characteristics of the lamellar structure. It is expected that the α_2 phase will influence the deformation in the γ phase by :

1.) altering the stress state due to both elastic and plastic incompatibilities,

2.) impeding the flow of dislocations and reducing the effective slip length. The efficiency of impeding this slip transfer across the lamellae will depend on the exact geometry of the slip systems involved and the thickness of the α_2 lamellae.

It was shown by experiments on oriented lamellar colonies [11,104-105] that the orientation of the lamellar colony with respect to the loading axis greatly influences the mechanical properties. This was

believed to be due to the influence of orientation on the activation of the hard (across the lamellae) or easy (parallel to the interface) deformation modes. However, it was recently found that this dependence is more appropriately attributed to the deformation characteristics of the α_2 phase itself [49]. This role of the α_2 phase is shown in Fig 5.4 where it is observed that the increase in yield strength of the lamellar structure is directly related to the yield strength in the α_2 phase. Hence, the deformability of the individual α_2 lamellae could influence the overall behavior of the structure. Further significance of the deformability of the α_2 phase will be discussed in Section 5.1.4.

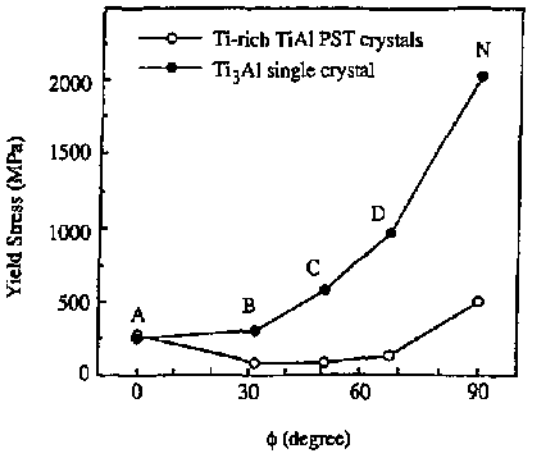

Figure 5.4 : Influence of loading orientation on the room temperature yield strength of oriented colonies of lamellar TiAl / Ti_3Al (PST) in comparison to Ti_3Al single crystals. From [49].

At this point, it is relevant to pose the question why the <101] superdislocations appeared to become more favorable in the deformation of the fine lamellae? In Fig 4.35, a fine lamella was shown to contain <101] superdislocations, even though the resolved shear stress on an ordinary dislocation system was nearly equal to the superdislocation system. It was previously concluded that the ordinary dislocations would be the preferred mode in the equiaxed and coarse lamellar microstructures. However, in the fine lamellae, the superdislocation mode was preferentially activated. Assuming that this observation corresponds with the active mechanisms during deformation (i.e. assuming that it is not true that ordinary dislocations were responsible for the deformation, but that they are then readily absorbed by the interfaces and, thus, were not observed in post-mortem examination), then there must be additional forces in the fine lamellae which have not been previously identified.

It may be possible that the ease of dislocation nucleation is the factor which determines the active deformation system in the fine lamellae. For instance, ledges of defined character at the interfaces may be more favorable to the emission of one type of dislocation than another. While the details of such a ledge mechanism have not been investigated, the notion is possible that the preferential nucleation of a certain type of dislocation could be related to the specific geometry of the boundary.

Additionally, it could be imagined that the nucleation process is aided by dislocation reactions between the dislocations which arrive at the interface from an adjacent grain and any interfacial dislocations which are present. For the situation shown in Fig 4.35, it is possible that the 1/6[$\bar{1}$12] partials in the adjacent lamella B could react with interfacial dislocations to form the [101] superdislocations in lamella A. Making use of the known 120° [$\bar{1}\bar{1}$1] rotation between these two grains, the Burgers vector of the twinning partial in lamella B is transformed to the coordinates system of lamellae A as:

$$1/6[\bar{1}12]_B \overset{120°}{\Rightarrow} 1/6[\bar{2}\bar{1}\bar{1}]_A \qquad 5.2)$$

Subsequently, in order to create a [101] superdislocation with this incoming partial dislocation, the following reaction would be required at the interface:

$$2x\ 1/6[\bar{2}\bar{1}\bar{1}] + 2x\ 1/6[\bar{1}12] \Rightarrow [\bar{1}0\bar{1}] \qquad 5.3)$$

However, it is clear that the required 1/6[$\bar{1}\bar{1}$2] will not be present in the ($\bar{1}\bar{1}$1) interfacial plane. Based upon similar calculations, no plausible reactions were found which would involve the expected interfacial dislocations and the incoming twin partial dislocations which would give a probable slip system in lamella A. Therefore, it is concluded that dislocation reactions involving interfacial dislocations and dislocations which intersect the interface do not assist in the nucleation of dislocations in the adjacent grain.

Furthermore, it is known that dislocation image forces may play an important role in the deformation behavior of nanoscale microstructures [148-149]. Based upon calculations of the forces required to activate Frank-Read dislocation sources and the image forces in multilayer structures, it was found that a critical thickness, t_c, was found below which operation of the Frank-Read source is suppressed [150]. This equation for t_c is given as:

$$t_c < \frac{32\ \pi\ b}{R} \qquad 5.4)$$

where $R = (G_1 - G_2) / (G_1 + G_2)$ and G_i is the shear modulus of layer i. It is possible that image forces are important in the current lamellar arrangement by favoring nucleation of dislocations with the appropriate Burgers vectors. Therefore, the influence of these image forces in the deformation mechanisms in fine lamellae has been estimated using equation 5.5 [149].

$$F = \frac{R\ G\ b^2}{4\ \pi\ r} \qquad 5.5)$$

where R is defined above, r is the distance of the dislocation from the interface, F is the image force on the dislocation and G and b shear modulus and Burgers vector, respectively. This gives the force due to the nearest image. Calculations of the magnitude of this image force for various dislocations using calculated elastic constants and simplified assumptions of the influence of anisotropic elasticity

have indicated that these forces are rather small. On this basis, it is necessary to presume that the image forces will not play an important role in the nucleation process. However, these simplified calculations cannot rule out the possibility that more detailed considerations of the elastic anisotropy would identify a larger effect of the image forces.

It should again be noted that deformation tended to proceed in the hard mode (i.e. across the lamellae) for all lamellar orientations. This is in contrast to the expectations outlined in [11] which predict deformation parallel to the lamellar interface (i.e. the easy mode) for loading orientations near 45°. The lack of deformation parallel to the interface could be due to insufficient dislocation sources. While the lamellar boundary provides sufficient sources of deformation across the lamellae in the hard mode, only the grain boundaries appear to be useful for initiating slip parallel to the interface. It is possible to speculate that the domain boundaries which occur within a single lamella could also provide nucleation sites for deformation parallel to the interface. However, the evidence presented here does not support this speculation. As such, the only way to increase the activity of the easy mode of deformation is to decrease the grain size as discussed previously.

Finally, although not the focus of this work, it is possible to comment on the configurations of the individual dislocations that have been observed. Since directional bonding effects have been reported to occur in TiAl alloys, it is possible to compare the observed dislocation line directions with the predicted bonding effects. Greenberg first proposed that directional bonding would result in deep Peierls valley for defined crystallographic directions [40] and these predictions have since been confirmed using more sophisticated methods [43]. If large Peierls valleys do influence dislocation mobility, then it would be expected that the dislocations would be frequently observed to lie along these directions. In Table 5.2, the experimentally observed line directions are compared with these Peierls valley calculations.

Dislocation	Observed Line Direction (° from screw orientation)	Predicted Peierls Pinning Effect
1/2<110] ordinary dislocation	strong tendency 0°	large
<101] superdislocation	strong tendency 0°	none
1/2<112] superdislocation	weak tendency 30° or 90°	none, large
1/6<112] twinning partial	strong tendency 0-30°	moderate to none

Table 5.2 : Observed line directions compared to the predicted Peierls valley effects.

Interpretation of these line directions is based on the assumption that the observed directions correspond to the dislocation segments that are blocked or exhibit low mobility and are, therefore, most commonly observed in the thin foil specimen. The higher mobility segments of the dislocation loops are assumed to have been absorbed by the free surfaces (i.e. grain boundaries) during deformation. It can be seen from the table that the observed preference of the ordinary dislocations for

the screw orientation may be attributed to a Peierls blocking effect. However, the ordinary dislocations are generally curved in nature and are not perfectly straight as would be expected if such a blocking mechanism would be active. Furthermore, the observation of dislocations lying along the screw orientation must be regarded with due caution since line energy effects would also favor the creation of dislocation segments in specific orientations. For instance, on the basis of elastic isotropy, the screw orientation would be expected to be the low energy orientation and this may explain the tendency for the ordinary dislocations to align along screw orientations. Although detailed elastic anisotropy calculations have not been performed for TiAl, calculations on other intermetallic phases [151] have shown that anisotropy effects will have a strong influence on the lowest energy orientation and the screw orientation may not necessarily be the lowest energy. Similarly, there is also a strong tendency for the <101] superdislocations to be aligned in straight segments along the screw direction, though this configuration is not predicted by the Peierls valley calculations as listed above. Therefore, the tendency to observe screw <101] superdislocations must be due to other locking mechanisms originating from, for example, non-planar core configurations or transformations, which leave the dislocations locked in this orientation. Evidence of the possibility of a core dissociation not contained in the primary glide plane is shown in Figure 4.14. Finally, the line direction of the 1/2<112] superdislocations or twinning partial dislocation does not seem to be influenced by a Peierls effect.

5.3 How do the γ / γ Orientation Relationships Influence Deformation ?

In light of the compatibility requirements outlined in Section 1.5.2, it is necessary to know how the specific orientation relationships in TiAl may effect deformation and to define the role of microstructure in this process. Recall that it has been shown that the orientation relationship between the adjacent γ grains in both microstructures can be described by multiples of a 60° rotation about a <111> direction. Through knowledge of the exact spatial relationship between grains and the subsequent application of the geometric compatibility factor defined in Section 1.5.2, it has been shown that the specific orientation relationship does indeed influence the deformation process (Section 4.3). The significance of the orientation relationship is that it geometrically defines the relative alignment of slip systems in adjacent grains.

In summary, the results in Section 4.3 showed that :

1.) the geometric compatibility factor could be applied in the equiaxed microstructure to predict the activation of the slip systems at the grain boundary or at a pile-up.

2.) the geometric compatibility factor plays an important role in the activation of the deformation modes in the fine lamellar structures.

3.) in general, the orientation relationship defined by a 120° type rotation provides the best compatibility between slip systems in adjacent grains.

In order to fully understand the influence of these orientations relationships, it is useful to look at the geometry of intersecting slip systems at the grain boundary as shown in Figure 5.5. In this diagram, a {111} slip plane in the initial grain I is shown intersecting the boundary plane between an adjacent grain II. For both the 60° pseudo-twin and 180° true-twin relationships, the angles formed at this boundary between the slip plane in I and the possible {111} slip planes in II are $\phi = 39°, 56°$ or 71° as shown. In addition, if the deformation in grain I occurs on the {111} plane used to define the plane of rotation, then obviously this plane will be parallel to the same plane in grain II (while the other three {111} planes all intersect this plane of rotation to form 71° angles). Although it was shown in Section 4.2 that deformation parallel to the interfacial plane is rare for the lamellar structures, it is readily possible in the equiaxed microstructure. Therefore, $\phi = 0°$ has also been indicated in the diagram for the equiaxed structure only. Since both the 60° and 180° orientation relationships lead to similar geometric situations, it is expected that the behavior of these boundaries would generally be the same.

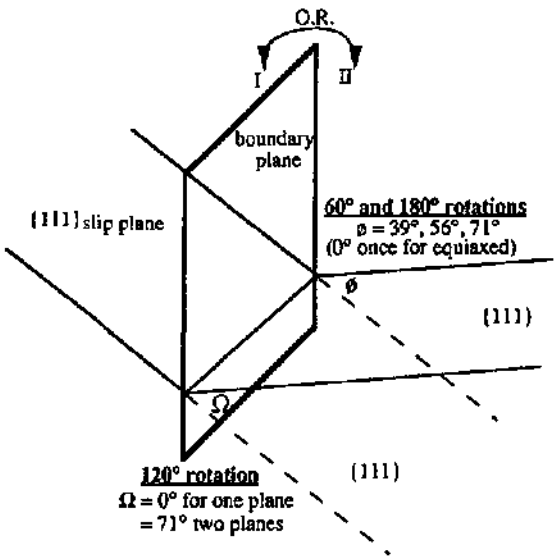

Figure 5.5 : Influence of the rotation between adjacent grains I and II on the geometry of the intersection of possible slip planes in each grain.

Now, if the geometry of the slip plane intersections at the grain boundary is examined for the 120° rotation, a completely different geometric situation can be identified. For a {111} slip plane defined in grain I, one possible slip system in grain II will form a 0° angle with this original plane, while the other two {111} planes will form a 71° angle. Thus, for any {111} slip plane in grain I there exists a

{111} glide plane in grain II which corresponds exactly to the original slip plane. The same geometry applies for the {111} plane which defines the plane of rotation. Straight away, it can thus be envisioned that deformation on {111} in grain I could be transmitted directly to the corresponding {111} plane in grain II (i.e. $\Omega = 0°$) with relatively little resistance. In this case, the transfer mechanisms would then depend upon the specific Burgers vector of the slip systems involved.

The importance of the direction of the Burgers vectors involved in the transfer process can be understood in a general way by applying the specific rotations on a <111> projection as discussed in Appendix 9.1 or using the matrix transformations defined in Section 2.3.3. For both the 60° and 180° rotations, neither the <110> nor the <112] slip directions in I will correspond to a possible slip direction in grain II. Again, the notable expectations to this are the directions which lie in the {111} used to define the orientation relationship in which case the directions in each grain do correspond. However, there will, in general, be no correspondence between slip directions in grains I and II for the 60° and 180° rotations.

Again, this behavior directly contrasts the geometric situation for the 120° rotation. Since the 120° type rotation is equally defined by a 90° rotation about <100> such that the cube axes in each crystal are parallel, one could expect a correspondence between slip directions in each grain. Calculations show that this is indeed the case since each <110> slip direction in grain I will be parallel to a <110> direction in grain II. Although the <112> directions are also parallel in each grain, the $L1_0$ ordering imposes restrictions on the possible slip directions such that slip is only possible in the <112] direction. Hence, <112] in grain I will be parallel to a <211} direction in the related grain, but this <211] is not a possible slip direction. Thus, although there is an exact correspondence between all <110> slip directions in the two grains, this is not the case for the <112] directions.

With this physical picture in mind, it is possible to calculate the maximum geometric compatibility factor for each slip system and for the three types of orientation relationships - 60°, 120° and 180°. Listed in Table 5.3 are all of the possible slip systems in the initial grain I and the largest compatibility factor, m', which would be possible for a slip system in the adjacent grain II. Also given in the table is the type of slip system which corresponds to this maximum value. In relevant cases, only a <112] direction is indicated since either twinning or 1/2<112] superdislocations would be appropriate depending upon the exact conditions regarding the polarity of twinning as discussed in Section 5.1.1. From Table 5.3, it can be concluded that the slip systems in adjacent grains related by a 120° rotation can result in better compatibility than either the 60° or 180° rotations. The exceptions to this are the slip systems contained in the {111} plane of rotation, in which case the geometric compatibility factors are either 0.87 or 1.00 for all rotations. It is, hence, possible to hypothesize that the transfer of slip between adjacent grains will be the easiest for a 120° rotation due to the good geometric alignment of slip systems. In contrast, transfer of slip across grain boundaries between grains related by 60° and 180° rotations would be expected to be more difficult due to the lower geometric compatibility.

Slip System I		Maximum Compatibility Factor in II		
b	(hkl)	60°	120°	180°
110	$\bar{1}11$	0.65 O	1.00 S	0.65 S
110	$1\bar{1}1$	0.65 S	1.00 S	0.65 S
$1\bar{1}0$	111	0.78 S	1.00 S	0.78 O
$1\bar{1}0$	$\bar{1}\bar{1}1$	1.00 S	1.00 S	1.00 O
112	$\bar{1}\bar{1}1$	0.87 S	0.87 O	1.00 112
$\bar{1}12$	$1\bar{1}1$	0.67 O	0.87 O	0.67 S
$1\bar{1}2$	$\bar{1}11$	0.73 112	0.87 O	0.67 S
$\bar{1}\bar{1}2$	111	0.54 S	0.87 O	0.60 112
101	$\bar{1}11$	0.78 S	1.00 O	0.78 S
101	$\bar{1}\bar{1}1$	1.00 S	1.00 O	1.00 S
$10\bar{1}$	111	0.65 O	1.00 O	0.65 S
$10\bar{1}$	$1\bar{1}1$	0.65 S	1.00 O	0.65 O
011	$1\bar{1}1$	0.78 O	1.00 S	0.78 S
011	$\bar{1}\bar{1}1$	1.00 O	1.00 S	1.00 S
$01\bar{1}$	111	0.65 S	1.00 S	0.65 S
$01\bar{1}$	$\bar{1}11$	0.65 S	1.00 S	0.65 O

Table 5.3 : Influence of orientation relationship on the maximum compatibility factor for rotations about $[\bar{1}\bar{1}1]$. Type of slip system which gives this compatibility : S <101] superdislocation system, O an ordinary 1/2<110] dislocation system and 112 slip or twinning in a <112] direction.

The compatibility factor can also be used to understand the activation of slip systems at the grain boundary in response to a pile-up of dislocations in a neighboring grain as shown in Section 4.3. Although this problem is central to the understanding of grain size strengthening, there exists relatively little understanding in the exact mechanisms controlling this effect. In a famous series of papers, Stroh [152-154] addressed a related problem and calculated that the plane experiencing the maximum normal stress would be found at an angle of 70.5° to the original slip plane. While this calculation is useful in understanding the fracture behavior at a pile-up, it gives no information regarding the activation of the possible slip systems due to the shear stresses which are present. Stroh gives the shear stress a distance r from the head of the pile-up as:

$$\tau = \tau_s \times \left(\frac{L}{r}\right)^{1/2} \qquad 5.6)$$

where L is the length of the dislocation pile-up and τ_s is the applied shear stress (resolved on the appropriate slip system). However, this equation also depends upon an orientation factor and doesn't indicate the direction of this shear stress. Hence, it is limited in its ability to be used to predict the activation of the possible slip systems. Shen [119] also showed that it is possible to calculate the full

stress field associated with the pile-up in order to predict the slip systems in adjacent grains. However, this calculation is necessarily complex and must be computed in full for each different situation (including the influence of the line direction of the dislocations, the nature of the grain boundary and the anisotropic elastic constants).

Therefore, it is interesting to note in this context that the compatibility factor was able to provide information regarding the activation of deformation in adjacent grains. In considering only the geometric compatibility of the slip systems in the two grains, the complex mathematics involved in calculating the exact stress distribution have been avoided. This simplification is necessary in the case of, for example, a twin since the pile-up of twinning partial dislocations occurs on consecutive {111} planes and the Eshelby solution to the stress concentration at the pile-up only applies if the pile-up occurs on a single {111} plane. Additionally, the exact stress distribution at the head of the pile-up is expected to be a complex function of the character of the dislocation and this introduces further difficulties in finding an exact mathematical solution. Therefore, any mathematical solution will be limited for only the exact conditions upon which it was defined. In contrast, it is imagined that because the concept of this geometric compatibility is so general, it would apply for all dislocation characters, for the twinning process and in other physical situations or in other materials.

Additionally, it was shown that the geometric compatibility of slip systems appears to play an important role in the selection of the single deformation mode which is activated in adjacent fine γ lamellae. In order to visualize the significance of the compatibility factor in these lamellae, it is possible to refer to the concept of "geometrically necessary dislocations" as first postulated by Cottrell and developed into a complete theory by the works of Ashby [155]. Accordingly, the density of geometrically necessary dislocations in a material can be directly related to the strain gradients which arise due to different deformation behaviors in adjacent phases or grains. This density of *geometrically necessary dislocations*, ρ^G, *is given by:*

$$\rho^G = \frac{4\,\gamma}{\lambda_G\, b} \qquad 5.7)$$

where γ is the shear strain and λ_G is the geometric slip distance. For a polycrystal, λ_G is given by the grain size, while this distance is defined as the spacing between the lamellae for lamellar microstructures. There will always exist a competition during the deformation process between ρ^G and ρ^S, the density of randomly stored "statistical" dislocations. However, for geometric slip distances less than approximately 2μm, it has been shown that the geometrically necessary contribution should dominate the total dislocation density [155].

Since the thickness of the fine lamellae in the lamellar microstructures is below this approximate limit, it is expected that geometrically necessary dislocations would dominate the total dislocation density in the fine lamellae. The actual physical situation of deformation in the fine lamellae varies from the

model proposed by Ashby since the model was derived by assuming that the bonding between the lamellae is such that dislocations are not absorbed at the interface, that sliding does not occur at the interface and that the second phase does not deform. Although these conditions are probably relaxed for the lamellar structure of TiAl and Ti_3Al, the general considerations of the geometrically necessary model still apply - dislocations must be generated in order to maintain a *compatible* shape change between adjacent lamellae and this effect becomes more important with *decreasing* lamellar thickness.

The results in Section 4.3 demonstrate that both the Schmid factor and geometric compatibility factor are important in activation of the deformation systems for lamellae less than 1μm thick. Apparently, the choice of deformation system must simultaneously maximize conformity to the shape change required by the imposed stress (i.e. the Schmid factor) and the shape change required to maintain compatibility with the adjacent grain (i.e. the geometric compatibility factor). The influence of these two factors can be described by representing the stress state in the grain as :

$$\tau_{total} = \tau_{applied} + \tau_{adjacent} \qquad 5.8)$$

where $\tau_{applied}$ is the stress due to the applied load and $\tau_{adjacent}$ the stress due to the shape changes occuring in the adjacent grain. In this way, the activation of the deformation system in the adjacent lamellae will be influenced by both the external loading and the local compatibility requirements. Detailed calculations regarding values for $\tau_{adjacent}$ were not attempted. However, it is expected that these are in the same order of magnitude as the $\tau_{applied}$ since both factors have been shown to be important in the activation of the deformation systems.

Finally, it is necessary to consider some of the limitations in applying this type of calculation. Obviously, the ability of the boundary to deform will influence the applicability of the compatibility factor. This may be especially important in the lamellar structures where the interface is defined by a {111} plane which has been shown to contain glissile dislocations [71,77,156]. Therefore, deformation along the interface could accommodate differences in the deformation systems. This type of effect is demonstrated in the analysis presented by Lim [157]. A residual slip vector was defined as the difference in the Burgers vectors in adjacent grains and it was postulated that this parameter must be minimized by the deformation systems in adjacent grains. Mobility of this residual slip vector in the interface plane would enhance the deformation of the two grains through increased compatibility of the deformation. In contrast, immobile residual vectors will accumulate at the interface and eventually lead to crack formation and failure. Obviously, minimization of the size of these residual slip vectors is important in reducing stress concentrations at the interface and this is achieved only if the geometric compatibility factor is maximized.

Another important factor which is not taken into account in the proposed geometric compatibility analysis is the additive properties of the deformation systems. An assumption which has indirectly

been made is that the deformation systems in adjacent grains can be compared on a one-to-one basis. However, it is plausible that even though the compatibility of a slip system in grain I, S_I, is low with respect to two individual systems A, S_{IIA}, and B, S_{IIB}, in grain II, the geometric compatibility of the deformation systems in these grains could be sufficient according to a simple addition of the strains in grain II:

$$S_{IIA} + S_{IIB} \Rightarrow S_I \qquad 5.9)$$

Thus, the grain boundary coherency conditions defined in equation 1.16 may also be satisfied by the cumulative strains of two or more slip systems. This possibility has not been taken into account during the current analysis. The fact that the fine lamellae deform principally by a single deformation mechanism removes this concern, while in the case of localized activation of deformation systems at the grain boundary this possibility also does not appear to play a major role. In contrast, some of the compatibility factors given previously in Table 4.13 could be limited by this effect. It was stated that these values represent the maximization of the compatibility between individual mechanisms and, as such, do not take into account the possibilities illuminated by equation 5.9.

Notwithstanding these limitations, it has been demonstrated that the compatibility factor can be useful in predicting the activation of deformation systems at the grain boundary in the equiaxed microstructure and that it plays an important role in the activation of deformation systems in the lamellar microstructures. Also, it has been reasoned on a geometric basis and verified experimentally that the deformation systems in grains related by a 120° rotation will exhibit higher geometric compatibility.

On the basis of these conclusions, it is possible to identify additional influences of the microstructure on the deformation process.

1.) on average, the equiaxed microstructure will contain more 120° type boundaries than the lamellar structure (where the 180° rotation is the most common).

2.) in the equiaxed microstructure, deformation is possible on the {111} plane used to define the orientation relationship and, in this case, there exist slip systems in the adjacent grain which result in high compatibility for all orientation relationships. In contrast, deformation rarely occurs on the {111} planes parallel to the lamellar boundary and, thus, these high compatibility systems for the 60° and 180° rotations do not exist.

Taken together, these two factors would indicate that superior ductility should be obtained in equiaxed structures. Experimentally, this notion has been confirmed.

Finally, it is appropriate to comment on the cross-twinning process that was identified in Fig 4.37. In this context, *cross-twinning* refers to the transfer of twinning deformation between adjacent lamellae, whereby twinning occurs on the same {111} plane in each lamella and that the transfer occurs with apparently little resistance. Two cases of this process (observed only for 180° rotations) were identified and the relevant geometry of this transfer process was presented in Fig 4.38. Although it is also frequently presented in the literature [64,81,99] as a common transfer mechanism, little attention has been devoted to this process. Therefore, it is necessary to comment on the possible mechanisms involved in the process and its importance in the overall deformation behavior.

For the current alloy, this cross-twin process was identified only in the lamellar microstructure and only for true-twin, 180° oriented lamellae. In contrast, for the case of the 60° rotation (Fig 4.31), the large dislocation pile-ups at the boundary indicate that the favorable cross-twin transfer process was not activated. These differences between the 60° and 180° rotation could be due to 1.) nature of the boundary itself, 2.) presence, absence or density of misfit dislocations or 3.) the differing intersection geometries. With regard to the last point, the intersection of the twin planes in each lamella for the 180° rotation is a <101] direction contained in the boundary plane. However, this intersection was a <123> direction in the case of the 60° rotation examined (Fig 4.32). By assuming that cross-twinning is only possible for 180° rotations, that the geometric polarity requirements for twinning must be met for both lamellae and that the Schmid factor for each system must be sufficiently large, it is possible to predict the loading orientations where cross-twinning may be expected. For a $(\bar{1}\bar{1}1)$ boundary plane and cross-twinning on the $(\bar{1}11)$ planes, these requirements are fulfilled for the small region of loading orientations shown in the superimposed standard / twin projection in Figure 5.6. Also shown in the figure are the three experimental cases where $(\bar{1}11)$ twinning was observed in $(\bar{1}\bar{1}1)$ twin-related lamellae. These experimental observations verify the predictions since the two orientations where cross-twinning was observed lie within the stripped zone while the one where it was not observed lies outside the zone. Geometrically equivalent predicted favorable zones are obtained for $(1\bar{1}1)$ cross-twinning. However, there exists no favorable zone for (111) twinning. Hence, for deformation twinning, non-equivalent geometric situations control the ability of a specific twin system (i.e. (111) or $(1\bar{1}1)$ twinning) to transfer through twin-oriented γ lamellae. Similar considerations should also apply to the intersection of twins during deformation of equiaxed grains since the deformation twin which occurs first can be considered as a twin-oriented lamella that is present within the grain. Subsequently, a second twin which intersects this original twin will be able to transfer through this twin by cross-twinning only if the geometric and loading conditions of cross-twinning are fulfilled. Outside of these favorable cross-twin orientations, other mechanisms are expected to be activated to transfer deformation between intersecting twins [158]. It should also be noted that, although this cross-twin phenomenon is frequently proposed as an important mechanism of deformation transfer in the lamellar structures, the process is, in fact, restricted to be active for only particular loading orientations. Therefore, its overall importance in slip transfer between adjacent

lamellae is limited. More work is necessary to properly define the specific mechanisms which occur at the boundary.

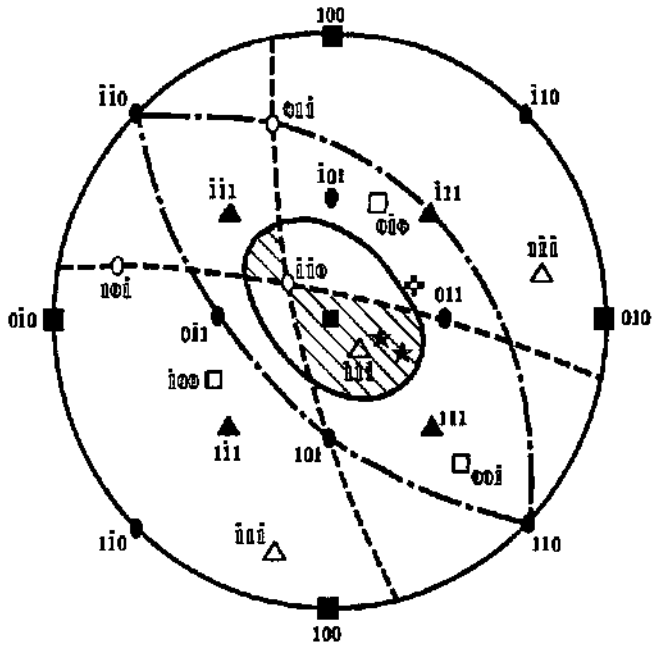

Figure 5.6 : Standard stereographic projection (solid symbols) overlapped with a projection of a $(\bar{1}\bar{1}1)$ twin-related crystal (open symbols with zone axes indicated in shadowed characters). The stripped area shows the loading orientations where $(\bar{1}11)$ cross-twinning between $(\bar{1}\bar{1}1)$ twin related lamellae is expected to be possible. ★ and ✣ represent orientations where cross-twinning was experimentally observed and not observed, respectively.

5.4 Does the α_2 / γ Orientation Relationship Influence the Transmission of Slip ?

In general, the α_2 phase deforms rather less than the γ phase. Nevertheless, the plastic properties of the α_2 phase may be crucial to the deformability of the lamellar structure as shown in Figure 5.4. Increased ductility in this phase could certainly increase ductility of the lamellar structure by reducing the density of geometrically necessary dislocations required in the γ phase and by reducing interfacial stress concentrations. Although only limited examination of this phase has been carried out in the current work, some important conclusions can be drawn through application of the concepts of geometric compatibility that were discussed in the preceding section.

In Section 4.2.8, detailed examination of the deformation structures observed in a coarse α_2 lamella were presented. It was shown that two types of dislocations were found in this lamella - a low density of dislocations located in the interior of the lamella which were identified as $1/6[11\bar{2}0]$ $(\bar{1}100)$ dislocations and some loops or short segments which were localized only in the proximity of the interfacial regions. This second type of dislocations were shown to have a Burgers vector parallel to [0001] and geometrical considerations indicated that the slip plane could be $(\bar{1}100)$. In contrast to the interior slip system, the Schmid factor for this localized slip system could not be used to explain the activation of these dislocations.

Therefore, in an effort to understand the activation of this localized dislocation system, the geometric compatibility factors were calculated in relation to the deformation mechanisms in the surrounding γ phase - the twinning system $1/6[\bar{1}\bar{1}2]$ (111). Then using the definition of the orientation relationship between the γ and α_2 phases as $[\bar{2}110]_{\alpha_2} // [011]_{\gamma}$, the compatibility factor may be calculated in exactly the same manner as it was for the γ / γ relationships. The geometric compatibility factors for the possible slip systems in the α_2 are subsequently given in Table 5.4.

Slip Direction	Slip Plane	m'	Comments
[0001]	$(1\bar{1}00)$	0.88	maximum compatibility
$[\bar{1}2\bar{1}6]$	$(1\bar{2}11)$	0.84	---
$[\bar{2}116]$	$(2\bar{1}\bar{1}1)$	0.84	---
[0001]	$(2\bar{1}\bar{1}0)$	0.77	---
$[2\bar{1}\bar{1}0]$	$(01\bar{1}0)$	0.14	highest for a prismatic slip system
$[11\bar{2}0]$	$(\bar{1}100)$	0.00	observed in interior of the lamella

Table 5.4 : Geometric compatibility factors for possible slip systems in the α_2 lamella for twinning on the (111) plane in the adjacent γ lamellae.

The results shown in Table 5.4 are indeed provocative and may explain the appearance of the [0001] dislocations in the interfacial region. The compatibility factor shows that the $[11\bar{2}0]$ dislocations, while active within the lamella due to the applied shear stress, provide little compensation for the shape changes in the surrounding γ lamellae due to (111) twinning. However, it is striking that the [0001] $(1\bar{1}00)$ slip system would provide the maximum compatibility with the twinning in the γ lamellae. Therefore, it is suggested that these [0001] dislocations in the α_2 lamella are created due to the shape changes imposed by the (111) twinning and, as such, serve to accommodate the stresses created at the γ / α_2 interface.

The general observation that these dislocations are usually associated with the twins in γ supports this conclusion. However, the short distances that these dislocations propagate from the interface indicate that they have only a low mobility due to either a large CRSS or high elastic energy. Due to this limited mobility, they can only partially accomplish the imposed shape changes. Since the prismatic

<11$\bar{2}$0> dislocations appear to have higher mobility (since they are found in the interior of the grains), they would appear to be a more favorable system to activate in order to accommodate the stress concentrations. However, the geometric compatibilities for these <11$\bar{2}$0> slip systems are all rather low and, as indicated in the table, the maximum compatibility factor for a prismatic slip system is only m = 0.14. Thus, while the prismatic family of dislocations may be rather mobile, they do not *provide the required shape changes necessary to maintain compatibility with the adjacent γ lamellae.*

Since there are three possible twinning systems in the γ lamellae (excluding the {111} plane which is parallel to the interface), it is necessary to determine if all three possess equivalent geometric relationships with the possible deformation systems in α_2. Therefore, the geometric compatibilities have been calculated for the three twinning systems, assuming the same orientation relationship as above as summarized in Table 5.5.

(111) twinning	
[0001] (1$\bar{1}$00)	0.88
[$\bar{1}$2$\bar{1}$6] (1$\bar{2}$11)	0.84
[$\bar{2}$116] (2$\bar{1}\bar{1}$1)	0.84
[0001] (2$\bar{1}\bar{1}$0)	0.77
[2$\bar{1}\bar{1}$0] (01$\bar{1}$0)	0.14

(1$\bar{1}$1) twinning	
[$\bar{2}$110] (01$\bar{1}$1)	0.84
[$\bar{2}$110] (01$\bar{1}$0)	0.82
[1126] (11$\bar{2}$1)	0.63
[2$\bar{1}\bar{1}$0] (0$\bar{1}$11)	0.50

($\bar{1}$11) twinning	
[$\bar{1}$2$\bar{1}$0] ($\bar{1}$011)	0.84
[$\bar{1}$2$\bar{1}$0] ($\bar{1}$010)	0.82
[11$\bar{2}$6] ($\bar{1}\bar{1}$21)	0.63
[1$\bar{2}$10] (10$\bar{1}$1)	0.50

Table 5.5 : Maximum geometric compatibility factors for the possible slip systems in an α_2 lamella for the given twinning system in the adjacent γ lamellae using $[\bar{2}110]_{\alpha_2}//[011]_{\gamma}$ and $(0001)_{\alpha_2}//(\bar{1}\bar{1}1)_{\gamma}$.

It is readily seen that the (1$\bar{1}$1) and ($\bar{1}$11) twinning systems result in geometrically equivalent relationships with the possible slip systems in α_2 and that they exhibit different geometry than a (111) twin. Presuming that the <2$\bar{1}\bar{1}$0> {01$\bar{1}$0} prismatic slip systems are the most favorable systems in the α_2 phase, it is clear that the two geometric situations will vary in their ability to accommodate twinning in the adjacent γ lamellae. As previously shown for the (111) twinning, the maximum compatibility factor for a favorable prismatic slip system is only m' = 0.14. Hence, these favorable dislocations will not be able to accommodate the twinning in the adjacent γ lamellae and, as a result, unfavorable [0001] or <1216> pyramidal dislocations will be necessary. In contrast, for the other two twinning systems, there exists a prismatic <11$\bar{2}$0> system which gives a geometric compatibility of m' = 0.82 for the adjacent twinning. Due to this higher compatibility, glide of the prismatic dislocations will effectively be able to accommodate the adjacent twinning deformation and, therefore, reduce stress concentrations at the interface. Based on this analysis, fracture at the α_2 / γ interface is predicted to occur preferentially when (111) twinning is activated in the γ phase due to the low compatibility of this particular twin system with a favorable prismatic slip system in the α_2.

In order for this prediction to be valid, the assumption that the <2$\bar{1}\bar{1}$0> {01$\bar{1}$0} slip system is favorable should be addressed in more detail. The values for the critical resolved shear stress for

various slip systems in α_2 are given in Table 5.6. The value for the CRSS of the [0001] {1100} slip system was estimated by assuming that these slip systems were not active for any of the orientations investigated by Inui et. al. [49]. Hence, the *minimum* value can be approximated. However, this assumption must be made with proper caution since the active slip systems were determined by analysis of the slip traces on the surface. It would be possible that [0001] and <11$\bar{2}$0> slip are active on the same slip plane and would, thus, not be individually detected. The general appearance of the slip traces did not give any indication for this multiple slip. Moreover, [0001] dislocations are only rarely observed in Ti_3Al [46,50] and this tends to confirm the fact that the CRSS must be much higher than for <2$\bar{1}\bar{1}$0> {01$\bar{1}$0} slip. Thus, the value indicated in the table can be taken as a reasonable lower bound. Furthermore, it can be seen that the CRSS depends sensitively on the exact chemical composition. The values listed given in [49] should be most applicable in the current case since this hyperstoichiometric composition most closely approximates the composition of the α_2 lamellae in equilibrium with the TiAl lamellae. However, it is also noted that vanadium additions nearly double the CRSS for both the prism and pyramidal slip systems. Hence, it could be anticipated that Cr in the hyperstoichiometric α_2 would also increase these values to some degree. As such, the values given by Inui [49] can again be taken as lower bound for the CRSS in the current alloy. While the absolute value of these CRSS cannot be directly applied to the current alloy, the important conclusion remains. Namely, the CRSS for <2$\bar{1}\bar{1}$0> {01$\bar{1}$0} slip is much lower than for any of the other possible slip systems and would, thus, be the favored mode of deformation. Ward has also reported that <$\bar{1}\bar{1}$20> (1$\bar{1}$00) prismatic slip is the dominant slip system for various alloys [45] and this further confirms that this system is expected to be more favorable than the other possible slip systems.

Source	Alloy	<$\bar{1}\bar{1}$20> {$\bar{1}$100}	<11$\bar{2}$0> (0001)	<$\bar{1}\bar{1}$26> {11$\bar{2}$1}	{0001} [1$\bar{1}$00}
[49]	Ti-36.5Al	90-107	329	911	> 250
[48]	Ti-24.4Al	65	---	450	---
	Ti-29.4Al-2.3V	50-110		710	
[51]	Ti-25.1Al	≈ 65	---	≈ 470	---

Table 5.6 : Critical resolved shear stress, in MPa, for slip in single-crystal Ti_3Al.

These CRSS for slip in α_2 can be compared with the CRSS for slip in the γ phase given by Kawabata for single-crystal TiAl [26]. Depending on the exact orientation, values for 1/2<110] slip ranged from 83 to 97 MPa, while slip parallel to the <101] directions required 80 to 116 MPa. It is again expected that these values will vary strongly with the exact chemical composition and, thus, may not directly apply for the current alloys under investigation. Nonetheless, it is supposed that they give a reasonable order of magnitude approximation for the current two-phase alloy. Therefore, it could be expected that <2$\bar{1}\bar{1}$0> {01$\bar{1}$0} would glide under shear stresses which are similar to these necessary for glide of both dislocation systems in γ. In contrast, other slip systems in α_2 are expected to be mobile only under conditions of high stress concentration. If the CRSS for these systems is higher than the interfacial strength, then interfacial decohesion will occur prior to activation of the system.

It should be noted that this type of orientational dependence on the ability of slip to transfer between adjacent phases has been previously observed. In a similar study on pearlite [159], it was shown that the ability of twins to shear the cementite lamellae depended upon the interaction of the specific twinning system and the orientation relationship between the ferrite and cementite. Consequently, two twin systems in the ferrite were observed to transmit across the pearlite due to their alignment with possible slip planes in the cementite while the other two twins were unable to shear the cementite phase. The current work extends this notion by defining the geometrical compatibility factor which provides more information regarding the slip systems which are required to shear the second phase. Hence, this analysis provides a more detailed description of the transfer process and also gives guidelines on how to facilitate this transfer.

It is, therefore, possible to predict how the α_2 phase could be modified in order to achieve maximum ductility of lamellar alloys :

1.) the thickness of the α_2 lamellae should be strictly controlled since it was shown that the thickness has a significant influence on the transmission of slip systems across the lamellae. Although a precise value cannot be obtained from the current experiments, less than 50nm would appear to be an optimum thickness.

2.) due to geometric compatibility conditions imposed by the α_2 / γ orientation relationship, glide of unfavorable <1126> pyramidal dislocations or [0001] dislocations may be required to maintain compatibility with γ lamellae, depending upon the specific deformation mechanism. Therefore, the properties of these slip systems must be understood in more detail and alloying efforts to reduce the CRSS of these systems would be appropriate.

In conclusion, it has been demonstrated that the deformation behavior of lamellar structures depends not only on the γ phase, but also on the plastic behavior of the α_2 phase. Moreover, the geometric compatibility factor can be used to show that the geometric compatibility of slip systems between the two phase plays an important role in the deformation of the lamellar structures. Specifically, (111) twinning in the γ lamellae will always lead geometrically unfavorable situations with the α_2 lamellae such that glide of [0001] or <1216> dislocations will be required. Clearly more research on the behavior of these slip systems is required.

6. Conclusions

In order to examine the influence of microstructure and orientation relationships on the room temperature deformation behavior of two-phase TiAl alloys, the deformation mechanisms of a Ti-47.5Al-2.5Cr alloy, heat-treated in two distinct microstructural variants, have been identified using transmission electron microscopy. The two heat treatments were 1270°C/64h and 1000°C/168h and these resulted in either **a transformed lamellar** structure or an **equiaxed** microstructure, respectively. The transformed lamellar structure consisted of approximately 50% coarse γ lamellae and 50% regions of fine, alternating γ and α_2 lamellae. In contrast, the equiaxed structure consisted of 10% large α_2 particles in a fine-grained γ phase matrix. Based upon the detailed TEM analysis of the orientation relationships and deformation mechanisms of both alloys, the following conclusions can be drawn :

- ▲ It has previously been proposed that γ grains may assume a total of six different orientations such that a total of five orientation relationships may exist between adjacent grains. Although only four of these six orientations have previously been observed, a **consistent indexing method** developed here has been used to verify that a total of six distinct orientations does exist.

- ▲ Utilization of the consistent indexing method, which is achieved by describing the orientation of each grain as a multiple of a **60° rotation** about a **<111> axis**, enables the deformation mechanisms in each grain to be described in a spatially correct manner.

- ▲ Both the Schmid factor and a **geometric compatibility** factor influence the activation of the various deformation mechanisms within each grain. Introduced in this work, a geometric compatibility factor, m', is used to quantify the relative alignment of slip systems in adjacent grains and is calculated as the product of the cosines of the angles between the slip directions and the normal to the slip planes.

- ▲ Deformation twinning of the type **1/6<112]{111}** and glide of **1/2<110]** ordinary dislocations are the preferred deformation modes in the γ-TiAl phase. <101] and 1/2<112] super-dislocations are usually only present in grains where twinning and ordinary dislocations are not easily activated.

- ▲ **Asymmetric deformation behavior** creates grain to grain variation in the active deformation mechanisms and is due to the $L1_0$ ordering of the TiAl phase. Consequently, it is imperative to investigate a sufficient number of grains when attempting to identify the influence of, for example, temperature or alloying additions on the deformation behavior.

- Only deformation twinning of the type **1/6<112]{111}** is possible. This has been established by the correspondence of the twinning polarity criterion with the influence of the loading orientation and by direct analysis of the twinning partial dislocations.

- Application of the geometric compatibility factor was used to show that orientation relationships described by a **120°** rotation will provide the best compatibility between slip systems in adjacent grains. This was predicted theoretically and verified experimentally.

- It would be expected that the **equiaxed structure** should be more **ductile** than the lamellar structure based on the following:

  1.) in the lamellar structure, the majority of orientation relationships between γ lamellae are the 180° true-twin type, while the distribution of orientation relationships in the equiaxed structure is random. This means that more of the favorable 120° type will be present in the equiaxed structure.

  2.) deformation modes which are active on the {111} plane used to define the axis of rotation between grains can always result in a high geometric compatibility in slip systems. While this deformation mode is possible in the equiaxed structure, it is rare in the lamellar structure since deformation generally occurs by the hard mode - i.e. on slip planes inclined to the lamellar boundary.

  3.) deformation twinning and localized deformation mechanisms are more easily activated in the equiaxed microstructure.

- **Lamellar thickness** plays an important role in the deformation characteristics of the lamellar structures. For γ lamellae thicker than $\lesssim 1\mu m$, more deformation mechanisms may be active, while below this thickness only a single deformation mechanism is active. The thickness of the α_2 lamellae influences the ability of the deformation to shear across the lamellae.

- The α_2 particles in the equiaxed microstructure exert a negligible role during the deformation process. In contrast, α_2 **lamellae** limit the deformability of the lamellar structure by restricting the propagation of slip across the γ lamellae.

- The known effect of increasing ductility with decreasing **grain size** can be attributed to the activation of grain boundary sources. Grain boundaries are shown to be important since they provide sources for the easy mode of deformation - i.e. deformation parallel to the lamellar boundary.

- Limited observations of the deformation mechanisms in the α_2 lamellae indicate that the **orientation relationship between the α_2 and γ phases** also plays an important role in the deformation process. Depending upon the specific deformation mechanism in the surrounding γ lamellae, glide of unfavorable types of dislocations may be required in order to maintain compatibility at the lamellar interface. Therefore, the properties of these unfavorable slip systems should be examined in detail in order to improve the ductility of the lamellar structures.

- Deformation twinning may be transmitted between grains related by a 180°, true-twin rotation by a **cross-twinning** process which encounters little resistance to propagation across the grain boundary. While this process appears to be rather favorable, it is shown to be important for only a small region of loading directions and is, therefore, limited in its overall importance in the deformation process.

7. References

[1] Y-W. Kim, J Metals, (7), 1989, 24-30.

[2] D.M. Dimiduk and D.B. Miracle, in High-Temperature Ordered Intermetallic Alloys III, C.T. Liu, A.I. Taub, N.S. Stoloff and C.C. Koch (eds.), Vol. 133, Materials Research Society, 1989, 349-360.

[3] S. Naka, M. Thomas and T. Khan, in High Temperature Intermetallics, The Institute of Metals, 1991, 1-14.

[4] L. Singheiser and H.W. Grünling, ibid [3], 159-171.

[5] R.W. Cahn, MRS Bulletin, May 1991, 18-23.

[6] N.S. Stoloff and R.G. Davies, Prog Mater Sci, (13), 1966.

[7] D.M. Dimiduk, D.B. Miracle and C.H. Ward, Mat Sci Tech, (8), 1992, 367-375.

[8] H.A. Lipsitt, in High-Temperature Ordered Intermetallic Alloys, C.C. Koch, C.T. Liu and N.S. Stoloff (eds.), Vol. 39, Materials Research Society, 1985, 351-364.

[9] J.C. Chesnutt and J.C. Williams, Metals and Materials, August 1990, 509-511.

[10] I. Baker and E.P. George, Metals and Materials, 1992, 318-328.

[11] M. Yamaguchi, ibid [3], 15-29.

[12] Y. Nishiyama, T. Miyashita, S. Isobe and T. Noda, ibid [2], 557-584.

[13] J.W. Parten, ibid [2], 492-504.

[14] J.H. Westbrook, Mechanical Properties of Intermetallic Compounds, John Wiley & Sons, 1960.

[15] M. Yamaguchi and Y. Umakoshi, Prog Mater Sci, (34), 1990.

[16] R.L. Fleischer, D.S. Dimiduk and H.A. Lipsitt, Ann Rev Mater Sci, (19), 1989, 231-263.

[17] P. Duwez and J.L. Taylor, Trans AIME, (4), 1952, 70-71.

[18] J.B. McAndrew and H.D. Kessler, J Metals, (8), 1956, 1348.

[19] G. Hug, A. Loiseau and P. Veyssière, Phil Mag A, (57), 1988, 499-523.

[20] G. Hug, A. Loiseau and A. Lasalmonie, Phil Mag A, (54), 1986, 47-65.

[21] D.W. Pashley, J.L. Robertson and M.J. Stowell, Phil Mag A, (19), 1969, 83-98.

[22] D. Shechtman, M.J. Blackburn and H.A. Lipsitt, Met Trans A, (5), 1974, 1373-1381.

[23] G. Hug, DSc Thesis, Université de Paris Sud, Centre D'Orsay, 1988.

[24] S.H. Whang and Y.D. Hahn, Scripta Met, (24), 1990, 1679-1684.

[25] H.A. Lipsitt, D. Shechtman and R.E. Schfrik, Met Trans A, (6), 1975, 1991-1996.

[26] T. Kawabata, T. Kanai and O. Izumi, Acta Met, (33), 1985, 1355-1366.

[27] G. Hug and P. Veyssière, in Electron Microscopy in Plasticity and Fracture Research of Materials, U. Messerschmidt, F. Appel, J. Heydenreich and V. Schmidt (eds.), Akademie-Verlag, 1989, 451-458.

[28] E.L. Hall and S.C. Huang, J Mater Res, (4), 1989, 595-602.

[29] S.A. Court, V.K. Vasudevan and H.L. Fraser, Phil Mag A, (61), 1990, 141-158.

[30] V.K. Vasudevan, S.A. Court, P. Kurath and H.L. Fraser, Scripta Met, (23), 1989, 907-912.

[31] S.H. Whang, Y.D. Hahn, Z.X. Li and Z.C. Li, in Proceedings of International Symposium on Intermetallic Compounds, O. Izumi (Ed.), Japan Institute of Metals, 1991, 763-770.

[32] S.C. Huang and E.L. Hall, Met Trans A, (22), 1991, 427-439.

[33] S. Farenc, DSc Thesis, Université Paul Sabatier, No. 1131, 1992.

[34] S. Sriram, V.K. Vasudevan and D.M. Dimiduk, High-Temperature Ordered Intermetallic Alloys IV, L.A. Johnson, D.P. Pope and J.O. Stiegler (eds.), Vol. 213, Materials Research Society, 1991, 375-383.

[35] B.A. Greenberg, O.V. Antonova, V.N. Indenbaum, L.E. Karkina, A.B. Notkin, M.V. Ponomarev and L.V. Smirnov, Acta Met, (39), 1991, 243-254.

[36] K. Chaudhuri and S. Das, Phil Mag Let, (67), 1993, 143-150.

[37] B.A. Greenberg, O.V. Antonova, V.N. Indenbaum, L.E. Karkina, A.B. Notkin, M.V. Ponomarev and L.V. Smirnov, Acta Met, (39), 1991, 233-242.

[38] X. Qu, B. Huang, Y. Qian, X. Kong, H. Lu and P. Huang, ibid [31], 797-801.

[39] Bernard Viguier, private contact, EPFL, Lausanne, Switzerland, 1993.

[40] B.A. Greenberg, Phy Stat Sol B, (55), 1973, 59-67.

[41] T. Kawabata and O. Izumi, Scripta Met, (21), 1987, 435-440.

[42] Z.C. Li and S.H. Whang, Mat Sci Eng A, (152), 1992, 18-25.

[43] C. Woodward, J.M. MacLaren and S. Rao, J Mater Res, (7), 1992, 1735-1750.

[44] V. Vitek, in Dislocation Properties of Real Materials, The Institute of Metals, (1985), 30-50.

[45] C.H. Ward, Int Mat Rev, (38), 1993, 79-101.

[46] M. Thomas, A. Vassel and P. Veyssière, Scripta Met, (21), 1987, 501-506.

[47] S.A. Court, J.P.A. Löfvander, M.H. Loretto and H.L. Fraser, Phil Mag A, (61), 1991, 109-139.

[48] Y. Umakoshi, T. Nakano, T. Takenaka, K. Suminoto and T. Yamane, Acta Met, (41), 1993, 1149-1154.

[49] H. Inui, Y. Toda and M. Yamaguchi, Phil Mag A, (67), 1993, 1315-1332.

[50] S.A. Court, J.P.A. Löfvander, M.H. Loretto and H.L. Fraser, Phil Mag A, (59), 1989, 379-399.

[51] Y. Minonishi, Phil Mag A, (63), 1991, 1085-1093.

[52] W.J.S. Yang, Met Trans A, (15), 1982, 324-328.

[53] M.A. Morris and D.G. Morris, Phil Mag A, (63), 1991, 1175-1194.

[54] Y.W. Kim and D.M. Dimiduk, J Metals, (8), 1991, 40-47.

[55] M.J. Blackburn, in The Science, Technology and Applications of Titanium, R. Jaffee and N.E. Promisel (eds.), Pergamon Press, 1970, 633-642.

[56] H. Inui, M.H. Oh, A. Nakamura and M. Yamaguchi, Phil Mag A, (66), 1992, 539-556.

[57] S.C. Huang and D.S. Shih, in Microstructure / Property Relationships in Titanium Aluminides and Alloys, Y-W. Kim and R.R. Boyer (eds.), TMS, 1991.

[58] C.R. Feng, D.J. Michel and C.R. Crowe, Scripta Met, (22), 1988, 1481-1486.

[59] Y.S. Yang and S.K. Wu, Scripta Met, (24), 1990, 1801-1806.

[60] D.S. Schwartz and S.M.L. Sastry, Scripta Met, (23), 1989, 1621-1626.

[61] C.R. Feng, D.J. Michel and C.R. Crowe, Phil Mag Let, (61), 1990, 95-100.

[62] Y.S. Yang and S.K. Wu, Phil Mag A, (65), 1992, 15-28.

[63] C.R. Feng, D.J. Michel and C.R. Crowe, Scripta Met, (23), 1989, 1135-1140.

[64] H. Inui, M.H. Oh, A. Nakamura and M. Yamaguchi, Phil Mag A, (66), 1992, 557-573.

[65] H. Inui, M.H. Oh, A. Nakamura and M. Yamaguchi, Acta Met, (40), 1992, 3095-3104.

[66] L.L. He, H.Q. Ye, X.G. Ning, M.Z. Cao and D. Han, Phil Mag A, (67), 1993, 1161-1175.

[67] L. Zhao and K. Tangri, Phil Mag A, (65), 1992, 1065-1081.

[68] L. Zhao and K. Tangri, Acta Met, (39), 1991, 2209-2224.

[69] L. Zhao and K. Tangri, Phil Mag A, (64), 1991, 361-386.

[70] W. Wunderlich, Th. Kremser and G. Frommeyer, Z Metall, (81), 1990, 802-808.

[71] S.R. Singh and J.M. Howe, Phil Mag A, (66), 1992, 739-772.

[72] O. Popoola, C. Cordier, P.Pirouz and A.H. Heusler, Scripta Met, (26), 1992, 1643-1648.

[73] F. Appel, P.A. Beaven and R. Wagner, Acta Met, (41), 1993, 1721-1732.

[74] B.K. Kad and P.M. Hazzeldine, Phil Mag Let, (66), 1992, 133-139.

[75] G.J. Mahon and J.M. Howe, Met Trans A, (21), 1990, 1655-1662.

[76] C.R. Feng, D.J. Michel and C.R. Crowe, Mat Sci & Eng A, (145), 1991, 257-264.

[77] W. Wunderlich, Th. Kremser and O. Frommeyer, Acta Met, (41), 1993, 1791-1799.

[78] P.A. McQuay, D.M. Dimiduk and S.L. Semiatin, Scripta Met, (25), 1991, 1689-1694.

[79] J.D. Bryant, S.L. Kampe, P. Sadler and L. Christodoulou, Met Trans A, (22), 1991, 2009-2019.

[80] S.L. Semiatin and P.A. McQuay, Met Trans A, (23), 1992, 149-161.

[81] Y-W. Kim, Acta Met, (40), 1992, 1121-1134.

[82] Y-W. Kim, ibid [57], 1991.

[83] J.D. Bryant and S.L. Semiatin, Scripta Met, (25), 1991, 449-453.

[84] Y. Zheng, L. Zhao and K. Tangri, Scripta Met, (26), 1992, 219-224.

[85] M.H. Oh, H. Inui, A. Nakamura and M. Yamaguchi, Acta Met, (40), 1992, 167-176.

[86] Y. Umakoshi, T. Nakano and T. Yamane, Scripta Met, (25), 1991, 1525-1528.

[87] G. Ramanth and V.K. Vasedevan, in High-Temperature Ordered Intermetallic Alloys V, I. Baker, R. Darolia, J.D. Whittenberger and M.H. Yoo (eds.), Vol. 288, Materials Research Society, 1993.

[88] P. Wang and V.K. Vasudevan, Scripta Met, (27), 1992, 89-94.

[89] P. Wang, G.B. Viswanthan and V.K. Vasudevan, Met Trans A, (23), 1992, 690-697.

[90] S.C. Huang, E.L. Hall and M.F.X. Gigliotti, in High-Temperature Ordered Intermetallic Alloys II, N.S. Stoloff, C.C. Koch, C.T. Lui and O. Izumi (eds.), Vol. 81, Materials Research Society, 1987, 481-486.

[91] S.C. Huang and E.L. Hall, ibid [2], 373-383.

[92] T. Kawabata, T. Tamura and O. Izumi, ibid [2], 329-334.

[93] S.C. Huang, D.W. McKee, D.S. Shih and J.C. Chesnutt, ibid [31], 363-370.

[94] T. Kawabata, M. Tadano and O. Izumi, Met Trans A, (24), 1993, 141-150.

[95] S.C. Huang and E.L. Hall, Acta Met, (39), 1991, 1053-1060.

[96] T. Hanamura, R. Uemori and M. Tanino, J Mater Res, (4), 1988, 656-664.

[97] D.A. Wheeler, B. London and D.E. Larsen, in Proceedings of the 7th World Titanium Conference, 1992.

[98] S.L. Kampe, P. Sadler, D.E. Larsen and L. Christodoulou, ibid [57], 313-322.

[99] W.O. Soboyejo, D.S. Schwartz and S.M.L. Sastry, Met Trans A, (23), 1992, 2039-2059.

[100] S. Mitao, T. Isawa and S. Tsuyama, Scripta Met, (26), 1992, 1405-1410.

[101] M. Nobuki and T. Tsujimoto, ibid [31], 451-455.

[102] M. Nazmy, M. Staubli and D. Anton, Scripta Met, (26), 1992, 105-108.

[103] K.S. Chan, J Metals, (5), 1992, 30-38.

[104] J. Seeger, A. Bartels and H. Mecking, Scripta Met, (25), 1991, 2523-2528.

[105] Y. Umakoshi and T. Nakano, Acta Met, (41), 1993, 1155-1161.

[106] S.M.L. Sastry and H.A. Lipsitt, Met Trans A, (8), 1977, 299-308.

[107] S.C. Huang, E.L. Hall and M.F.X. Gigliotti, in Sixth World Conference on Titanium, P. Locombe, R. Tricot and G. Beranger, Societé Francaise de Métallurgie, 1988.

[108] V.K. Vasudevan, M.A. Stucke, S.A. Court and H.L. Fraser, Phil Mag Let, (59), 1989, 299-307.

[109] K.S. Chan and Y-W. Kim, Met Trans A, (24), 1993, 113-125.

[110] T. Kawabata, M. Tadano and O. Izumi, Scripta Met, (22), 1988, 1725-1730.

[111] K.S. Chan and Y-W. Kim, ibid {57}, 1991.

[112] R. von Mises, Z Angew Math Mech, (8), 1928, 161-185.

[113] G.J. Taylor, J Inst Met, (62), 1938, 307.

[114] J.F.W. Bishop and R. Hill, Phil Mag, (42), 1951, 414-427.

[115] J.D. Livingston and B. Chamlers, Acta Met, (5), 1957, 322-327.

[116] S. Muira, K. Hamashima and K.T. Aust, Acta Met, (28), 1980, 1591-1602.

[117] C. Rey and A. Zaoui, Acta Met, (30), 1982, 523-535.

[118] H. Kawazoe, T. Takasugi and O. Izumi, Acta Met, (37), 1989, 2883-2894.

[119] Z. Shen, R.H. Wagoner and W.A.T. Clark, Acta Met, (36), 1988, 3231-4242.

[120] M.H. Loretto and R.E. Smallman, Defect Analysis in Electron Microscopy, Chapman and Hall, 1975.

[121] H.K.D.H. Bhadeshia, Geometry of Crystals, The Institute of Metals, 1987, 31-33.

[122] W. Bollmann, Crystal Lattices, Interfaces and Matrices, W. Bollmann, 1982, 44-51.

[123] D.S. Shong and Y-W. Kim, Scripta Met, (23), 1989, 257-261.

[124] J.J. Valencia, C. McCullough, C.G. Levi and R. Mehrabrian, Scripta Met, (21), 1987, 1341-1346.

[125] P. Hirsch, A. Howie, R. Nicholson, D.W. Pashley and M.J. Whelan, Electron Microscopy of Thin Crystals, Robert E. Krieger, 1977.

[126] L.M. Clarebrough, Aust J Phys, (24), 1971, 79-96.

[127] J.W. Edington, Practical Electron Microscopy in Materials Science, (3), Macmillan Press, 1975.

[128] J. M. Silcock and W.J. Tunstall, Phil Mag, (10), 1964, 361-385.

[129] S. Mahajan and D.F. Williams, Int Met Rev, (18), 1973, 43-61.

[130] C. N. Reid, Deformation Geometry for Materials Scientists, Pergamon Press, 1973.

[131] J.R. Rice and R. Thomson, Phil Mag A, (29), 1974, 73-96.

[132] A. Kelly and G.W. Groves, Crystallography and Crystal Defects, Longman, 1970, 178-195.

[133] M.H. Yoo and C.L. Fu, Mater Sci & Eng A, (153), 1992, 470-478.

[134] C.T. Liu and Y-W. Kim, Scripta Met, (27), 599-603, 1992.

[135] M.H. Oh, H. Inui, M. Misaki and M. Yamaguchi, Acta Met, (41), 1993, 1939-1950.

[136] B.A. Greenberg and Y.N. Gornostirev, Scripta Met, (22), 1988, 853-857.

[137] E. Schmid and W. Boas, Kristallplastizität, Julius Springer, 1935.

[138] B.A. Bilby and A.G. Crocker, Proc Roy Soc A, (288), 1965, 240-255.

[139] G. E. Dieter, Mechanical Metallurgy, McGraw-Hill, 1986, 133.

[140] S. Takeuchi and E. Kuramoto, Acta Met, (21), 1973, 415-425.

[141] C. Lall, S. Chin and D.P. Pope, Met Trans A, (10) 1979, 1323-1332.

[142] V. Paidar, D.P. Pope and V. Vitek, Acta Met, (32), 1984, 435-448.

[143] P.M. Hazzeldine and Y.Q. Sun, ibid [34], 209-222.

[144] Z.X. Li, J.Y. Kim and S.H. Whang, Scripta Met, (25), 1991, 2595-2600.

[145] Y.G. Zhang, M.C. Chaturvedi and C.Q. Chen, Phil Mag A, (67), 1993, 979-989.

[146] M.A. Morris and D.G. Morris, Acta Met, (38), 1990, 551-559.

[147] D.G. Morris and M.A. Morris, Acta Met, (39), 1991, 1771-1779.

[148] J.S. Koehler, Phys Rev B, (2), 1970, 547-551.

[149] S.L. Lehoczky, J Appl Phys, (49), 1978, 5479-5485.

[150] C. Suryanarayana and F.H. Froes, Met Trans A, (23), 1992, 1071-1081.

[151] U. Glatzel, K.R. Forbes and W.D. Nix, Phil Mag A, (67), 307-323.

[152] A.N. Stroh, Proc Roy Soc Lond A, (223), 1954, 404-414.

[153] A.N. Stroh, Phil Mag, (46), 1955, 968-972.

[154] A.N. Stroh, Proc Roy Soc Lond A, (232), 1955, 548-560.

[155] M.F. Ashby, in Strengthening Methods in Crystals, A. Kelly and R.B. Nicholson (eds.), Applied Science, 1971, 137-192.

[156] P.P. Rao and K. Tangri, Met Sci Tech, (8), 1992, 1117-1123.

[157] L.C. Lim, Scripta Met, (18), 1984, 1139-1142.

[158] S. Wardle, I. Phan and G. Hug, Phil Mag A, (67), 1993, 497-514.

[159] H.G. Bowden and P.M. Kelly, Acta Met, (15), 1967, 105-111.

8. Acknowledgements

Naturally, it is appropriate to give thanks to the following people which have played an important role throughout the course of this work:

to Professor Maria Morris for the ideas which laid the foundation for this work, her guidance and patience, the freedom to pursue these research topics, transferring her keen sense of critical evaluation to myself by demanding always the best and for sharing her microscopy skills with me.

to Professor David Morris for providing the meticulous research facilities that allowed this work to be carried out, for securing the financial support of this project, for all the indirect support he provided to this work "behind the scenes" and for sharing his passion for metallurgy with me.

to the Swiss government for their financial support of this research through the CERS program.

to Alusuisse-Lonza for providing the experimental materials.

and to the members of the jury Professor M. Loretto, Professor J.L. Martin, Professor M. Morris and Professor D. Morris for accepting to examine this work, for the time and effort they invested in going through the manuscript and all the helpful comments that were made.

to Massoud, Philippe, Claude, Reto, Glenn, Kevin, Bernard and Willie for all the interesting discussions and to all the members of IMS and UMS for their cheerful and kind support.

Finally, I give a special thanks to my wife, Regula, who provided me with the incentive to stay in Switzerland to do this work and who faithfully supported me through the many long hours that were required to successfully conclude this thesis.

9. Appendix

9.1 Controlled Tilting and Orientation Relationships

The Kikuchi map is commonly used in order to perform controlled tilting experiments in the transmission electron microscope. A section of the map for TiAl, with the $L1_0$ crystal structure, is given in Figure 9.1. Indicated on this map are both the relative positions of the zone axes and a schematic representation of the diffraction pattern which would be encountered for the particular beam direction. It should be noted that the unique identification of the diffraction pattern is aided by the presence of the superlattice reflections. Diffraction conditions for the $L1_0$ structure are satisfied for :

h, k unmixed 9.1)

For the usual conditions of diffraction for the fcc structure - i.e. h, k and l unmixed - fundamental reflections are observed. Superlattice reflections are observed for any planes which satisfy equation 9.1, but do not satisfy the conditions for fcc like 001, 110, etc. Accordingly, superlattice diffraction spots are observed in the <110] and <112] zone axes, but not in the <101] or <211] zones. Furthermore, the position of the superlattice spots in the <001> zones gives additional information about the identification of the zone. These conditions are clearly indicated in the schematic representations of the diffraction patterns included in the Kikuchi map in Figure 9.1. The full circles indicate fundamental reflections and are the same as those for the fcc crystal (ignoring the slight tetragonal distortion), while the open diamonds indicate the position of the superlattice spots.

To use this map, two zone axes are located in the crystal and the Kikuchi map is rotated such that the direction of rotation on the map is the same as the rotation that was executed in the microscope to "move" between the two zones. The orientation of the Kikuchi map must then remain fixed and is used to define the sense of rotation necessary to reach any other zones. Controlled tilting along the appropriate "road" is then used to rotate the crystal to the desired orientations. It should be mentioned that this map was constructed without the necessary consideration of the definition of the beam direction (as the upward normal of the foil) [120]. However, selection of the beam direction in the downward sense of the foil normal does not change any of the calculations performed in this work.

It must be noted that this method of tilting is valid only for a single grain. Consistent indexing of related grains can be accomplished by the method given in Table 2.1 and shown more explicitly in Figure 9.2. The construction of the <111> standard projection shown in Fig 9.2(a) is such that the pole of rotation between the adjacent crystals is taken at the center of the projection. In this way, all directions which are perpendicular to this pole, or alternately contained within the plane of the

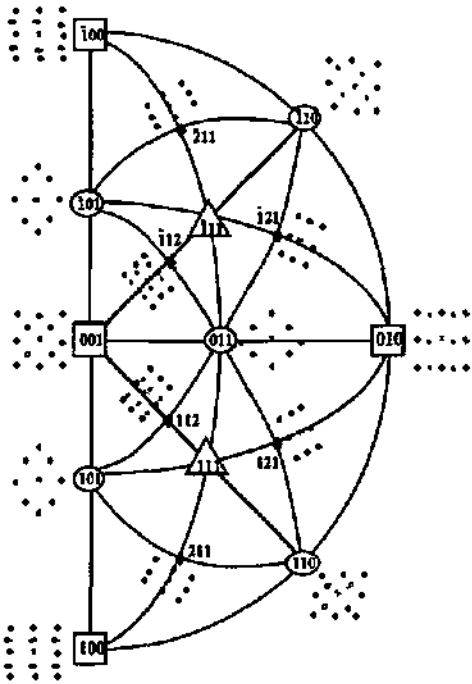

Figure 9.1 : The Kikuchi map for the $L1_0$ structure of TiAl.

rotation, are located on the great circle defined by the rotation plane. Since the orientation relationships between adjacent γ grains can always be described by a multiple of 60° about a <111> direction, this projection provides a convenient way of determining the orientation relationship. Also indicated on this projection is the relative orientation of the [101] and [011] zone axes. This orientation is defined by the relative position of the [001] pole such that the (020) and (200) "roads" are correctly oriented. Also indicated by these representations of the orientation is the common $[\bar{1}\bar{1}1]$ reflection which is used to rotate the crystal with the beam direction always parallel to the plane of rotation.

As an example of how this projection is then used to determine the orientation relationship, it is assumed that an orientation relationship of a 60° rotation about $[\bar{1}\bar{1}1]$, i.e. the pseudo-twin relationship, is present between the two grains under investigation. The relative orientation of the two crystals can then be visualized by manually rotating the projection of one relative to the standard projection which remains stationary. Overlapping projections after the rotation of 60° is shown in

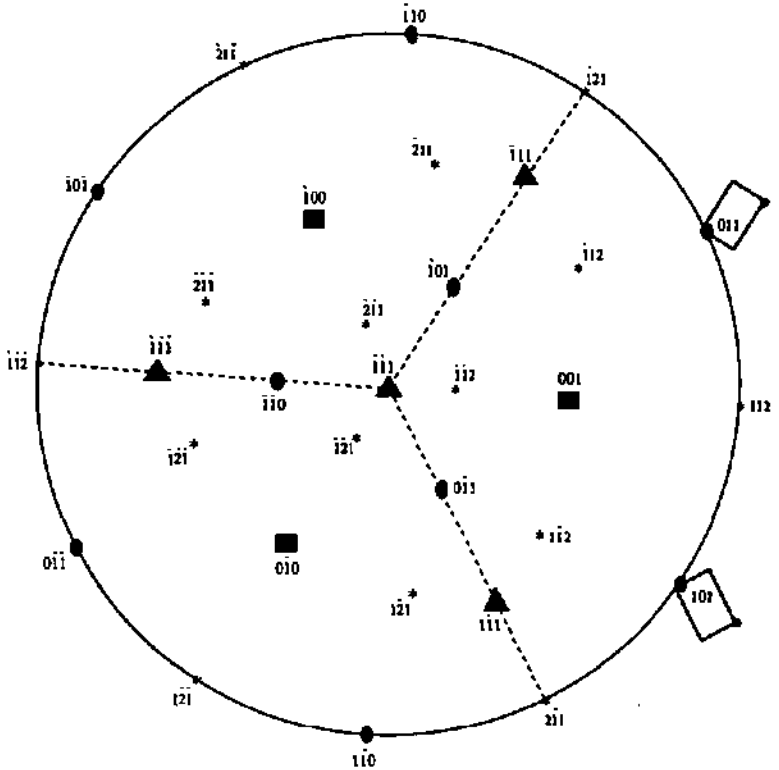

Figure 9.2(a) : A <111> projection constructed with the pole of rotation, $[\bar{1}\bar{1}1]$, at the center.

Fig 9.2(b). In this projection, the initial or 0° grain is represented by the open symbols while the rotated crystal is represented by the filled symbols and the poles are identified with a bold print. Now it is readily seen that for a beam direction parallel to [101] in the initial grain, the beam must be parallel to the [011] zone in the adjacent grain. Similarly, if the beam is parallel to [011] in the initial grain, the beam will be simultaneously parallel to the $[\bar{1}10]$ direction in the adjacent grain. However, the type of zone axes which are parallel in the adjacent grains is not sufficient to define the exact orientation relationship and the position of the zones must also be compared. Comparing Figs 9.2(a)&(b), it is clear that the orientation of the diffraction patterns for these two zone axes appears to be reflected across an axis which would contain the spot from the transmitted beam and the $[\bar{1}\bar{1}1]$ spot. This reflection is characteristic of a twin relationship and, in the case of the 60°

rotation, this is associated with a pseudo-twin relationship. The origin of the inversion lies in the changing of the stacking sequence from ABCABC to CBACBA across the boundary as discussed in Section 1.4.1.

In order to identify the relationship between any two grains, the observed diffraction patterns are compared with the predicted patterns as shown in Table 2.1. A minimum of two simultaneous zone axes (preferably three) must be identified in each grain. Comparison of the presence or absence of superlattice spots and the orientation of the diffraction patterns with the predicted patterns for various rotations will then give the specific orientation relationship between the two grains. It is also desirable to locate a fourth zone axes which is not parallel to the plane of rotation to confirm the full analysis.

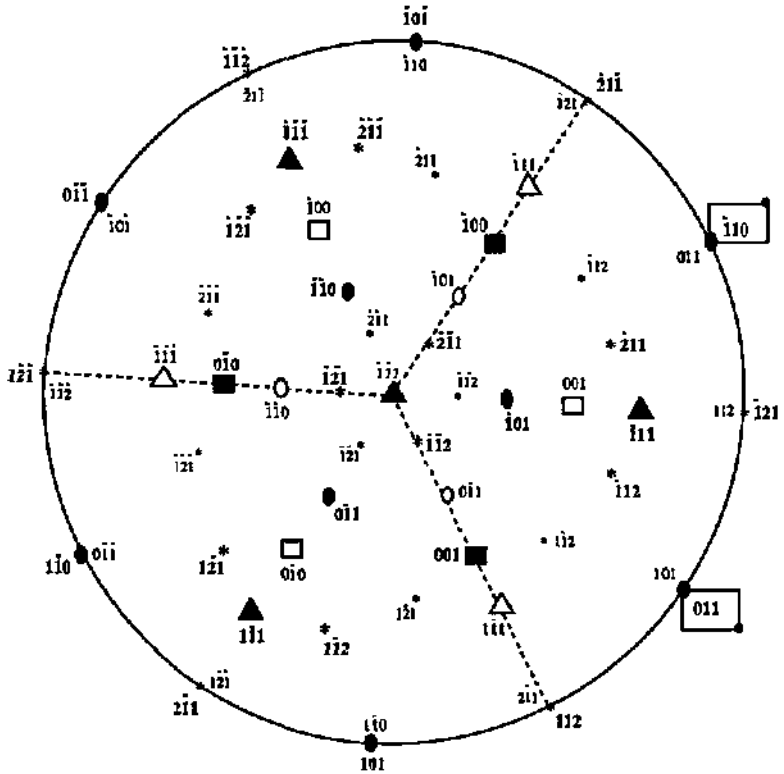

Figure 9.2(b) : Overlapping projections of both a [$\bar{1}\bar{1}1$] standard projection and the projection of a crystal rotated 60° about the [$\bar{1}\bar{1}1$] pole.

It should be noted that this method allows a clear distinction to be made between the two types of pseudo-twin relationships (i.e. 60° or 300°) and the two 120° type rotational faults (i.e. - 120° or 240°). Furthermore, it can be said that many other methods can be used to define the orientation relationship between *two* adjacent grains and that this can generally be accomplished with manipulations of the standard [001] projection. However, the method outlined here is believed to be much simpler than these trial and error methods. Moreover, it provides rapid and consistent indexing when three or more grains are investigated. For instance, the orientations of many lamellae within a lamellar colony are rapidly identified and will be fully consistent. It should be emphasized that the distinction between the 60° and 300° rotation is arbitrary since the rotations will be crystallographically equivalent. The distinction between these rotations is nevertheless made to enable fully consistent determination of the slip systems and for the calculation of the appropriate geometric compatibility factors as described in Section 1.5.2.